Magnetic Properties of Individual Molecules Studied by Scanning Tunneling Microscopy

Dissertation zur Erlangung des akademischen Grades
des Doktors der Naturwissenschaften (Dr. rer. nat.)

vorgelegt von

Steffen Kahle

an der

Universität
Konstanz

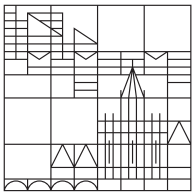

Mathematisch-Naturwissenschaftliche Sektion

Fachbereich Physik

Tag der mündlichen Prüfung: 06. November 2013
1. Referent: Prof. Dr. Klaus Kern
2. Referentin: Prof. Dr. Elke Scheer

Zusammenfassung

Seit 50 Jahren führt die fortschreitende Miniaturisierung der Computertechnik zu exponentiell ansteigender Rechenleistung, und seit ebenso langer Zeit wird ein nahes Ende dieser Entwicklung aufgrund vermeintlich unüberwindbarer technischer Hürden prognostiziert. Die Entwicklung molekularer Elektronik, bei der elektronische Bauteile durch einzelne Moleküle realisiert werden, ermöglicht die weitere Miniaturisierung über die Entwicklungsgrenzen der aktuellen Halbleitertechnologie hinaus. Ein detailliertes Verständnis der elektrischen und magnetischen Eigenschaften einzelner Moleküle ist hierfür notwendig.

Die vorliegende Arbeit ist eine experimentelle Untersuchung der Spineigenschaften von Molekülen sowie deren Beeinflussung durch Aufbringung auf verschiedene Oberflächen. Mithilfe von Rastertunnelmikroskopie (englisch: scanning tunneling microscopy, STM) und Rastertunnelspektroskopie (scanning tunneling spectroscopy, STS) wurden dabei Eigenschaften an einzelnen Molekülen untersucht, die bisher nur durch Ensemblemessungen bekannt waren.

Im ersten Teil der Arbeit wurden Spinanregungen von molekularen Magneten untersucht, um zu bestimmen, ob und wie sich ihr magnetisches Moment bei der Deposition auf verschiedene Oberflächen verändert und ob sich die Vorhersagen aus Bulkmessungen auf einzelne Moleküle übertragen lassen.

Als typischer Vertreter wurde zunächst Mn_{12}-Acetat auf Metallsubstrate sowie auf dünne Isolatorschichten aufgebracht. Als Substrat wurde dabei Gold (Au(111)) sowie eine Monolage Bornitrid auf Rhodium (BN/Rh(111)) verwendet. Das empfindliche Molekül wurde mittels Elektrospray-Ionisation auf die Proben aufgebracht, und STM-Messungen bestätigten die Deposition von intakten und nicht agglomerierten Molekülen. Mithilfe von STS konnten Spinanregungen in einzelnen Mn_{12}-Molekülen auf BN/Rh angeregt und vermessen werden. Eine Analyse der beobachteten Spinanregungen ergab, dass die durch Bulkmessungen bekannten Spineigenschaften von Mn_{12} bei der Deposition auf BN/Rh erhalten bleiben; eine wichtige Voraussetzung zur Nutzbarmachung von Mn_{12} in möglichen Anwendungen. Bei Mn_{12}-Molekülen auf Au konnten keine Spinanregungen festgestellt werden, was vermutlich auf die Reduktion der Mn-Atome durch die Metalloberfläche zurückzuführen ist.

Diese Ergebnisse stellen die erste erfolgreiche Untersuchung der Spineigenschaften von einzelnen Mn_{12}-Molekülen mittels STM dar und zeigen die Eignung von BN/Rh als Substrat für einzelne molekulare Magnete.

Vergleichbare Experimente wurden ebenfalls mit Cr_7Ni, einem anderen molekularen Magneten, durchgeführt. Nach der Deposition auf Au(111) konnten einzelne Cr_7Ni-Moleküle mittels STM identifiziert werden. STS-Messungen zeigten wie im Fall von Mn_{12} keine Spinanregungen, was auf eine Veränderung der Spineigenschaften durch den Kontakt mit dem Metall schließen lässt. Auf BN/Rh(111) konnten Cr_7Ni-Moleküle nicht stabil abgebildet werden, da sie während der Messungen von der STM-Spitze über die Probe geschoben wurden. STM-Messungen auf Isolatoren wie BN erfordern besonders geringe Abstände zwischen Spitze und Probe.

Im zweiten Teil der Arbeit wurde ein rein organisches Molekül untersucht, das über ein ungepaartes Elektron und damit einen freien Spin innerhalb einer Nitronyl-Nitroxid-Gruppe (NIT) verfügt. Das ungepaarte Elektron ist über Teile der NIT-Gruppe delokalisiert und dadurch reaktionsträge, so dass es bei der Deposition auf Metallen erhalten bleibt. Durch das ausschließliche Auftreten von s- und p-Orbitalen in organischen Molekülen wird eine Entartung mit höheren Orbitalen verhindert, was die theoretische Modellierung erleichtert.

Die Moleküle wurden auf Au(111) deponiert und mithilfe von STM abgebildet. Mittels STS konnte ein Kondoeffekt beobachtet werden, der sich durch die Kopplung des freien Spins des Moleküls mit den Leitungselektronen des Substrats gebildet hatte. Eine genaue Untersuchung der Kondoresonanz für Temperaturen im Bereich von $1.5 - 16$ K und bei Magnetfeldern von bis zu 14 T ergab, dass sich der Kondoeffekt im untersuchten Temperaturbereich im Grenzfall schwacher Kopplung befindet (weak coupling regime).

Da sich bisher untersuchte Kondosysteme von einzelnen freien Spins stets im Bereich starker Kopplung befanden (strong coupling regime), ermöglichen die hier gezeigten Ergebnisse zum ersten Mal den Vergleich mit den ursprünglichen, störungstheoretischen Beschreibungen des Kondoeffekts, die ebenfalls den Bereich schwacher Kopplung beschreiben. Als ein nicht entartetes Spin-$^1/_2$-System stellt das untersuchte Molekül das einfachste Modellsystem zur Beschreibung des Kondoeffekts dar. Die experimentellen Ergebnisse dieser Arbeit sind daher ein idealer Vergleichsmaßstab für bekannte wie auch zukünftige theoretische Modelle.

Contents

1. Introduction

„There is plenty of room at the bottom“, with these words did later Nobel laureate Richard Feynman open his speech in 1959 about the technological prospects if one would be able to manipulate matter at the atomic scale [1]. He proposed that when device sizes reach the realm of quantum mechanics, unprecedented functionalities will be achieved. In 2013 nanotechnology has reached maturity and its first products exploiting quantum mechanical effects have left the labs and entered everyday consumer products [2, 3]

A driving force behind this trend is the rapid miniaturization of integrated circuits in computer chips, which since more than 50 years has lead to exponentially increasing computing performance and a vast reduction in power consumption. Throughout this time the end of such rapid advancement has been proposed many times due to allegedly insurmountable obstacles. With commercially available feature sizes of 22 nm and fabrication plants using 14 nm-technology in construction, a new obstacle is rapidly approaching [4–6]: At feature size approaching 5 - 7 nm it will be difficult to operate transistors utilizing the traditional CMOS design since quantum tunneling through the transistor channel will occur. This constitutes a fundamental physical limit and might mark the end of the silicon-era in information technology. And it might be reached within the next ten years [7].

Going beyond this limit requires the use of new concepts and materials, which today are still in the realm of fundamental physics. One possibility are molecular electronics, where electronic devices are realized by a single functional molecule. Besides allowing a further miniaturization of devices, molecular electronics can be employed with novel concepts like spintronics [8] or quantum computation [9], with the latter being able to ultimately increase computer performance by going beyond the boolean “on/off” paradigm. Furthermore, the use of molecules as building blocks allows the use of bottom-up techniques as a more economical way of creating structures than the traditional top-down approach. The advancement of molecular electronics is the technological motivation for the work on single molecules presented in this thesis

Maybe even greater than the impact on technology are the possibilities for fundamental research when being able to observe and control matter at the atomic scale. Nanoscience opens the access to study quantum mechanical systems at their natural

scale and to isolate single effects which otherwise disappear in the statistical behaviour of macroscopic objects. The ability to build structures with atomic precision beyond what can be found in nature can lead to new and unexpected effects.

The vision of Feynman came to reality with the invention of the scanning tunneling microscope (STM) by Binnig and Rohrer in 1982 [10], which allowed the imaging of single atoms and the ability to move them around as demonstrated by Eigler in 1990 [11]. The STMs utility for diverse scientific areas stems from its spectroscopic versatility allowing the mapping of vibrational, electrical or magnetic properties with atomic resolution.

The work presented in this thesis investigates the magnetic properties of individual molecules and their interaction with an underlying substrate using a low-temperature STM. Unlike single atoms, molecules are often the fundamental units which provide a desired functionality and can be tailor-made for their specific purpose. Scanning tunneling microscopy allows the investigation of individual molecules in contrast to other techniques which average over ensembles of molecules (typically thin layers, single crystals or powders). The deposition on a substrate is a requirement for STM measurements as well as a prerequisite for any practical application.

In the first part of this thesis molecular magnets are studied, which are a class of molecules which show ferromagnetic effects like hysteresis, but whose magnetism is of purely molecular origin, so that no interaction between molecules is required. Molecular magnets are candidates for high-density data storage and have been proposed for the use as entangled quantum systems in quantum computing applications.

Molecular magnets typically contain several atomic spins forming a combined spin state. This combination of spins is complex enough to show interesting effects like quantum tunneling of magnetization. However, the number of coupled spins is small enough to form discrete quantum states rather than band structures. This makes molecular magnets ideally suited for the observation and manipulation of coupled spin systems. The number and arrangement of the atomic spins within a molecule can be tuned by chemical synthesis. This adaptability and the possibility of building absolutely identical units are substantial advantages of molecular magnets compared to non-molecular magnetic nanoparticles.

Practically all information on molecular magnets have been obtained by experimental techniques which average over ensembles of molecules. Measurements on single molecular magnets have been hindered by the difficulty of retaining their magnetic moment upon deposition on surfaces. We deposit the molecular magnets Mn_{12} and Cr_7Ni directly on metal substrates and on insulating layers on top of metals, the latter to decouple the magnetic atoms inside the molecules from the metal substrate to avoid quenching of the

spin due to charge transfer. We then investigate the spectrum of spin states by means of spin-flip spectroscopy to identify, if and how the magnetic properties of the molecules have changed upon deposition.

In the second part of this thesis we focus on the Kondo effect, which arises from the interaction of a single impurity spin with the electrons of an otherwise non-magnetic metal substrate. The Kondo effect of magnetic defects in metals is known since the 1930s [12] and has been explained in the 1960s [13], but the emerging possibilities of nanoscience have revived this interest in the last 15 years. Measurements on single Kondo impurities have been performed by STM [14] and in single electron transistor setups [15] with control of the local environment or the possibility to tune the parameters of the impurity. Most of this recent work has been focused on the Kondo effect of a single metal atom.

In the work presented in this thesis we study the Kondo physics of rather new system: The free spin of an organic molecule coupled to the electrons of a metal substrate. This represents a "simple" spin-$^1/_2$ system with low orbital quantum numbers and therefore allows a detailed quantitative characterization of the Kondo physics, which was impeded in past studies by higher spin quantum numbers, orbital degeneracies or too high Kondo temperatures. The use of Kondo impurities embedded in molecules allows a wider variety of these parameters which can lead to different types of the Kondo effect. A detailed spectroscopic study including the temperature and field dependance of the molecular Kondo system is performed.

This thesis is organized as follows:

Following this introduction chapter 2 describes the used experimental techniques, namely scanning tunneling microscopy and scanning tunneling spectroscopy. Chapter 3 explains the home-built STM setup used for the experiments focusing on how the experimental requirements for such delicate measurements are achieved. Chapter 4 discusses the investigations regarding molecular magnets. It starts with an overview of molecular magnetism and then describes the findings obtained by spectroscopy for Mn_{12} deposited on the different substrates followed by results from analogous experiments performed with Cr_7Ni. In Chapter 5 different models for the Kondo effect are described in detail and then compared to the results of the spectroscopic study of the molecular Kondo system. A summary of all results as well as suggestions for further experiments can be found in chapter 6.

2. Experimental Techniques

2.1. Scanning Tunneling Microscopy

Since the invention by Binnig and Rohrer in 1982 [10, 16, 17] the STM has developed to be a versatile tool, allowing unprecedented access to the atomic scale, with a resolution often only limited by experimental difficulties rather than physical principles. The conceptual and instrumental simplicity make the STM an affordable tool and its small size allows easy implementation into more complicated setups.

While the STM is primary known for its imaging and atom manipulation capabilities [11], the versatility of the STM to study a variety of problems is owed to its spectroscopic capabilities down to the atomic scale. This makes the STM an invaluable tool for fundamental research.

2.1.1. Concept

A sharp metallic wire, the tip, is brought within a distance of a few Angstrom to a conducting sample surface. A bias voltage is applied resulting in a current flowing between tip and sample. While classically no electron would be able to pass the insulating gap between these two electrodes, such a current is based on the quantum mechanical *tunnel effect* (details in the next section) and is highly sensitive to changes of the gap distance.

The tip is mounted on a piezo actuator being able to move the tip in all three axes with pm precision. To image a sample surface, the tip is approached towards the sample until the desired tunneling current is achieved (usually 10 pA - 1 nA), then the tip is scanned over the surface line by line.

- In the *constant height mode* the piezo-axis perpendicular to the sample surface (the z-axis) is kept at a constant value. Thus, the actual distance between tip and sample varies while the tip scans over the protrusions and indentations of the surface. The current varies respectively and is recorded as image signal.
- In the *constant current mode* the tunnel current is kept constant by regulating the z-piezo to maintain a constant distance between tip and sample. Thus, the

z-height of the piezo follows the contour of the sample surface and can be used as image signal. In this mode crashes into a high surface area or the loss of contact in a depression can be avoided, making it the first choice for most measurements.

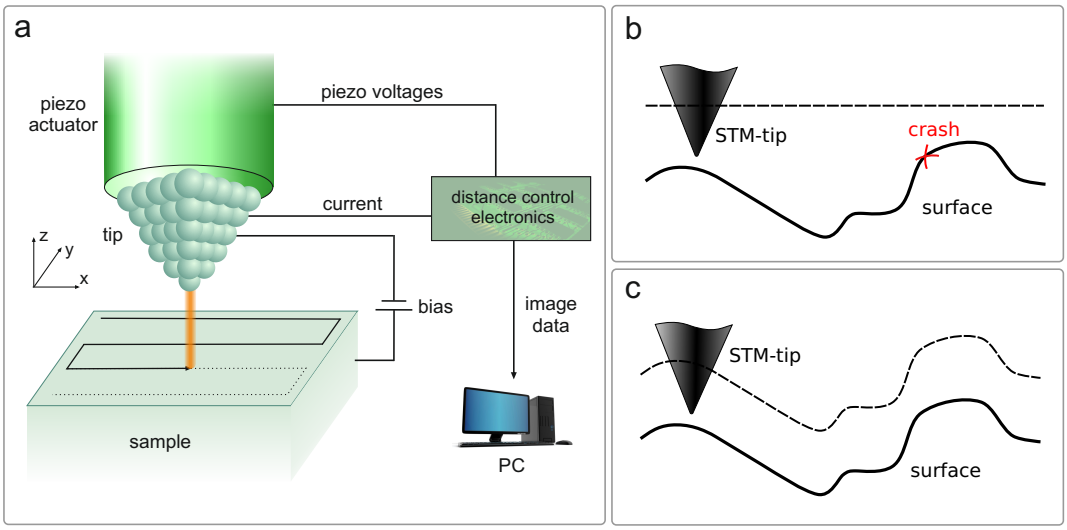

Figure 2.1.: (a) Schematic view of an STM showing its principal components. (b, c) The different scanning modes: constant height mode (b), and constant current mode (c).

The image signal does not necessarily represent the topography of the sample surface. The tunnel current can increase either due to a reduced gap distance or due to an increase of the local conductivity of the sample. Thus, actual elevations can appear as depressions [18], and measured heights must be treated as *apparent heights*, especially when the sample consists of several materials with different conductance.

As an imaging technique the STM is not limited by diffraction and offers outstanding resolution down to the atomic scale. The primary resolution exists in the z-axis, based on the sensitivity of the underlying tunnel effect towards the gap distance. Height differences of a few pm can be measured routinely. The lateral resolution also benefits from the strong decay of the tunnel current in z. An increased gap distance by a few pm lowers the tunnel current substantially, so that only the atom on the very apex of the tip conducts almost all of the current (see figure 2.1). Therefore the tip being a wire of macroscopic diameter (μm) can produce images with a lateral resolution of 1 Å.

2.1.2. The Tunnel Effect

The quantum mechanical nature of the electrons allow them to penetrate (to *tunnel*) through classically impenetrable barriers such as a vacuum gap. The tunnel effect is based on the overlap of wave functions from both sides of the barrier and thus is only significant over very short distances up to a few Angstroms.

The wave function of an electron state reaching into the barrier region is described by

$$\Psi(z) = \Psi(0)e^{-\kappa z} \tag{2.1}$$

decaying along the z-axis (into the barrier) with the decay constant κ depending on the barrier height. Assuming the barrier represents the vacuum gap between an STM's tip and the sample and for bias voltages small against the work function Φ_T of the tip and Φ_S of the sample, κ can be described by $\kappa = \sqrt{m(\Phi_T + \Phi_S)}/\hbar$.[1] The probability for an electron to tunnel from the tip to the sample (or vice versa) through a gap of width D is proportional to $|\Psi(D)|^2 = |\Psi(0)|^2 e^{-2\kappa D}$.

The energy scheme of a tip-sample-junction is shown in figure 2.2. Without a bias voltage the Fermi energies of tip and sample are aligned at the same energy level and no net tunneling occurs. Applying a voltage V to the sample shifts its Fermi level accordingly, and all sample states Ψ_i in the energy interval eV contribute to the tunnel current:

$$I_T \propto \sum_{E_i = E_F - eV}^{E_F} |\Psi_i(0)|^2 e^{-2\kappa D} \tag{2.2}$$

The strong distance dependance from the decaying wave functions is the reason for the extraordinary topographic sensitivity of the STM. The high value of κ ensures that as a rule of thumb the tunneling current changes by one order of magnitude for each Angstrom difference in the gap distance D.

2.1.3. Current Calculation

For a more detailed understanding of the tunneling current in a real STM junction, it is necessary to go beyond the one-dimensional model of equation 2.2. In a general form the tunnel current can be calculated by summing over all possible states Ψ_m and Ψ_n of tip and sample, multiplied with the absolute square of tunneling matrix elements M_{mn},

[1] Typical values for Φ are $4 - 6$ eV for the used metals. This results in $\kappa = 10^{10}$ m^{-1}.

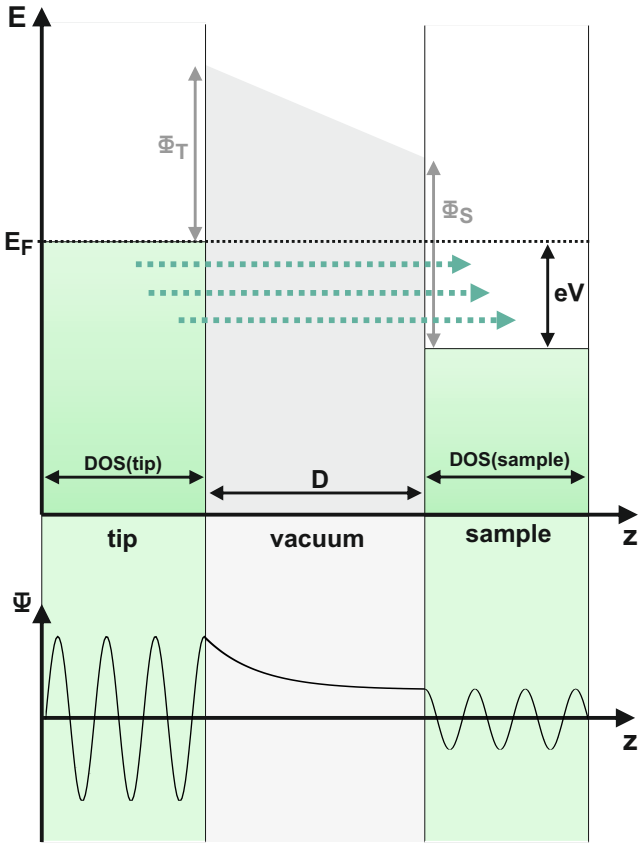

Figure 2.2.: Energy diagram of a tunnel contact (upper part) and corresponding progression of the wavefunction Ψ decaying into the gap (lower part). Φ_T and Φ_S are the work functions of tip and sample respectively, which form the trapezoidal barrier of width D. The applied voltage eV allows net tunneling through the gap (green arrows). For simplicity, zero temperature is assumed, resulting in sharp Fermi edges.

which describes the transition probability from state Ψ_m to Ψ_n. To account for the continuous nature of the states in metals, we will use the concept of *density of states* (DOS) to describe their energy spectrum. A bias voltage V is applied to the sample resulting in a current flowing from tip to sample as

$$I_{t\to s} = \frac{4\pi e}{\hbar} \int \rho_s(\epsilon - eV)\rho_t(\epsilon)\ f(\epsilon - eV)[1 - f(\epsilon)]\ |M_{mn}|^2\ \mathrm{d}\epsilon. \tag{2.3}$$

Here $f(\epsilon) = [1+\exp(\epsilon/k_BT)]^{-1}$ is the temperature dependent Fermi distribution function, ϵ the energy with respect to the common Fermi level, and $\rho_t(\epsilon)$ and $\rho_s(\epsilon)$ are the DOS of the tip and sample, respectively. Since electron tunneling can only occur from

occupied states in the tip into unoccupied states of the sample, the combination of both Fermi functions limit the integral to a corresponding range. Thus, for low temperatures and small bias values only the states close to the Fermi energy contribute to the tunneling current.

In the general case the effective current from tip to sample has to be calculated according to $I = I_{t\to s} - I_{s\to t}$, where the current of opposite direction has to be subtracted from the one described above. This results in a current of

$$I = \frac{4\pi e}{\hbar} \int \rho_s(\epsilon - eV)\rho_t(\epsilon)\ [f(\epsilon - eV) - f(\epsilon)]\ |M_{mn}|^2\ \mathrm{d}\epsilon. \tag{2.4}$$

If the applied bias is large with respect to the temperature induced broadening of the Fermi edge, the Fermi functions can be replaced by step functions and both equations are equivalent.

As can be seen from equation 2.4 the essential problem in calculating the current is determinating the tunneling matrix M. Bardeen has addressed this problem already in 1961 for the tunneling between two electrodes separated by a thin oxide layer [19]. Instead of solving the Schrödinger equation for the complete system, he considered each electrode as an independent subsystem with a wavefunction that decays exponentially into the tunnel gap. For a small overlap between these wavefunctions the matrix elements M_{mn} for the transition between Ψ_m and Ψ_n can be calculated as

$$M_{mn} = \int_F (\Psi_m^* \nabla \Psi_n - \Psi_n \nabla \Psi_m^*) \cdot \mathrm{d}\vec{A} \tag{2.5}$$

with the integration area F separating both electrodes.

In Bardeen's equation the electronic states of both electrodes contribute equally. While STM measurements are aiming to resolve the electronic states and the topography of the sample, they face the problem that the exact atomic configuration of the tip is also unknown. Therefore a more simplified model is necessary, which neglects the tip configuration, but still gives acceptable results to calculate the tunnel current.

Tersoff and Hamann [20,21] applied Bardeen's approach to a tunnel junction, making explicit assumptions about the shape of the wavefunctions of tip and sample. They assumed a spherical wave function for the tip and a plane wave approximation for the sample, both decaying outwards exponentially. Using the general tunneling equation in

the limit of low temperature (eq. 2.3) and small bias voltage V, they obtain for the tunneling current

$$I = \frac{8\pi^3 e^2 \hbar^3}{m^2} \, V \rho_t(E_F) \; R^2 e^{2\kappa R} \underbrace{\sum_n |\Psi_n(\vec{r_0})|^2 \delta(E_n - E_F)}_{\text{LDOS} = \rho_s(\vec{r_0}, E_F)} \tag{2.6}$$

with R as the curvature of the tip, and κ as in the one dimensional model as $\kappa = \sqrt{2m\Phi}/\hbar$ with the work function Φ, identical for tip and sample. The sum represents the local density of states (LDOS) of the sample at the Fermi energy and at the location $\vec{r_0}$, which is at the center of the tip apex.

Hence, the tunnel current at small bias can be approximated to be proportional to the LDOS of the sample at the Fermi level: $I \propto \rho_s(E_F)$.

2.2. Scanning Tunneling Spectroscopy

2.2.1. Concept

The scanning tunneling microscope is not only capable of just imaging a sample surface, but can also be used as a spectroscopic tool investigating the electronic states of a sample at the atomic scale. *Scanning tunneling spectroscopy* (STS) can measure the LDOS of the sample and additionally inelastic processes excited by the tunneling electrons. This way STS can obtain information about the functionality of a molecule or atom, which is essential for possible applications like molecular electronics. The first use of tunneling spectroscopy in an STM was done by Binnig in 1985 [22]. Since then STS has been able to observe fundamental phenomena like the spin-flip of an atomic spin [23], the lifetime of an excited electron state [24], or the Kondo resonance of a single atom [14].

Since the main results of this thesis have been obtained by scanning tunneling spectroscopy, this technique will be discussed in detail. In particular, $\mathrm{d}I/\mathrm{d}V$-spectroscopy was used, the most common type of STS.

Since we are interested in the density of states of the sample, we need a tip with a constant DOS in the bias range of interest. By further assuming that the transition prob-

ability between two states $|M_{mn}|^2$ can be approximated as a constant $|M|^2$ independent of the states, we can simplify the general tunneling equation 2.4 to

$$I \propto |M|^2 \rho_t \int \rho_s(\epsilon - eV)[f(\epsilon - eV) - f(\epsilon)] \, \mathrm{d}\epsilon. \tag{2.7}$$

If the temperature broadening $k_B T$ is small against the energy resolution of the experiment, the Fermi function can be replaced by a step function and we obtain for the derivative

$$\frac{\mathrm{d}I}{\mathrm{d}V}(V_0) \propto \rho_s(eV_0). \tag{2.8}$$

Hence by measuring the $I(V)$-curve and taking the differential conductance $\mathrm{d}I/\mathrm{d}V$, we obtain the LDOS of the sample as a function of bias.

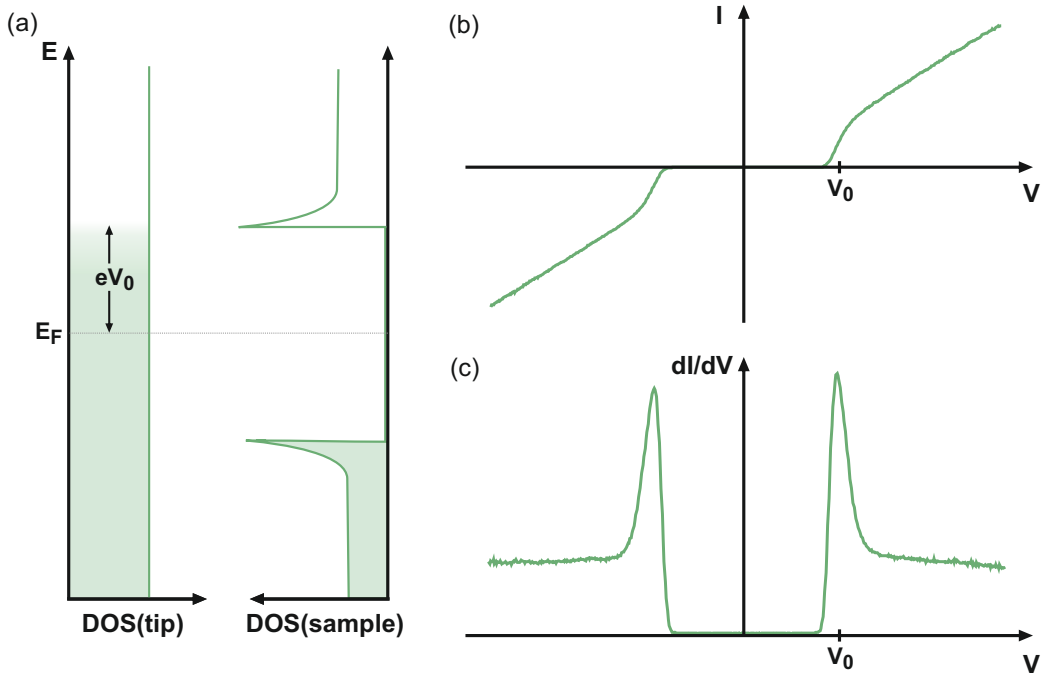

Figure 2.3.: **STS of a superconducting sample.** (a) The DOS of the sample shows a superconducting gap around E_F, while the DOS of the tip is assumed constant. An applied bias of V_0 raises the level of occupied states above E_F. (b) The corresponding $I(V)$-curve: for small positive bias below V_0 the current is zero, since there are no empty states available in the sample. At V_0 the current raises due to available states in the sample. The actual onset of the current is shifted before V_0 due to the finite temperature of the tip. (c) The derivative of the curve in (b) reproduces the DOS of the sample.

In practice this is done by locating the tip over the desired position of the sample, turning off the feedback-loop controlling the z-height, and then sweeping the bias while measuring the current. Since the measured $I(V)$-curves are often too noisy to give useful information after differentiation, the $\mathrm{d}I/\mathrm{d}V$-signal is usually directly measured with the lock-in technique.

2.2.2. Lock-In Technique

To allow spectroscopic studies even at low signal-to-noise-ratios, a lock-in amplifier is used to measure the derivative of the tunnel current ($\mathrm{d}I/\mathrm{d}V$) directly. For that a small sinusoidal voltage V_{LI} is added to the bias voltage

$$V_{total} = V_{bias} + V_{LI}\sin(\omega t). \tag{2.9}$$

The frequency ω is chosen higher than the bandwidth of the feedback loop, so that the z-positioning of the tip is not affected; it is also higher than the sweeping of the bias during spectroscopy, so that for each measurement point of a spectrum the voltage V_{total} can be averaged to be V_{bias}.

As can be seen in figure 2.4a, for each point in an I(V)-curve, the actual voltage applied to the sample is now a voltage range of the width $\Delta V = 2V_{LI}$ centered around V_{bias}. While ΔV is set to a constant value, the corresponding current range $\Delta I(V_{bias})$ depends linearly on slope of the curve. The lock-in amplifier extracts the signal with frequency ω from the tunnel current and returns the amplitude ΔI of this signal as an output value. The lock-in signal is thus proportional to $\mathrm{d}I/\mathrm{d}V$ as function of the bias voltage and likewise proportional to the LDOS of the sample.

The essential benefit of this technique is that by modulating the signal of interest with a certain frequency, the measurement can be shifted to an ideal (noise-free) frequency, and thus circumvent most noise sources:

The measured current consists of the desired $I(V)$-signal overlaid with a noise component, which originates mainly from the instabilities of the tip-sample-distance and usually has a $1/f$-dependence. When measuring the tunnel current directly (without applying a modulation), a low-pass filter can be used to reduce high-frequency noise, but the high noise at low frequencies still disturbs the measurement. Modulating the bias with a high frequency shifts the current from the high-noise environment at 0 Hz to a low-noise environment at higher frequencies. Now the noise at low frequencies can be easily cut off to gain a clearer signal.

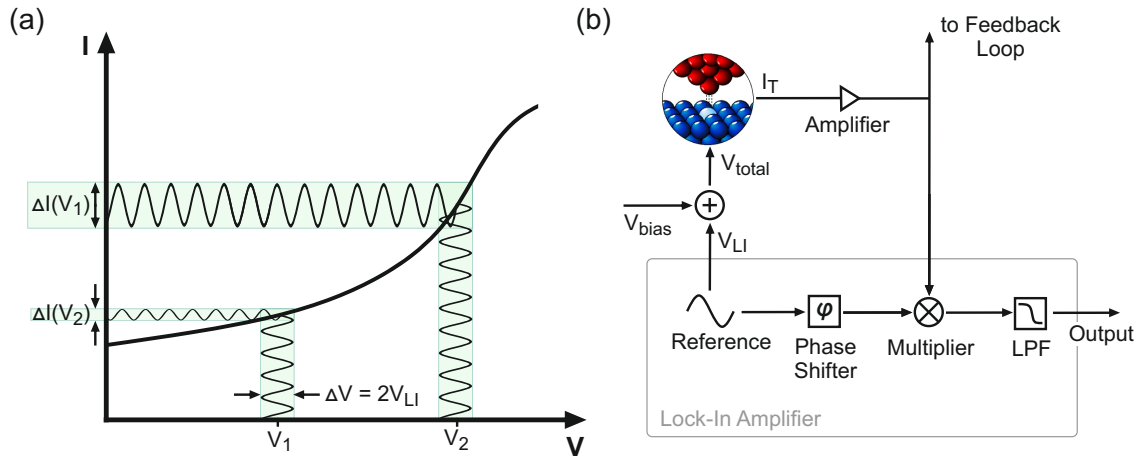

Figure 2.4.: (a) Modulating the bias voltage with an additional voltage ΔV results in a modulated current with an amplitude ΔI, which is proportional to the slope of the $I(V)$-curve. (b) Schematic of the signal path inside and outside the lock-in amplifier. The current amplifier is actually converting the tunnel current into a voltage (I-V-converter).

Figure 2.4b shows a schematic signal path. While higher modulation frequencies are more favorable for lock-in detection, we are limited by the bandwidth of the current amplifier[2] and thus typically use frequencies of $700 - 900$ Hz. The extraction of signals with the correct frequency (the "lock" onto the signal) is realized inside the lock-in amplifier by multiplication of the sinusoidal reference signal with the tunnel current. With the phase of both signals aligned before multiplication, the multiplied signal is only positive and can be averaged by a low pass filter producing the DC lock-in output signal proportional to the LDOS.

In figure 2.5a the I(V)-curve measured over a Kondo resonance can be seen. The noise in the tunnel current is so high, that the Kondo peak in the dI/dV signal obtained by numerical differentiation is only barely visible. Applying a low-pass filter (smoothing) improves the signal quality, but low frequency noise can not be eliminated. The derivative obtained by the lock-in technique bypasses most of the noise and presents a much clearer signal (fig. 2.5b).

The lock-in technique has the disadvantage of limiting the energetic resolution of the spectroscopy due the finite size of the modulating voltage. A detailed description of this limitation is given in section 2.2.4.

[2]We use a Femto DLPCA-200 with a cutoff frequency of 1.1 kHz at a gain of 10^9 V/A.

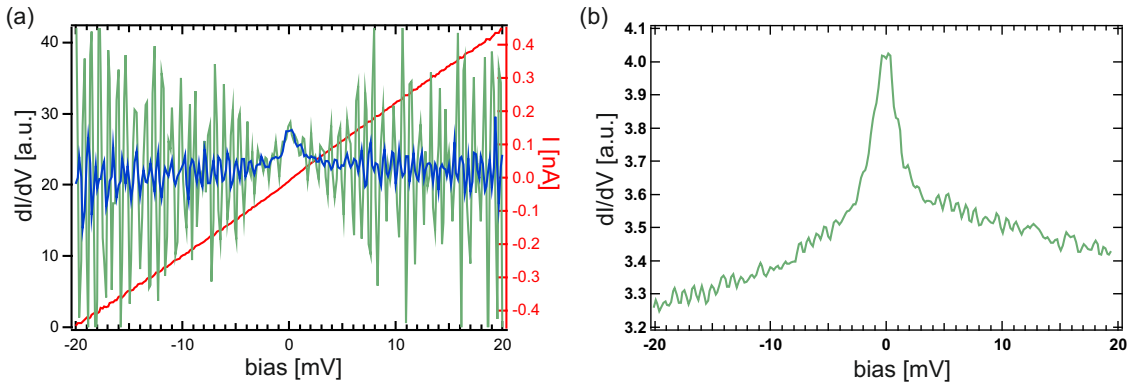

Figure 2.5.: **Comparison of direct measurement vs. lock-in technique.** (a) direct measurement of the current (red) over a Kondo peak, the numerical derivative (green), and the derivative after applying a low pass filter (blue). (b) The same measurement with the $\mathrm{d}I/\mathrm{d}V$-curve obtained via a lock-in amplifier.

2.2.3. Inelastic Electron Tunneling Spectroscopy

The spectroscopy considered so far was limited to elastic tunneling of the electrons with the aim of mapping the unperturbed DOS of the sample. In the case of *inelastic electron tunneling spectroscopy* (IETS) the electrons are not only passively mapping the sample DOS, but are exciting processes in the sample by losing part of their own energy.

IETS was already performed on traditional metal-oxide-metal tunnel junctions in the 1960s. The results could be attributed to vibrations of molecules contained in the barrier [25,26], making IETS a spectroscopic tool complimentary to the optical methods like IR- or Raman-spectroscopy. After the invention of the STM, the group around Wilson Ho pioneered in using IETS to observe vibrations of individual molecules [27]. The combination of STM and IETS allowed the spectroscopic analysis of a molecule with unprecedented knowledge (and even control) over its direct environment.

IETS is hereby not limited to vibrational modes, but can probe all kind of electronic excitations. In particular the excitation of a single electron spin has been observed by Heinrich [23] in 2004, which will be the groundwork for chapter 4 of this thesis.

For inelastic tunneling the sample needs to provide two discrete states with an energy difference E_0 as illustrated in figure 2.6a. Electrons can tunnel elastically through the gap for all bias voltages. If the bias voltage is high enough ($eV \geq E_0$), the electrons can excite the sample state by losing part of their kinetic energy. This additional tunneling channel leads to an increase of current for a bias above $V_0 = E_0/e$ (fig. 2.6b). Once both channels are available, the current increases again linear with the higher slope (conduc-

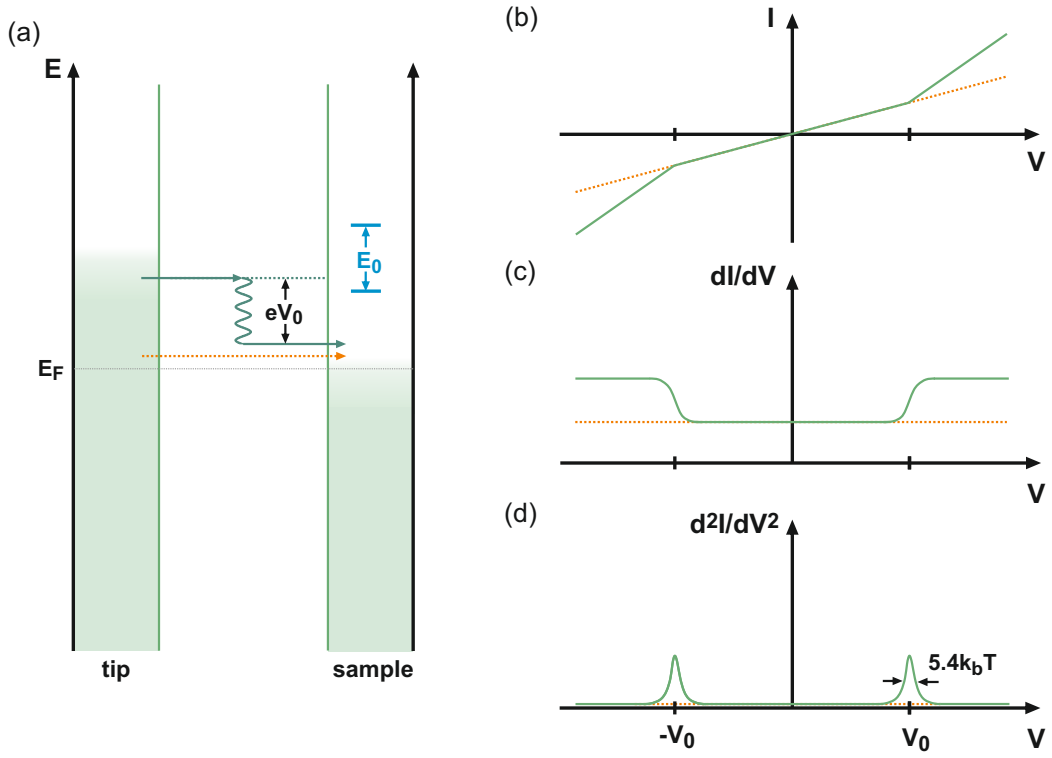

Figure 2.6.: **STS including an inelastic tunneling process.** (a) Energy scheme of tip and sample assuming a constant DOS. Elastic tunneling (orange arrow) occurs at all bias values, inelastic tunneling (green arrow) only if the bias voltage is sufficient to excite the sample state ($eV > E_0$). Note that the position of the sample states (blue) in this plot is arbitrary, since e. g. vibrational states cannot be related to the Fermi level of the conduction band. (b,c,d) I(V)-curves and corresponding 1st and 2nd derivatives for the described system (green) or only the elastic part (orange).

tivity) of the combined channels (assuming a constant DOS). As can be seen in figure 2.6c the inelastic channel above V_0 leads to a step-like structure in the $\mathrm{d}I/\mathrm{d}V$-signal, and consequently to peaks in the second derivative $\mathrm{d}^2I/\mathrm{d}V^2$, with the latter one often used for easier attribution of the position of V_0. The structure is symmetrical around zero bias, since the excitations occur independent of the direction of the tunneling electrons.

At finite temperature the steps in the $\mathrm{d}I/\mathrm{d}V$-curve are not forming sharp edges, but follow the equation[3]

$$\frac{\mathrm{d}I}{\mathrm{d}V} = \frac{e^{2x} - xe^x - e^x}{(e^x - 1)^2} \qquad \text{with} \qquad x = \frac{\pm eV - E_0}{k_B T}. \tag{2.10}$$

[3] an equivalent expression used in the literature is $\frac{xe^x - e^x + 1}{(e^x - 1)^2}$ with $x = -\frac{\pm eV - E_0}{k_B T}$

This curve can be generated from the general tunneling equation (eq. 2.4), which includes the thermal broadening of the Fermi levels on both side. The broadened step edges can be seen in figure 2.6c. According to Lambe [26] the peaks in the second derivative have a width (fwhm) of $5.4k_BT$, the equivalent of convoluting a indefinitely sharp peak twice with the Fermi function.

So far we have assumed that a tunneling electron can excite the sample state independent of the tunnel current. However, this is only valid for the non-saturated case, where the lifetime of the excited state is smaller than the average time between two tunneling events. For higher currents or longer lifetimes the excited state can saturate, resulting in different spectral shapes [28]. This can be experimentally used to measure the lifetime of sample states. [24]

2.2.4. Energy Resolution

The theoretical energy resolution of STS is limited by two factors: The thermal broadening due to the temperature of the experiment and the broadening due to the modulation voltage of the lock-in technique.

The thermal broadening is due to the finite width of the involved Fermi levels. In the case of elastic tunneling, the sample DOS is imaged by shifting it with respect to the Fermi level of the tip. When the Fermi level passes a feature in the DOS, this feature can only be resolved with the sharpness of the Fermi level (of the tip). Since the Fermi level of the sample is at a different energy than the feature of interest, it does not contribute to the broadening. Accordingly the thermal broadening function $\Phi_T(\epsilon)$ is the derivative of one Fermi distribution $f(\epsilon)$:

$$\Phi_T(\epsilon) = f'(\epsilon) = -\frac{1}{k_BT}\frac{\exp(\epsilon/k_BT)}{[1+\exp(\epsilon/k_BT)]^2}. \tag{2.11}$$

The measured $\mathrm{d}I/\mathrm{d}V$-signal can be described as the convolution product of the actual sample DOS and the broadening function.

$$\frac{\mathrm{d}I}{\mathrm{d}V}(\epsilon) = \rho_S(\epsilon) * \Phi_T(\epsilon) \tag{2.12}$$

Thus, an ideally sharp peak in the DOS, described by a delta-function, would be imaged as gaussian-like peak of the width (fwhm) $\Delta_T = 3.5k_BT$ as can be seen in figure 2.7.

In the case of inelastic tunneling we are not just imaging the sample DOS, but are exciting states in the sample. For this excitations the energy difference between the

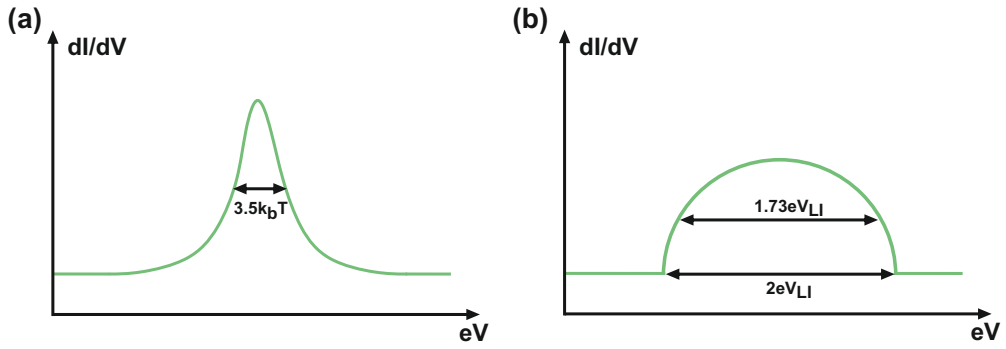

Figure 2.7.: **Thermal broadening and instrumentation function.** (a) The thermal broadening function for elastic processes appears gaussian-like with a width of $3.5k_BT$. For inelastic processes the width is $5.4k_BT$. (b) The lock-in modulation leads to a half-spherical instrumentation function with radius eV_{LI} and a fwhm-value of $1.73eV_{LI}$.

Fermi levels on both sides of the tunnel gap is of relevance and thus the broadening of both Fermi levels contribute to the total broadening. The corresponding broadening function has a width (fwhm) of $5.4k_BT$ [26].

An additional broadening occurs due to the use of the lock-in technique. When the modulation voltage V_{LI} is added to the bias voltage, the $\mathrm{d}I/\mathrm{d}V$-measurement is actually averaging over a bias range of width $2V_{LI}$ centered around V_{bias} (see figure 2.4). The instrumental function can be described as a half sphere by

$$\Phi_{LI}(\epsilon) = \sqrt{(eV_{LI})^2 - \epsilon^2} \tag{2.13}$$

with a width (fwhm) of $\Delta_{LI} = \sqrt{3}eV_{LI} = 1.73eV_{LI}$ [29]. For lock-in amplifiers the output amplitude is usually given as root-mean-square (rms) value $V_{LI}^{(rms)} = V_{LI}/\sqrt{2}$, which gives the relation $\Delta_{LI} = 2.45eV_{LI}^{(rms)}$. As above the measured signal can be described by a convolution of the DOS with the instrumental function $\frac{\mathrm{d}I}{\mathrm{d}V}(\epsilon) = \rho_S(\epsilon) * \Phi_{LI}(\epsilon)$.

Obviously, in a real measurement both broadening effects must be taken into account. Since the convolution is commutative we can describe the measured $\mathrm{d}I/\mathrm{d}V$-signal as convolution of the DOS $\sigma(\epsilon)$ with both broadening functions:

$$\frac{\mathrm{d}I}{\mathrm{d}V}(\epsilon) = \rho_S(\epsilon) * \Phi_T(\epsilon) * \Phi_{LI}(\epsilon) \tag{2.14}$$

While this can be used to model the broadening effects on a known DOS, the deconvolution of measured spectra is often not feasible. To calculate the original width Δ of a

gaussian-like peak in the DOS, we can approximate the experimentally obtained width Δ_{exp} by

$$\Delta_{exp}^2 = \Delta_T^2 + \Delta_{LI}^2 + \Delta^2. \tag{2.15}$$

This approximation assumes a gaussian-like shape for all involved curves, and obviously produces more accurate results for broadening factors (Δ_T, Δ_{LI}) smaller than the actual width (Δ). This equation works equally well for the widths to be fwhm or hwhm as long as both types are not mixed.

While the modulation voltage can be freely chosen, the choice of the temperature is limited by the experimental setup and eventually by the studied object which requires a certain temperature. The trade-off for higher energy resolution given by lower modulation voltages is a lower signal intensity.

For optimal resolution the modulation voltage should be chosen, so that the lock-in broadening is insignificant compared to the inevitable thermal broadening, yet as big as possible for a high signal intensity. Figure 2.8 shows which modulation voltages are preferable for each temperature. In practice higher voltages can be necessary to obtain reasonable signal-to-noise ratios.

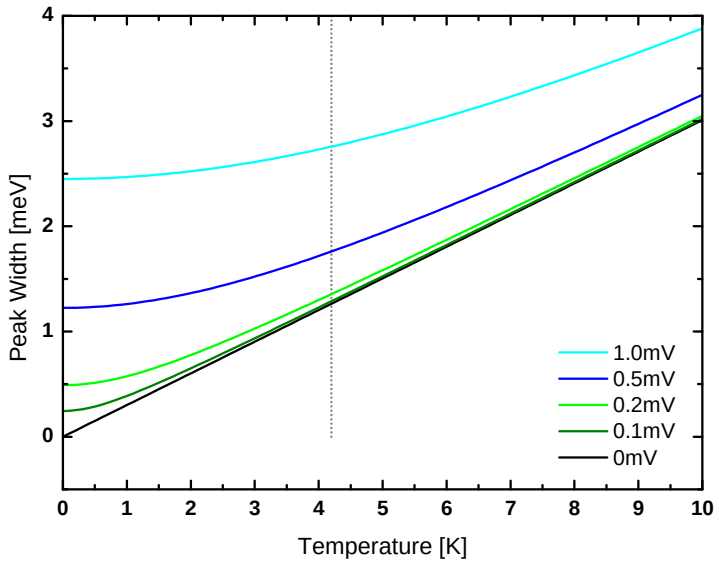

Figure 2.8.: **Peak broadening.** Without modulation voltage the peak broadening increases linear with temperature (black line). With higher modulation voltages (given in $V_{LI}^{(rms)}$) the broadening increases. An ideal modulation voltage at 4.2 K (vertical line) should be 0.2 mV or less, so that the LI-broadening is negligible. All curves assume elastic tunneling processes and show fwhm-values.

In principle lower signal intensity can be compensated by longer averaging times (or averaging multiple spectra), but the maximal duration of spectroscopic measurements is limited by experimental reasons: Thermal drift and piezo drift slowly change the positioning of the tip, particulary during spectroscopy, when the feedback loop is turned off. Additionally the atomic configuration of the tip and the studied sample (e. g. a molecule) have to stay intact, which can get critical when trying to compensate the low signal intensity with higher currents. In this thesis averaging times up to 30 min have been shown feasible.

3. Experimental Setup

All experiments were performed with a home-built STM situated at the Max Planck Institute for Solid State Research in Stuttgart. To allow experiments on individual molecules the machine requires ultra high vacuum (UHV), very low temperatures and a high degree of mechanical stability to operate. The machine was built 2001-2005 and a more detailed description can be found in the theses of Paolo Messina and Gero Wittich [30, 31]. Maintenance, repair and performing upgrades on this machine were an important part of this thesis.

3.1. Chamber Setup

The STM is operating in a UHV chamber, which can be divided in three sections, separable by gate valves: the "preparation chamber", the "STM chamber", and the "STM tube", in which the actual STM head is placed.

Vacuum in the first two sections is achieved by a combination of turbo molecular pumps, ion getter pumps, and a titanium sublimation pump to a base pressure of 10^{-10} mbar. It can be temporarily decreased to 10^{-11} mbar by using additional cryo-pumps. The STM tube has no active pumping system. For initial evacuation (e. g. after a repair) it is pumped through the STM chamber; after UHV is reached the cryostat surrounding the STM tube is cooled down to 4K, forming a very effective cryopump around the STM tube. With all gases but hydrogen condensed at this temperature, the pressure inside the tube is much lower than in the other chambers, but cannot be measured with a gauge due to limited space inside the cryostat. A rough estimation based on the observed accumulation of hydrogen on the sample surface over time yields a pressure of below 10^{-13} mbar inside the tube.[1]

The preparation chamber is used for in-situ cleaning of metal substrates and the deposition of molecules or thin films on top of it. For this purpose it is equipped with a sputter gun for Ar^+ bombardment and a filament heating to anneal the samples up to 1100 K. Furthermore it is equipped with molecular evaporators and leak valves for the controlled influx of gases as well as an Auger spectrometer for analysis of the surface composition. The sample can also be cooled by liquid nitrogen or helium to immobilize deposited atoms or molecules on the surface.

[1] Observed build-up of 0.1 ML per month and assumed growth of one ML per second at $3 \cdot 10^{-6}$ mbar.

The STM chamber provides storage for up to five samples in UHV conditions and houses the manipulator for the sample transfer inside the actual STM. An attached load-lock chamber allows for easy transfer of samples in and out of the chamber without breaking the vacuum. Also an additional transfer chamber can be attached to the load-lock, which enables sample transfers to other machines under continuous UHV conditions. This transfer chamber is described in more detail in the PhD thesis of Christian Michaelis [32].

The STM tube contains the actual STM head and is surrounded by a superconducting 14 Tesla magnet, whose field is perpendicular to the sample surface inside the STM. While the tube is made of non-magnetic stainless steel, the welding seams show weak ferromagnetism due to material restructuring by the welding process. The STM tube is the only cryogenic part of the UHV system and thus can maintain its vacuum level without any additional pumps.

3.2. Low Temperatures

To achieve low temperatures for the STM as well as for the superconducting magnet both are embedded in a cryostat with a 100 liter liquid helium reservoir and a standing time of up to five days. While the magnet is completely surrounded by the liquid helium and thus constantly at a temperature of 4.2 K, the actual STM is thermally decoupled from the helium bath to allow for variable temperatures. As illustrated in figure 3.1 the UHV tube containing the STM is surrounded by a helium gas volume of variable pressure and an additional evacuated double walled dewar for further decoupling from the liquid helium tank.

To minimize thermal influx into the cryostat copper plates are installed in the gas volume serving as radiation shields. Two additional movable radiation shields can be placed in the STM tube after a sample is transferred down to the STM. With both inner radiation shields in place an actual sample temperature of 4.2 Kelvin can be achieved, while just one radiation shield is sufficient to reach 4.3 Kelvin.

For cooling the STM below 4.2 K we use a Joule-Thomson cooling cycle operating in continuous mode. Therefore a thin tube is installed feeding helium gas from outside the cryostat to the the bottom of the helium gas volume close to the STM. A long copper tube is used running in loops in the outer helium area to ensure good heat exchange. The incoming gas liquifies on the way to the bottom of the cryostat, where it enters the gas volume through a capillary and provides cooling power to the STM by both

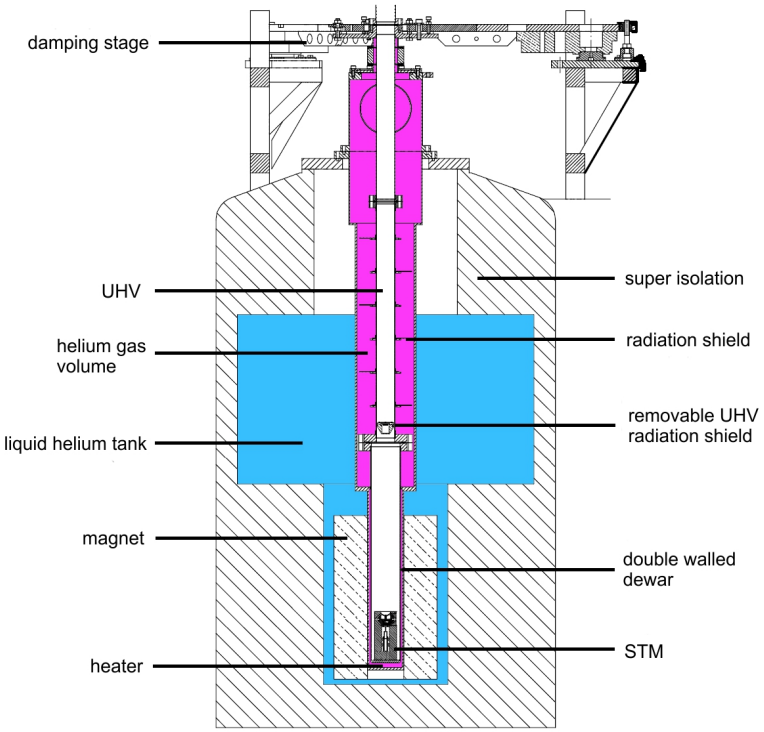

Figure 3.1.: **Cross-section of the cryostat**. Showing the different parts of the cooling system. The blue part is filled with liquid helium, the pink one with helium gas (adapted from [31]).

vaporization and expansion. The inflow through the tube is countered by pumping at the top of the gas volume to allow for continuous operation. The corresponding pump has to be mechanically separated from the STM to not prohibit the measurements due to its vibrations (more in section 3.3).

With this setup and both radiation shields in place temperatures down to 1.3 K have been achieved, but require very long waiting times. In everyday use typical sample temperatures are rather $1.4 - 1.5$ K.

Until 2008 the same machine was equipped with a slightly modified cooling system being able to run with ^{3}He as a cooling agent, which reached temperatures down to 0.8 K [32]. Due to the raging ^{3}He prizes and complications in the operation of the cryostat this was not continued.

For variable temperature measurements the STM can also be heated by a foil resistance heater installed underneath the STM tube in the gas volume. The sample temperature is measured by a resistance sensor with a distance of 2.5 cm from the sample; an additional sensor is mounted next to the foil heater for a better dynamic control

of the heating process. With this setup temperatures up to 20 K have been realized with a stability of ±0.01 K over several hours. Higher temperatures are accessible with less stable conditions.

3.3. Vibration Isolation

The exceptional sensitivity of the tunnel current on the distance between tip and sample is the main ingredient to the STM's success story in exploring the atomic scale. But this sensitivity equals also a noise source since all mechanical vibrations in the lab environment will lead to fluctuations in the tip-sample-distance (z-noise) which will be exponentially increased in the tunnel current (I_t-noise).

The first measure to minimize the z-noise is to actually build the STM head as stiff as possible, so that external vibrations do not translate into changes of the tip-sample distance. Certain features like an in-situ changeable sample, a coarse approach mechanism, and the size limitations inside the magnet bore are setting the limits here.

Vibration isolation is the second major method to limit z-noise. While most STMs are located in basements or even in separate buildings, the machine used for this thesis is located on the sixth floor and thus exposed to all building vibrations generated by the institute's life or due to winds. Therefore the vibration isolation system is very sophisticated, consisting of three stages (see figure 3.2).

The first and most outer damping stage consists of a metal frame mounted on four active dampers (TMC Stacis 2100) employing piezo actuators to detect and counter ground movements. Compared to usually employed air isolators this system allows for damping down to relatively low frequencies of 0.6 Hz, but also unavoidably generates some noise due to the acting piezo stacks.

The second stage dampers are positioned on top on the first frame, and are holding the vacuum chambers, the cryostat, and all additional equipment. They are air dampers (Newport I-2000) reducing vibrations down to 1.6 Hz.

The inner stage (or 3rd stage) containing the STM head consists of the STM tube hanging inside the cryostat with 1 mm space around it to be isolated from the movements of the cryostat. This very small gap requires precise adjustment of the STM tube inside the cryostat, but a larger gap would also require a larger magnet bore and result in a lower available field. The tube is mounted below a three legged star resting on air dampers (Newport CM-225). Best damping results were obtained when overriding the

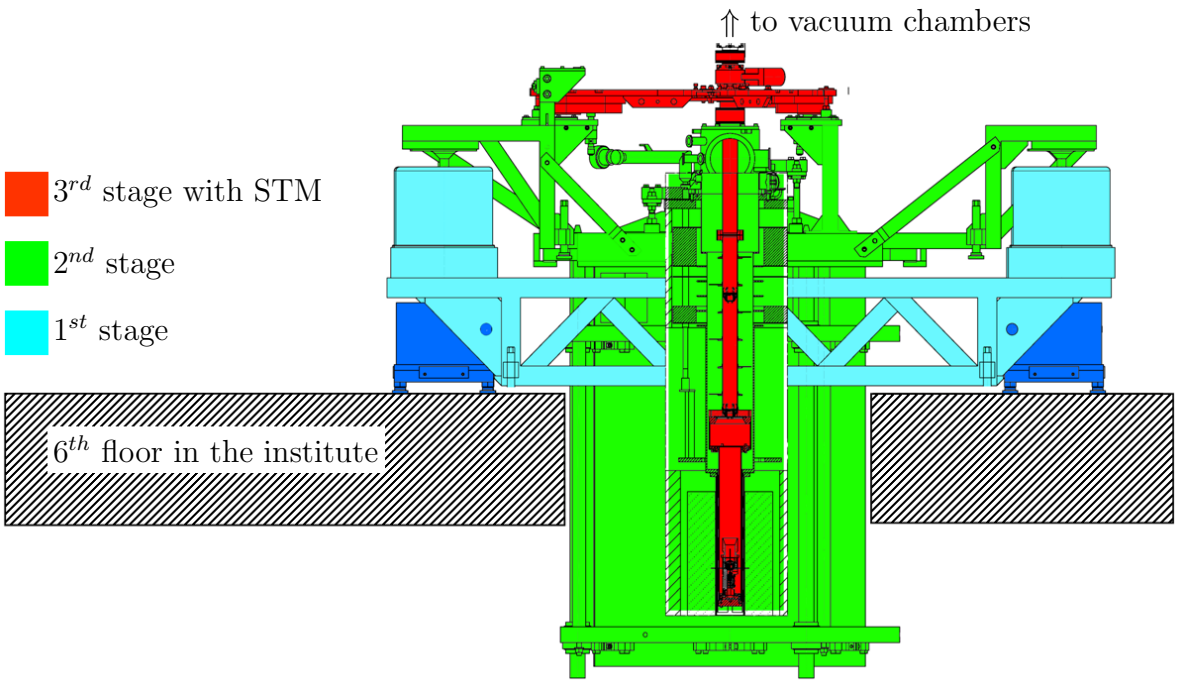

Figure 3.2.: **The damping stages of the system.** Blue: piezo actuators. Cyan: 1^{st} stage frame, holding the air dampers. Green: 2^{nd} stage supporting the vacuum chambers and the cryostat. Red: 3^{rd} stage, the STM tube containing the STM head. (from [32])

self-leveling control of the three air dampers and instead supplying each damper with individually set gas pressures until the position of the tube is centered in the magnet bore.

A non-centered tube is more likely to strike against the inner wall of the magnet bore even on minute outside vibrations, an event resulting in severe vibrations on the system, which are often sufficient to cause a tip crash. Running the STM showed, that otherwise stable tunneling conditions are often impaired by these strikes. Thus, when designing a similar system, one should value stable operation over maximum magnetic field capacity and increase the gap size between tube and cryostat.

Besides shielding the STM from environmental vibrations, there are also mechanical noise sources intrinsic to the system, which are more difficult to avoid. The liquid helium in the cryostat is slowly boiling off and produces periodic sound waves in the gas volume above it resulting in vibrations in the range of $130 - 140$ Hz. These vibrations were reduced by equipping the helium backflow line with a flow reducer and using a rubber backflow line.

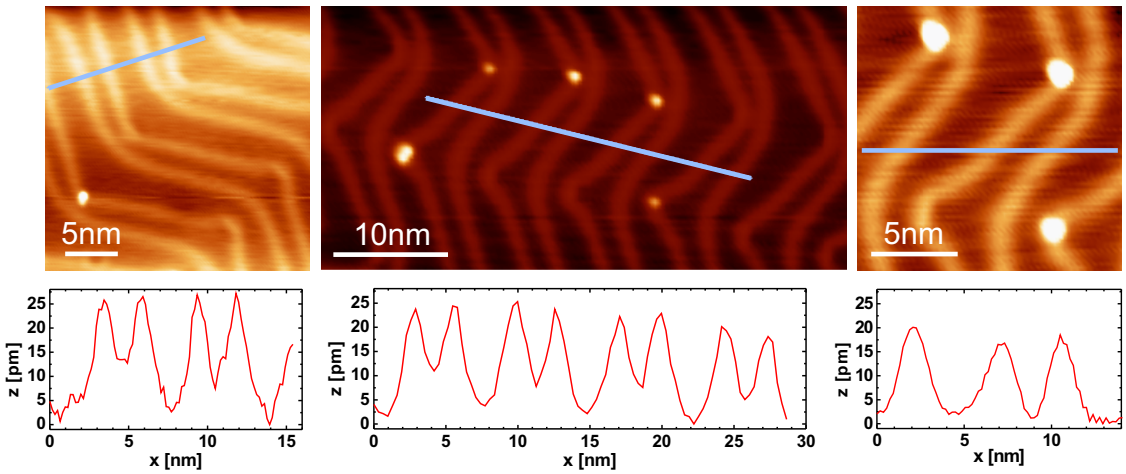

Figure 3.3.: **Noise performance.** STM images and corresponding height profiles obtained on Au(111) showing the herringbone reconstruction of the surface. The height profiles are taken along the blue lines and show z-noise of less than 2 pm (peak-to-peak). The data has been obtained with the combined STM/AFM-head. Image parameters: no magnetic field, $U = 0.5$ V, $I_T = 20 - 30$ pA, $10 - 20$ ms/px

Furthermore, the field of the superconducting magnet creates a stray field, which couples to the reinforced concrete of the lab floor and thus reduces the efficiency of the two outer coupling stages. Also the inner tube, which contains slightly magnetic parts, is attracted by the magnet, so that at fields above 5 T the tube is jammed inside the magnet instead of being suspended from above, shortening the 3rd damping stage.

The overall signal quality for STM imaging and spectroscopy is determined by the mechanical stability of the system. This stability does not only vary with obvious parameters (magnetic field or a quiet lab environment), but often also changes throughout the day. Figure 3.3 shows STM images and corresponding linescans with a noise level in z of less than 2 pm. Hereby regular imaging speeds of $10 - 20$ ms per pixel have been used. Slower imaging speeds (or a less responsive feedback-loop) can be used to further reduce the apparent z-noise. It should be noted, that these images represent perfect conditions, and that a z-noise up to 10 pm is regularly observed.

In 2013 the experiment will be moved into a new building especially designed for high precision measurements. The building is equipped with a vibration isolation system, from which a further reduction of the noise level is expected.

3.4. STM Head

During the time of this thesis a major update in the experimental setup was carried out: while at the beginning of the thesis the core of the machine was a regular scanning tunneling microscope (STM), in 2011 a new head was installed in the system with a combined scanning tunneling microscope and atomic force microscope (STM/AFM) based on the qPlus design [33].

For compact dimensions fitting inside the magnet bore both heads are based on the Pan design [34], implementing the coarse approach of the tip towards the sample as a 'slip-stick' mechanism. For safe sample transfers the tip can be retracted around 15 mm from the sample surface, which is of particular importance since the sample holders vary in height by up to 1-2 mm and the sample transfer has to be done "blind" due to a lack of optical access inside the cryostat. It has to be noted, that the tip cannot be changed in-situ and thus the PtIr-tips installed in the system are used for years.

In both setups the tip is mounted on the same type of piezo tube with a scan range of around 1000 nm in the sample plane and a z-range of around 100 nm (both at 4 Kelvin). Additionally, the sample can be moved one-dimensionally by tilting it very slightly so that there is negligible sample tilt, but still a new scan area can be reached.

In the combined STM/AFM the tip is mounted on one prong of a quartz tuning fork, similar to the ones used as resonators in commercial watches. The tuning fork is acting as a very stiff resonator, whose vibration is directly translated into an electrical signal due to the piezoelectric properties of quartz. When the tip, glued to the end of the vibrating prong, gets close to the sample surface, it is experiencing a force gradient, which changes the oscillation frequency of the tuning fork. This is detected as the AFM signal and can provide force mapping on the atomic scale.

The tip is connected with a separate wire to enable simultaneous STM operation. Even though typical amplitudes of the tuning fork of $50 - 200$ pm change the tip-sample distance so much, that the tunnel current changes significantly during each oscillation period, the resonance frequency of $18 - 25$ kHz is high enough to ensure a constant current signal at the output of the tunnel current I-V-converter due to its limited bandwidth of only 1.5 kHz. Thus, simultaneous measurements of both the AFM and the STM channel are possible. The feedback channel control the z-height during a scan can be freely chosen from both sub-systems.

Further updates of the new head were to enhance the tilting mechanism of the sample holder, to not only allow to reach new scan areas, but also to be able to rotate the sample

a full 180° for the deposition of atoms onto the sample while it is at 4 K. A Hall-sensor was installed to measure the magnetic field close to the sample and not only rely on the calibration data of the magnet. Measurements at different fields showed a deviation of less than 1% from the calibrated data.

Detailed information about the combined STM/AFM head can be found in the diploma thesis of Tobias Herden [35].

4. Spin Excitations Observed on Individual Molecular Magnets

4.1. Introduction to Molecular Magnetism

Ferromagnetism has long been thought to be an exclusive property of selected metals and a substantial amount of material seemed necessary for this collective phenomena. For too small amounts (below the superparamagnetic limit) thermal fluctuations prevent the formation of stable magnetic moments and otherwise ferromagnetic materials like Co or Fe behave paramagnetic.

Ferromagnets are organized in magnetic domains in which all magnetic moments are aligned parallel to minimize their energy. The magnetic moment of such a domain is protected against demagnetization by a restoring force (Heisenberg interaction) acting on any individual spin which got unaligned by thermal fluctuations. This self-stabilization mechanism allows a domain – once aligned by a magnetic field – to keep its magnetic orientation even in the absence of a field. Since the Heisenberg interaction requires several neighbouring spins, it does not work for too small ensembles of magnetic atoms.

Only since the 1990s a new class of magnetic materials known as *molecular magnets* has been discovered. While early works have demonstrated the synthesis of spin carrying molecules [36], the break-through for molecular magnets has been achieved with Mn_{12}, a molecule with a high-spin ground state [37] that showed a slow magnetic relaxation giving rise to a magnetic hysteresis [38]. While these are typical signs of ferromagnetic behaviour, the magnetism of single molecular magnets (SMMs) can not be explained by the ferromagnetic picture of magnetic domains since they lack a sufficient number of magnetic atoms.

Another effect stabilizing the orientation of magnetic moments does not require neighbouring spins and can even be observed on single magnetic atoms in a non-magnetic environment: *Magnetic anisotropy* defines the directional dependance of the magnetic moments in a material. In the simplest case of uniaxial anisotropy an *easy axis* defines the axis of preferred magnetization. The two opposing directions along this axis are degenerate and the actual direction of magnetization can assume either of both.

In the case of a single spin S this can be described by an anisotropy energy $E = DS_z^2$ with $D < 0$ and the direction z defined as easy axis. Thus, the spin favors a maximized z-component m, e. g. for a total spin $S = 10$ it will assume $m = \pm 10$ or a superposition of both. If the sample is prepared in a defined state like $m = -10$, the energy DS^2 is needed to "climb up the ladder" of states to reach $m = +10$ (fig 4.1a). This energy is called the *anisotropy barrier* and it defines the relaxation time τ of the system through thermally activated processes as $\tau = \tau_0 \exp\left(\frac{DS^2}{k_B T}\right)$. For systems of multiple spins the total anisotropy energy scales with the number of magnetic atoms. Anisotropy can be caused by the structure of a spin lattice, the coupling of several spins inside a molecule or even the interaction with a non-magnetic substrate in the case of an individual atom.

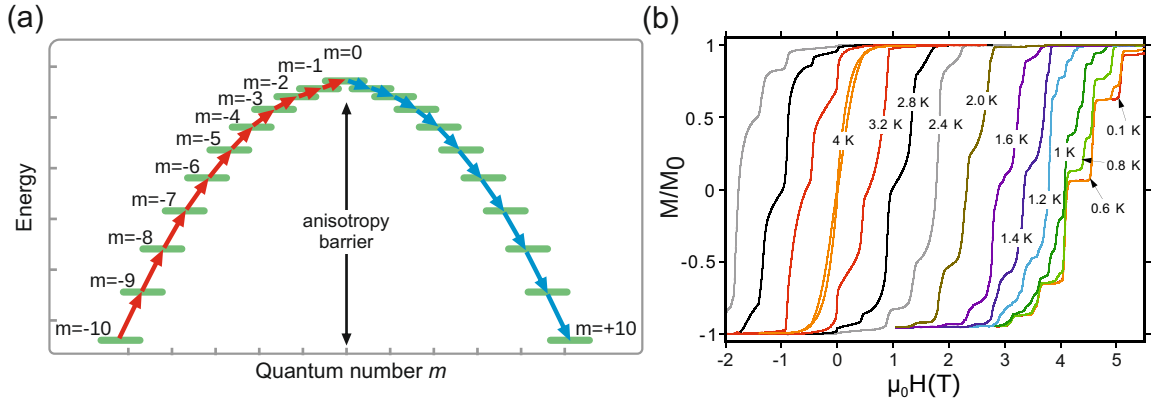

Figure 4.1.: (a) Schematic representation of the energy states of a spin system with $S = 10$ and easy axis anisotropy $-DS_z^2$. For the transition from $m = -10$ to $m = +10$ the spin needs to "climb of the ladder of states" to $m = 0$ (red arrows) and can then relax into $m = +10$ (blue arrows). (b) Hysteresis loops for single crystals of Mn_{12}-tBuAc at different temperatures. At lower temperatures the loops display steps and plateaus due quantum tunneling of magnetization, an effect in which the system tunnels through the anisotropy barrier even at energies below DS_z^2. Image from [39].

Molecular magnets describe a class of spin-carrying molecules, which show ferromagnetic effects like hysteresis (fig. 4.1b) or the corresponding slow relaxation of the magnetization. Unlike regular ferromagnets this behaviour is of purely molecular origin, so that no interaction between multiple molecules is required. It can be explained by the anisotropy of the molecular spin. This molecular spin is often composed of several atomic spins inside the molecule. With this definition a SMM is the smallest possible ferromagnetic unit, which is – unlike nanoclusters of ferromagnetic material – reproducible in its exact size and structure and can in principle be tailor-made in its magnetic and chemical properties.

Molecular magnets typically have a core-shell structure, with the core consisting of interlinked metal atoms carrying the spin and an organic shell protecting the core against chemical reactions or charge transfer. To achieve high spin quantum numbers several magnetic atoms are often combined in a ferromagnetic (or at least ferrimagnetic) coupling.

The most famous SMM is the Mn_{12} molecule, named after its core of 12 Manganese atoms which are carrying the spin (more in section 4.3). As typical for molecular magnets different "versions" of Mn_{12} exist, with varying ligands customized for different chemical environments. Other molecular magnets consisting of several identical metal atoms include various Mn compounds from Mn_4 [40] and the high anisotropy Mn_6 [41] up to Mn_{84} [42] as well as SMMs based on other metals like Fe_8 [43]. Furthermore, heterometallic molecular magnets exist like Cr_7Ni, where the individual spins are coupled antiferromagnetically and thus atoms of different spin are necessary to form a non-zero spin state with an even number of atoms (more in section 4.5). A more simple form of molecular magnets avoids the coupling of spins by containing just one metal atom shielded by an organic surrounding as e. g. in Terbium phthalocyanines [44].

The motivation to study SMMs can be described from two perspectives:

Technologically, magnetic materials have been used for data storage since decades and magnetic tape was in use even before the invention of the computer. The basic principle of magnetic storage has remained essentially unchanged since then, albeit the size of each bit has seen a tremendous decrease over time. For storing information a layer of ferromagnetic material is divided into sectors each representing one bit. The two states of that bit ("0" or "1") are represented by different directions of the magnetic moment of that sector. The bit size is usually described inversely as aerial storage density, which has increased from 100 Mbit/in^2 in 1990 [45] up to 600 Gbit/in^2 in 2010 for commercial hard drives, the latter implying a cell size of only 1000 nm^2 [46]. Future cell sizes are approaching the stability limit for thermal fluctuations and products announced for the next years reaching 1 Tbit/in^2 are using heat-assisted magnetic recording (HAMR) [47] to allow the use of high coercivity materials, which are otherwise not recordable with practical magnetic fields.

In summary, the rapid increase in storage densities will encounter physical limits of miniaturization, which will require the use of new concepts and materials. A slow-down in the increase of storage density due to this effect is already occurring [46].

Since molecular magnets are nm-sized magnets, they are possible candidates for magnetic data storage beyond the superparamagnetic limit of regular ferromagnets. Application-oriented research often focuses on increasing the anisotropy barrier height to reach longer relaxation times at usable temperatures. Magnetic relaxation in quantum

systems like SMMs occurs not only through thermal processes, but can also be induced by tunneling of magnetization, which can be impeded by an appropriate design of the magnetic energy states of the molecule.

After 20 years of research in molecular magnets the blocking temperatures of SMMs (the upper temperature limit for a desired minimum relaxation time) remains far away from room temperature, so that long-term magnetic storage as in conventional hard drives has partially moved out of focus. Especially as alternatives like bit-patterned media [48] or the racetrack memory [49] seem closer to application. A more promising scenario for the use SMMs is the entanglement of several molecular magnets for the use in quantum computation.

From a more scientific (and less technological) point of view SMMs combine the macroscopic properties of magnets with the quantum properties of nanoscale objects. This makes them ideal candidates for studies aimed at understanding the limits of validity of quantum mechanics. As systems of several coupled spins they are complex enough to give rise to new types of properties like quantum tunneling of magnetization [50], quantum coherence through Néel vector tunneling [51, 52], or quantum phase interference [53]. However, the number of coupled spins is small enough to allow the observation and manipulation of individual quantum states (rather than band structures), which makes SMMs ideally suited for studies of coupled spin systems.

Beneficial for applications as well as fundamental studies is the molecular nature of SMMs, which makes them identically reproducible units, with a high control over selective properties. Chemical synthesis allows the tuning of their magnetic and chemical properties, in principle including self-assembly as a more economical way of production. Molecular magnets often arrange in single crystals with no magnetic interaction between the molecules, so that quantum behaviour can be observed in a macroscopic object, making it accessible to a wide variety of methods.

While the magnetism of a molecular magnet does not require any neighbouring spins, it can still be influenced by its immediate surrounding: either by affecting the spin of its magnetic atoms through charge transfer or by changes of the intramolecular spin-coupling through chemical reactions changing the SMM's structure. While in principle the core-shell structure of many SMMs protects the magnetic core from such influences, the handling of individual SMMs like the deposition on surfaces or application of contacts is a very active field of research and required for both applications as well as new types of experiments.

4.2. Spin-Flip Spectroscopy

The STM allows to study the spin of individual atoms or molecules. Besides the observation of a Kondo resonance as a rather indirect method (see chapter 5), or the use of spin-polarized STM [54], the direct excitation of spin transitions by STM has been introduced by Heinrich in 2004 [23]. The so called *spin-flip spectroscopy*[1] is a form of inelastic tunneling spectroscopy (see section 2.2.3), where at bias voltages surpassing a certain threshold transitions in the spin's z-component m are excited, resulting in steps in the tunneling spectra. Thereby spin-flip spectroscopy allows the determination of the g-factor of the involved electrons and access to the energy levels of the magnetic states.

The most simple case is a spin $S = 1/2$ system, which can assume the two states $m = +1/2$ ($\uparrow$) and $m = -1/2$ ($\downarrow$). These two states are degenerate at zero magnetic field and otherwise differ by the Zeeman energy $\Delta E = g\mu_B B$ (see fig. 4.2a) with g as g-factor of the spin system and B as the applied magnetic field. If the bias voltage is sufficient to overcome the Zeeman splitting, an additional tunneling channel opens up, in which a tunneling electron excites the system from $\downarrow$ to $\uparrow$, while simultaneously the electron spin changes from $\uparrow$ to $\downarrow$. This additional channel leads to an increased conductance and thus to a pair of symmetric steps in the $\mathrm{d}I/\mathrm{d}V$-spectra (fig. 4.2d).

Figure 4.2b illustrates the situation for a system with higher spin ($S > 1/2$) and no anisotropy. As before, without magnetic field all states are degenerate, but with magnetic fields they split in $2S + 1$ states with the lowest-lying state having $m = -S$. The Zeeman splitting between two adjacent states is identical to one in the spin-$1/2$ system since neighbouring states always differ by $\Delta m = 1$.

A tunnel electron can excite the system from the ground state into the next higher state, but due to conservation of angular momentum higher excitations are forbidden since an exciting tunnel electron can only flip its spin by $\Delta m = 1$ (from $+1/2$ to $-1/2$). An excitation into higher states can occur via multiple excitation processes, where each involved electron contributes a spin flip of $\Delta m = 1$. This spin pumping requires that consecutive excitations by tunneling electrons occur faster than the spin relaxation times [24].

For a stable magnetic moment (e. g. in memory applications) the system requires magnetic anisotropy, which leads to non-degenerate states even without magnetic fields. The

[1] For higher spin systems ($S > 1/2$), the spin is not actually flipped but just excited into a higher state. Nevertheless the term spin-flip(!) spectroscopy is widely used.

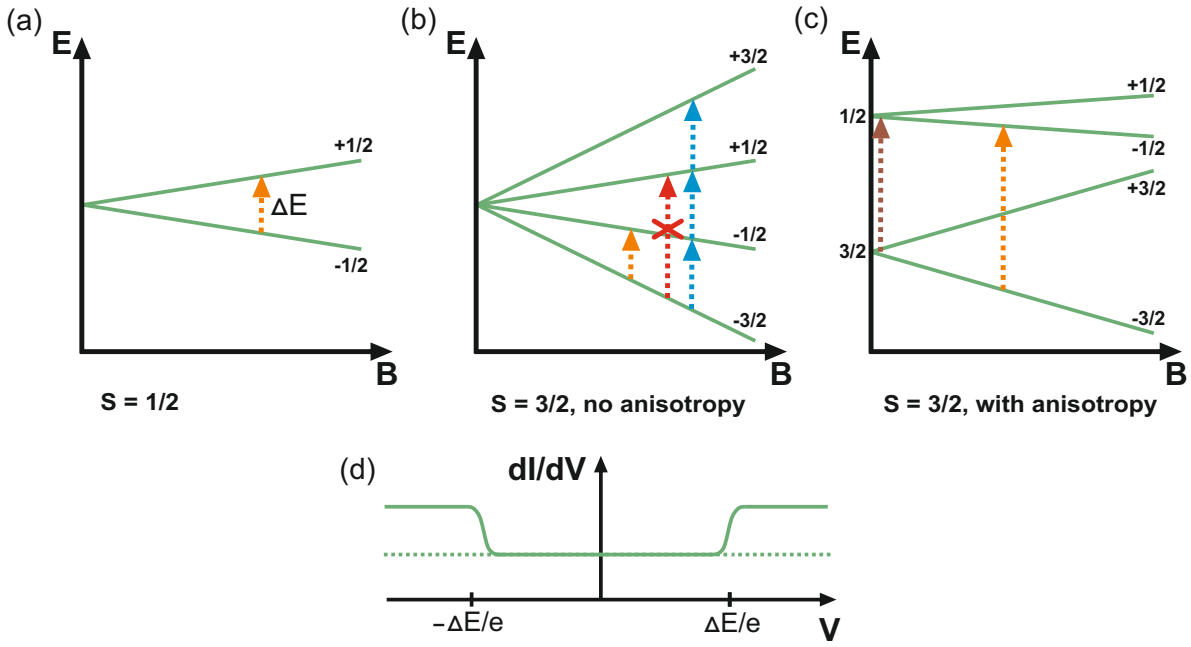

Figure 4.2.: (a-c) Spin Excitation Schemes. (a) In a spin-1/2 system the energy ΔE required for an excitation (orange arrow) depends linearly on the magnetic field. (b) In a system with higher spin ($S > 1/2$) only excitations into adjacent states are allowed (orange arrow). Direct excitations from the ground state into higher states are forbidden (red arrow), but can be achieved through spin pumping (blue arrows). (c) In a system with anisotropy even at zero magnetic field not all states are degenerated, allowing excitations also without magnetic field (brown arrow). (d) The $\mathrm{d}I/\mathrm{d}V$-spectrum in all three examples shows only one pair of excitation steps at $V = \pm\Delta E/e$. Without magnetic field the excitation steps merge together making them invisible in the case of (a) and (b).

spin Hamiltonian including anisotropy in a commonly used form for molecular magnets [55] or magnetic atoms on surfaces [56] is given by

$$H = -g\mu_B \vec{B}\vec{S} + DS_z^2 + E(S_x^2 - S_y^2). \tag{4.1}$$

The first term accounts for the Zeemann energy, the second term describes the axial anisotropy, and the third term specifies the weaker transversal anisotropy. The z-axis is chosen, that the anisotropy constants D and E fulfill $|D| \geq |3E|$ [55].

For the case of axial anisotropy ($E = 0$), the states with different absolute values of m are non-degenerate, allowing excitations also at zero field (fig. 4.2c). As in the case without anisotropy conservation of angular momentum allows only one excitation resulting in one step in the $\mathrm{d}I/\mathrm{d}V$-spectrum. Transversal anisotropy leads to a mixing

of the m-states (individual states are actual superpositions of different m-states). This allows excitations into several excited states leading to multiple steps in the spectra [56].

So far we have discussed excitations of the z-component m of a single spin with a fixed length S. This model is valid for spin-flip spectroscopy on single atoms. To describe the spin state of a molecule, where several spin-carrying atoms are combined, the *giant spin model* can be used. This simplifies the possible combinations of the individual spins by adding them up to one total (giant) spin of fixed length S allowing only excitations in the z-component M of this total spin. By reducing the system to a single spin system, we neglect how the individual spins are arranged to sum up to the different values of M.

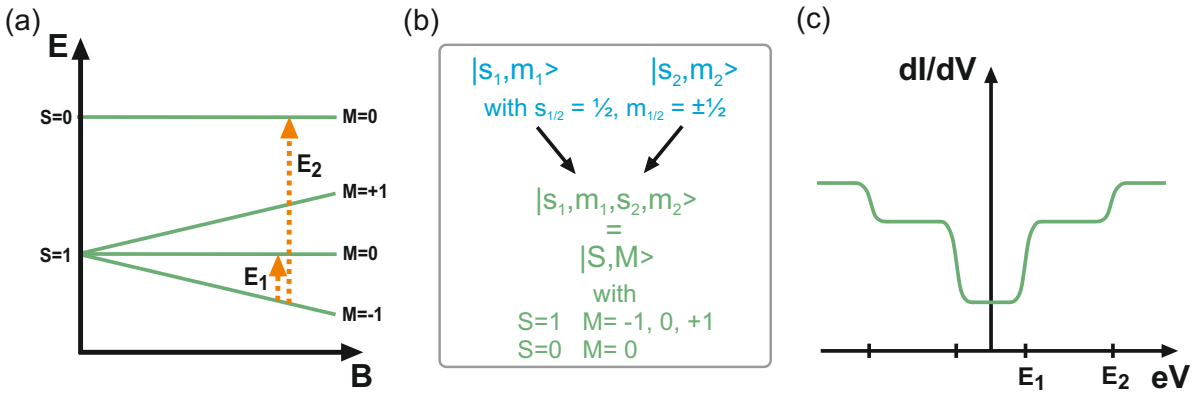

Figure 4.3.: (a) Spin excitation scheme of a giant spin combined of two spin-½ systems. Excitations can either change only M (short arrow) or S and M (long arrow). (b) Overview of the possible states and according quantum numbers when combining two spin-½ systems. (c) Resulting tunnel spectrum with excitation steps at the energies E_1 and E_2. Different transition probabilities of the excitations result in different step heights.

In the following the giant spin model and its limitations towards spin-flip spectroscopy will be illustrated by the example of combining two spin-½ systems. To avoid excessive indices we will use lowercase variables (s, m) for the individual spins and uppercase variables (S, M) for the combined spin system.

We combine two spin-½ systems described by $|s_1, m_1\rangle$ and $|s_2, m_2\rangle$ to a combined state $|s_1, s_2, m_1, m_2\rangle$ (fig. 4.3b). This combined state is again a spin state (obeying the relations for a quantum mechanical angular momentum) and thus can be described by $|S, M\rangle$ with a total spin S and its z-component M. With the individual spins $s_1 = s_2 = ½$ the total spin S can be either $S=1$ or $S=0$ for parallel or anti-parallel alignment. $S=1$ is a triplet state, where M can assume the values $M = \{-1, 0, +1\}$ with the corresponding Zeeman splitting at magnetic fields. The singlet state $S=0$ enforces $M=0$ (fig. 4.3a).

Assuming a ferromagnetic interaction between both spins, the $S=1$ state is energetically favored over the $S=0$ state, resulting in a ground state of $|1,-1\rangle$ at magnetic fields (fig. 4.3a). In the giant spin picture only changes of M are allowed resulting in one possible excitation from $|1,-1\rangle$ to $|1,0\rangle$. If the bias voltage supplies sufficient energy to not only rotate the total spin but to change the interaction between the individual spins, also the excitation from $|1,-1\rangle$ to $|0,0\rangle$ becomes available. This results in multiple steps in the spectra (fig. 4.3c).

Changes of S allow also excitations without changing of the spin of the exciting electron (e.g. $|1,0\rangle \rightarrow |0,0\rangle$). Conservation of angular momentum for the entire system restricts possible excitations to the transition rule $\Delta M = 0, \pm 1$.

Spin-flip spectroscopy has been used to study individual atoms (mostly $3d$ metals like Mn and Fe) on surfaces [23, 56–58] as well as linear chains of atoms [59]. Spin-polarized spin-flip spectroscopy has been used to gain additional information and enable spin pumping of the studied atoms [24,60]. Spin-flip spectroscopy on molecular magnets has been performed e. g. on phthalocyanines containing different metal atoms both on multilayers [61,62] and individual molecules [63].

4.3. Mn_{12}

The Mn_{12} molecule was one of the first molecular magnets discovered and is still one of the most investigated ones today. It is known for its long spin relaxation times, which are heavily temperature dependent with typical time constants of 0.1 s at 5 K and several months at 2 K [64,65]. With slow relaxation times at sufficiently low temperatures a magnetic hysteresis appears [38]. Measurements of Mn_{12} molecules in frozen organic solutions have confirmed the slow relaxation times as a property of the individual molecules [66,67]. Hysteresis loop measurements on crystals of Mn_{12} molecules show evenly spaced steps (see figure 4.1b), which are exemplary signatures for quantum tunneling of magnetization [50,68].

The full structure of Mn_{12}-acetate$_{16}$, the most common type of Mn_{12}, can be seen in figure 4.4a and is described as $Mn_{12}O_{12}(CH_3COO)_{16}$. It was first synthesized and characterized by Lis in 1980 [69]. It consists of a magnetic $Mn_{12}O_{12}$ core surrounded by 16 acetate groups, which shield the magnetic core from substrates or neighbouring molecules. The 12 Mn atoms are arranged in an inner ring of four atoms with the oxidation state Mn^{4+} and an outer ring of eight atoms with the oxidation state Mn^{3+}.

With the Mn^{4+}-atoms having a spin of 3/2 and the Mn^{3+}-atoms having a spin of 2, a maximum total spin of $S = 22$ would be possible. Susceptibility measurements have shown a total spin of $S = 10$ instead, suggesting a ferrimagnetic spin arrangement [37]. In the simplest picture the spin $S = 10$ ground state can be explained by assuming all Mn^{3+}-spins to point up and all Mn^{4+}-spins to point down, which has been confirmed by neutron diffraction [70].

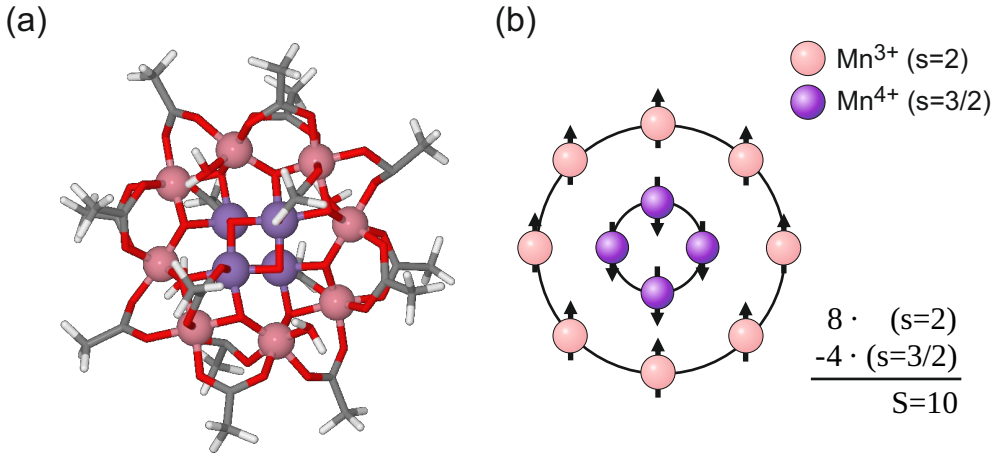

Figure 4.4.: (a) Structure of the Mn12 molecule. Balls represent Mn atoms of the two different oxidation states Mn^{3+} (pink) and Mn^{4+} (violet). Red (gray, white) sticks represent bonds to oxygen (carbon, hydrogen). (b) All Mn atoms of the same oxidation state (and thus identical spin) bond ferromagnetically while the atoms of a different spin state bond antiferromagnetically resulting in a spin ground state of $S = 10$.

Like many other molecular magnets, Mn_{12} actually describes a whole family of different Mn_{12} derivates. The acetate groups (CH_3COO) can be replaced by other ligands to obtain different chemical functionality [55]. Different ligands affect the interaction of a Mn_{12} molecule with the substrate, which can again alter the magnetic properties of the molecule [71–73]. Using a new combination of deposition technique and substrate we have chosen Mn_{12}-acetate for our experiments as the principal and most studied derivate of the Mn_{12} family.

A key property of all molecular magnets is that their magnetism is a property of the molecule itself and no interaction between several molecules is necessary for these phenomena to occur. Nevertheless almost all information about Mn_{12} are based on measurements on ensembles of molecules, usually in powder or single crystal form. Even though its core-shell structure should inhibit interaction between several molecules and measurements in solutions suggest no dependance on neighbouring molecules [66, 67],

the most elegant proof, a measurement of the magnetic moment on a well separated, individual Mn_{12} molecule was so far missing.

Two experimental approaches to study the magnetic properties of individual Mn_{12} are feasible: Transport measurement in a single molecular transistor setup or the use of scanning tunneling spectroscopy.

Transport measurements conducted on Mn_{12} molecules in a transistor setup contacted by gold electrodes showed current suppression on the energy scale of the anisotropy barrier [74] as well as a Zeeman splitting increasing with magnetic field [75]. While the results of both works can be interpreted as signatures of magnetic molecular states, variations between different devices hinder a straightforward interpretation and the conclusions remain qualitative. As usual for this type of measurements, molecules were deposited by applying solutions to the pre-defined gate setups with no further means to verify that the Mn_{12} molecules remain intact or do not aggregate into larger clusters.

In principle STM/STS studies can show detailed information about the environment of deposited molecules and can verify the structural integrity of Mn_{12} molecules before engaging spectroscopy. The primary challenge in STM studies has been the intact deposition of Mn_{12} on a (conductive) substrate without altering the magnetic properties. In the last 10 years intensive research was conducted to deposit different Mn_{12} derivates on various surfaces with Au(111) as the most common substrate [76]. The thermal instability of Mn_{12} [77] hinders the direct in-vacuo deposition and has resulted in the use of wet chemistry deposition methods, which are, like any methods at ambient conditions, impaired by frequent contamination.

While several STM studies on thin layers of Mn_{12} have been performed [71, 72, 78–80], detailed topographic information on molecular structure or self-organized ordering is still missing and single molecule spectroscopy has not been published at all. X-ray methods on thin films have rather shown that the Mn atoms undergo a reduction showing the presence of Mn^{2+} on gold surfaces [72, 73], suggesting changes of the molecular magnetic moment.

A different deposition approach has been used by the group of O'Shea, who used electrospray deposition as a non-thermal UHV deposition method [81]. While they achieved a moderately clean deposition of Mn_{12} on a Au surface and STM imaging suggests no fragmentation of the molecules, they also confirmed the reduction of the Mn inside the Mn_{12} molecules.[2]

[2] Very recently they achieved the preservation of the original oxidation states on Au surfaces by using Mn_{12} molecules with particular large ligands [82].

4.4. STM Studies on Individual Mn_{12} Molecules

4.4.1. Motivation

To reach the goal of observing the magnetic properties of an individual Mn_{12} molecule, we combine two sophisticated techniques, which are both available within the nanoscale science department of Prof. Kern at the MPI in Stuttgart: For sample preparation we use electrospray ion beam deposition as an in-situ UHV technique which offers excellent control of the adsorbates through mass selection prior deposition. In contrast to the traditionally used solution-based techniques it does not rely on the chemical properties of the surface allowing also a freer choice of substrates. Measurements on individual molecules are performed by STM to obtain topographic information and by STS to observe spin-flip excitations as a signature of molecular magnetism.

Measurements have been performed on Au(111) substrates and on a thin decoupling layer of boron nitride (BN) on a Rh(111) surface to avoid the reduction of the Mn atoms through contact with metal surfaces. While we obtained image data on both substrates of unprecedented quality, spectroscopic signatures of spin-flip excitations could only be observed on the decoupling layer.

Thereby this study presents the first observation of the magnetic moment of an individual Mn_{12} molecule in a well defined environment. Opposing to the work on single molecular transistors, the STM enables us to verify the intactness of a single molecule and to rule out the aggregation of several molecules. We successfully demonstrate the use of a BN monolayer as decoupling layer to avoid the spin altering reduction of the Mn atoms on metal surfaces. This work also represents the first low-temperature STM study of Mn_{12} molecules in general.

The following results have been published in *Nano Letters* in 2012 as an article named "The Quantum Magnetism of Individual Manganese-12-Acetate Molecular Magnets Anchored at Surfaces" [83].

4.4.2. Deposition

Deposition Setup

We use electrospray ion beam deposition (ES-IBD) as deposition method to bring Mn_{12} molecules on atomically well defined metal and ultra-thin insulating surfaces. This technique has been demonstrated to be a gentle method for the deposition of large organic molecules in vacuum [84–87]. The employment of ion optics, current detection and mass spectrometry allows complete control over all experimental parameters, most

importantly the chemical composition and the amount of deposited material. These attributes make ES-IBD an ideal technique for the preparation of samples for scanning probe microscopy in UHV. Depositions have been performed by members of the ESI group inside the nanoscale science department at the MPI, primarily by Zhitao Deng, Nikola Malinowski, and Stephan Rauschenbach.

Electrospray ionization (ESI) is a technique to generate molecular ions by dispersing charged droplets of a solution of the analyte into vacuum. The drying droplets undergo subsequent Coulomb explosions that finally lead to the molecular ions. Due to the absence of heating, as opposed to the more common technique of thermal evaporation, this technique allows the ionization of thermally unstable molecules and became a widely used ionization source for mass spectrometry.

Electrospray ion beam deposition (ES-IBD) uses the same ionization principle but directs the molecular ion beam onto a substrate for deposition. Thus, ES-IBD setups typically resemble ESI mass spectrometers with additional features, e. g. additional deposition chambers and sample holders. A schematic of the home build setup used in this experiment is shown in fig. 4.5. Since the ESI source operates at ambient pressure, differential vacuum pumping is required to reduce the pressure along the ion beam down to 10^{-11} mbar (UHV).

A solution of Mn_{12} molecules in acetonitril is fed into a spray needle, which generates charged droplets at ambient pressure. These droplets are mixed with a much higher flow of nitrogen at a temperature of 150 °C as a curtain gas to facilitate faster droplet evaporation. The ions created in the electrospray pass a capillary and expand with the carrier gas into the first vacuum stage. The dc-voltages applied to the back-end of the capillary and the ion funnel define the declustering potential (V_{decl}). This is a measure for the intensity of the collisions of the ion beam with the neutral background gas, which are used to break apart cluster ions or create molecular fragments. Usually V_{decl} is in the range of $100 - 400$ V.

To achieve a clean, mass-specific deposition, a quadrupole is used as mass selective ion guide. This allows the separation of intact Mn_{12} molecules from molecular fragments, solvent molecules, and other contaminations. It is followed by a time-of-flight (TOF) mass spectrometer used to assess the chemical composition of the ion beam and adjust the aforementioned mass selection. The spectrometer is mounted on a z-travel and can be retracted from the beam axis for the actual deposition. The instrument can detect positive and negative ions and has a resolution of $m/\Delta m = 300$, which is sufficient to confirm the intactness of a molecular species.

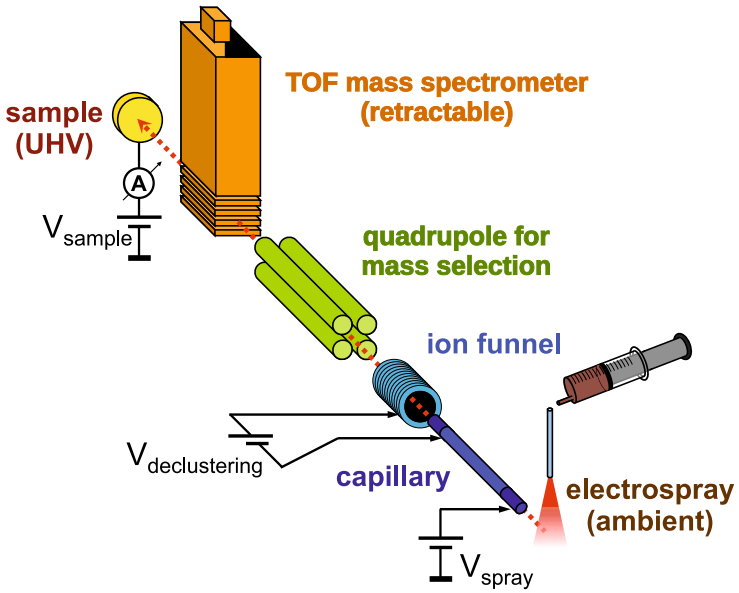

Figure 4.5.: Schematic of the ES-IBD setup. The ions created at the electrospray source at ambient pressure are fed into the vacuum system through a capillary. After mass selection the ion beam is either directed into a mass spectrometer for analysis or onto the sample surface for the actual deposition.

Samples where prepared in two different sample holders during this study, both located in the UHV pumping stages of the system. For quick measurements, as to check the correct deposition parameters, samples can be transferred to a commercial Omicron STM directly connected to the ESI-BD setup, which operates from room temperature down to 40 K. For spectroscopic measurements and high resolution imaging the STM described in detail in chapter 3 has been used. Besides general higher stability this STM can be operated at temperatures down to 1.5 K and under magnetic fields. To enable sample transport between both machines under continuous UHV conditions, a portable vacuum suitcase was developed. The sample holders for both machines are equipped with electrodes to accelerate or decelerate the incoming beam allowing a soft landing of the molecules. Additional current measurement offers precise control of the flux and thus the coverage.

Deposition Results

Mn_{12} molecules have been deposited on three different substrates: Cu(001), Au(111), and a monolayer of BN on Rh(111). Metal samples are prepared by repeated Ar^+ sputtering and thermal annealing. The BN/Rh samples are prepared as described in appendix A. Cu(001) substrates are only used for test measurements at room temperature due to

an expected low mobility of Mn_{12} since the rectangularly ordered (001)-surface is not as densely packed as a hexagonal (111)-surface. No spectroscopy is performed on this substrate.

The ES-IBD setup allows the analysis of the molecular ion beam prior deposition by mass spectrometry to check for contaminations or fragmented molecules. Mass spectra for different declustering potentials ($V_{\mathrm{decl.}}$), a parameter which adjusts the collision energy between the ion beam and the background gas, are shown in figure 4.6a. In all cases the Mn_{12} ion beams contain a certain amount of contamination, typically by one more or one less acetate group attached to the molecule. While at low $V_{\mathrm{decl.}}$ a peak corresponding to $Mn_{12}Ac_{17}^{1-}$ is found besides the intact Mn_{12} molecule, at high $V_{\mathrm{decl.}}$ the loss of acetate groups is the main source of defected molecules. For deposition a $V_{\mathrm{decl.}}$ of 150 V has been used. Contaminations of very low mass (below a few hundred) are already separated off by the ion optics before reaching the mass spectrometer.

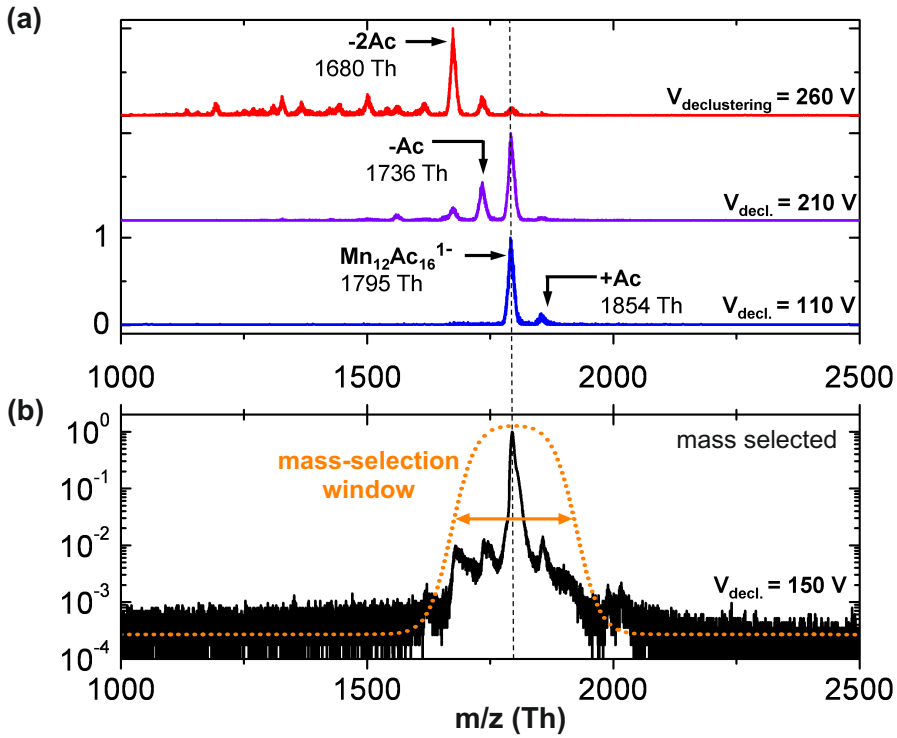

Figure 4.6.: (a) Mass spectra show the intact molecule (1796 Th) and fragments due to acetate loss (1737 Th, 1678 Th) for different declustering potentials. (b) Mass spectrum of a mass selected beam at $V_{\mathrm{decl.}} = 150$ V for deposition (log scale). The total contamination by fragmented molecules is suppressed to less than 5% intensity. The shape of the mass selection window is only qualitative.

To decrease contaminations the Mn_{12} ion-beams were mass selected using the quadrupole ion guide. Due to the small relative mass differences between defect and intact molecules, the mass selection can not be set to completely suppress the deposition of defect molecules without reducing the intensity of the intact species. With the resolution of the quadrupole ($m/\Delta m \approx 50$) the contaminations can be reduced below 5% intensity (figure 4.6b). STM images of depositions with and without mass selection can be seen in figure 4.7.

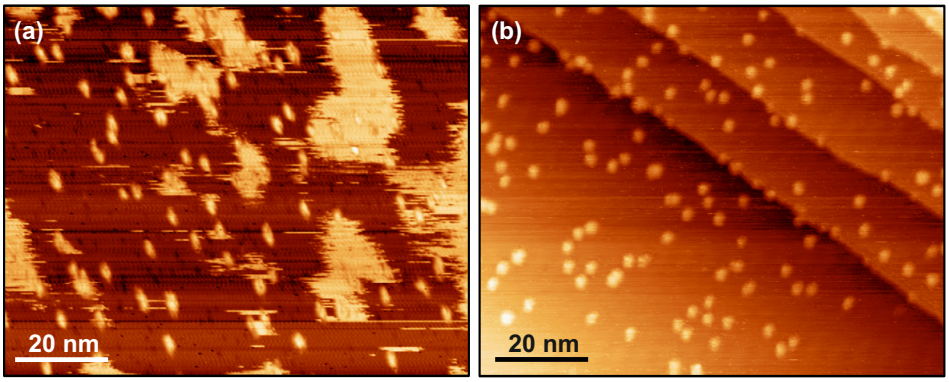

Figure 4.7.: Mn_{12} deposited on Cu(001) with and without mass selection. (a) Without mass selection individual Mn_{12} molecules can be identified, but also other material has been deposited and has agglomerated into larger patches. Contaminations on the surface interact with the tip resulting in unstable tunneling conditions (horizontal lines). (b) With mass selection enabled only Mn_{12} molecules are deposited.

To further ensure the intact deposition of the fragile molecules the ion beams were decelerated by applying an appropriate voltage to the sample. Typically, Mn_{12} ion beams with an initial kinetic energy of $25 - 30$ eV were decelerated and deposited at energies below 5 eV. During the deposition the ion current was monitored, which allows a precise adjustment of the molecular coverage. In our sample geometry a deposited charge of 350 pAh corresponds to a molecular monolayer. With mass selected beams of $20 - 200$ pA the full monolayer is achieved within several hours, however, much lower coverage is desirable for addressing individual molecules with STM. After a desired coverage has been deposited, the sample is transferred in-situ into the STM – either directly or via the vacuum suitcase.

4.4.3. STM Imaging

After room temperature deposition of Mn_{12} molecules on Cu(001), Au(111), and a monolayer of BN on Rh(111) we obtain STM topographies. On Cu(001) randomly distributed

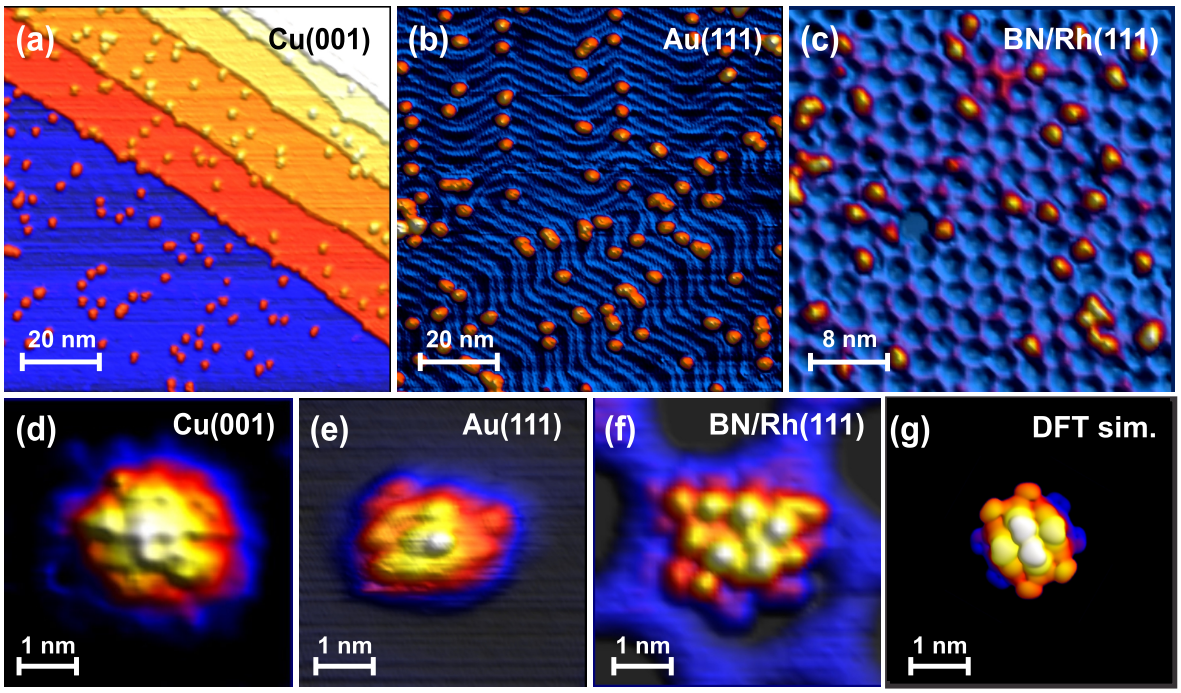

Figure 4.8.: **STM topographic images of Mn_{12} molecules deposited on different surfaces.** (a) On Cu(001) immobile molecules are randomly distributed over the surface at 300 K. (b) On Au(111) molecules are found preferably at the elbow sites of the herringbone reconstruction ($T = 40$ K). (c) On the BN/Rh(111) surface molecules adsorb in the depressions of the BN corrugation ($T = 1.5$ K). (d-f) images of individual molecules reveal an intramolecular structure identified as the acetate groups. Different adsorption geometries can be observed. (g) comparison with the DFT calculation of the free molecule (calculations by Duy Le, University of Central Florida). Tunneling parameters: **a**: $V = +2$ V, $I = 100$ pA, **b**: +2 V, 80 pA, **c**: +0.9 V, 100 pA, **d**: +2.5 V, 120 pA, **e**: +2 V, 80 pA, **f**: −1 V, 45 pA.

molecules have been observed (fig 4.8a) meaning that Mn_{12} is immobile at room temperature. In contrast, on Au(111) the molecules are mobile and can be imaged stably only after cooling down to 40 K. At low coverage they preferably occupy the fcc part of the Au(111) surface reconstruction starting at the elbow sites (fig 4.8b).

In contrast to bare metal surfaces, the BN monolayer on Rh(111) is chemically very inert and has shown to be an excellent electronic decoupling layer (see Appendix A). The deposition of Mn_{12} on the BN surface results in a random distribution of individual molecules in the depressions of the BN corrugation (fig 4.8c).

On all surfaces we identify individual molecules from their size of $(2.3 \pm 0.4) \times (1.9 \pm 0.4)$ nm^2 and a voltage dependent apparent height between 0.25 nm and 0.7 nm [79, 81]. Detailed imaging of the molecules (fig 4.8d–f) shows good agreement to an intact molecule, simulated by density functional theory (DFT) calculations (fig 4.8g). The characteristic sub-molecular structure with lobes of approximately 0.5 nm size corresponds to the acetate groups of the SMM as seen in DFT. Calculations have been performed by Duy Le, member of the group of Prof. Talat Rahman, University of Central Florida.

4.4.4. Spectroscopic Results

To address the question whether these molecular magnets can retain their magnetic properties upon deposition, we have applied spin-flip spectroscopy at 1.5 K to the molecules on BN/Rh and Au substrates. The differential conductance $\mathrm{d}I/\mathrm{d}V$ was measured by placing the tip above the center of the molecules and detecting the lock-in signal (fig 4.9a). The resulting spectra showed symmetric steps around the Fermi energy only for molecules on the BN insulator.

Figure 4.9d shows the obtained $\mathrm{d}I/\mathrm{d}V$-spectra at zero and with applied magnetic field. The spectra show three distinct steps, where the innermost step is usually the most prominent one and can be found at $1 - 2$ meV, while the outer steps can be observed in a range up to 16 meV. The steps in $\mathrm{d}I/\mathrm{d}V$-signal correspond to peaks in the numerically derivated $\mathrm{d}^2I/\mathrm{d}V^2$, which have been used for easier attribution of the step positions (fig 4.9d). For Mn_{12} molecules deposited on Au(111) surfaces we did not observe such features presumably due to the quenching of the spin.

Before and after the spectra on the molecules have been measured, reference spectra have been taken on the substrate to ensure a featureless conductance of the tip. The $\mathrm{d}I/\mathrm{d}V$-curves have been obtained with the lock-in technique using modulation voltages of $0.5 - 1$ mV.

To interpret these features we omit for the moment the many spin nature of the system by using the giant spin approximation in which $S = 10$ is fixed. The magnetic anisotropy is responsible for the zero-field splitting of the spin eigenstates in the z-projection M and leads to a degenerate ground state for $|S, M\rangle = |10, -10\rangle$ and $|10, 10\rangle$ (fig 4.9b). The model with fixed S reduces possible magnetic excitations to changes of M, and – obeying the transition rule $\Delta M = 0, \pm 1$ – allows only one excitation from the ground state: from $|10, \pm 10\rangle$ to $|10, \pm 9\rangle$. The energy difference between these two states is given by the anisotropy term of the Hamiltonian (equation 4.1) as $10^2D - 9^2D$. Us-

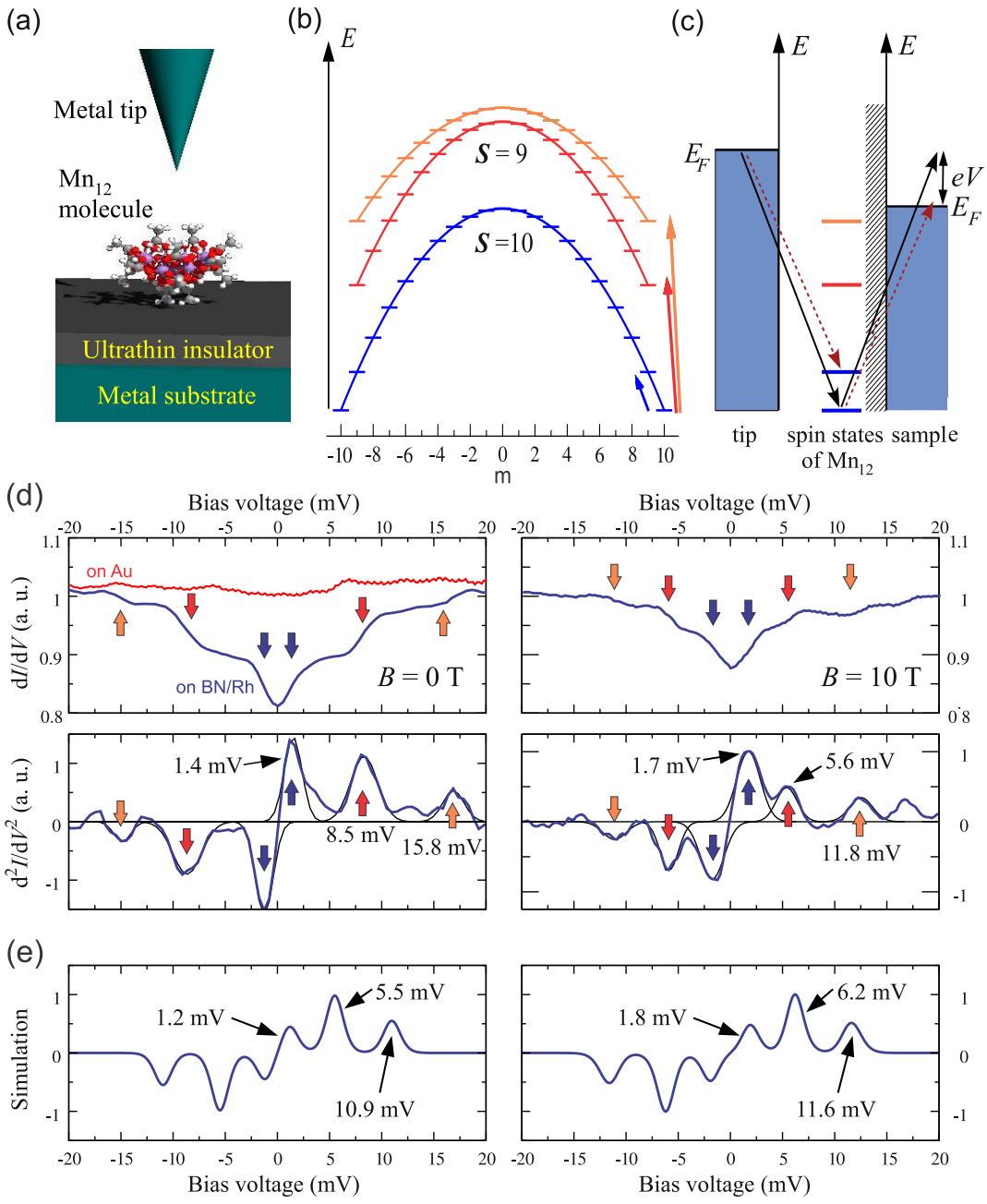

Figure 4.9.: **Tunnel spectroscopy on individual Mn_{12} molecules adsorbed on BN/Rh(111).** (a) Schematic of the tunneling geometry. (b) Schematic energy diagram of a Mn_{12} molecule in the giant spin approximation with $H = DS_z^2$ and $D < 0$ without magnetic field. The two upper curves represent two different arrangements of the atomic spins to reach $S = 9$. Arrows indicate possible excitations which obey the spin selection rule $\Delta M = 0, \pm 1$. (c) Co-tunneling processes between the metal tip and the BN/Rh sample via the Mn_{12} molecule. Full arrows: elastic tunneling; dashed red arrows: inelastic tunneling process which excites the internal spin system of the Mn_{12}. (d) Typical dI/dV and d^2I/dV^2 spectra ($V_{set} = 100$ mV, $I_{set} = 20$ pA, $T = 1.5$ K of a Mn_{12} molecule adsorbed on a BN/Rh surface at $B = 0$ T (left) and $B = 10$ T (right) reveal low energy spin-flip excitations which manifest themselves as steps (peaks) in the dI/dV (d^2I/dV^2) spectrum (blue lines). For comparison Mn_{12} on Au(111) does not show these features (red line in the top left panel). (e) Simulated d^2I/dV^2 spectra using the 8-spin model.

ing an anisotropy constant of $D = -57\ \mu$eV known from bulk measurements [88], we obtain a value of 1.1 meV for this transition, which is consistent with the innermost step.

To explain also the outer steps, we need to go beyond the giant spin model to cover all possible magnetic excitations. We calculated excitation spectra by using a Hamiltonian in which the spin of each individual Mn atom inside the Mn_{12} interacts with its neighbours and the magnetic field $\vec{B}$. Parameters for the Hamiltonian have been obtained from the literature and by using density functional theory calculations.

4.4.5. Calculation of Spectra

Density Functional Theory

Density functional theory (DFT) is used to calculate the electron and spin density of the Mn_{12}-acetate molecule on one layer of BN, in order to obtain the coupling constants between different atoms of the molecule and to evaluate the effect of the BN onto the Mn_{12}-molecule. Calculations have been performed by Duy Le, member of the group of Prof. Talat Rahman at the University of Central Florida. In detail the VASP package [89] was applied with the Perdew-Burke-Ernzerhof (PBE) exchange-correlation functional [90] and the projector augmented-wave method [91, 92].

For simulating a Mn_{12}-acetate on a BN substrate, a supercell consisting of a flat 8×8 unit cells large h-BN layer was assumed and a single Mn_{12}-acetate molecule was placed above it (fig. 4.10a,b). The structure of the molecule was relaxed by using the conjugate gradient algorithm until the forces acting on each ion were less than 0.01 eV/Å. To take strong electron-electron correlation effects on the 3d Mn atoms into account the generalized gradient approximation (GGA+U) [93] is used with an on-site Coulomb repulsion energy on the Mn atoms of $U = 5.1$ eV, which corresponds to the observed local magnetic moment. The lattice parameter of the BN sheet is optimized to be 2.51 Å.

To make the simulation of the surface and molecule feasible, we assume that the acetate ligands are still intact and that the molecule is not relaxing internally when approaching the surface. Within this approach, the optimized distance from center of mass of the Mn_{12} molecule to the BN sheet is about 9.1 Å, resulting in an absorption energy of about 25 meV (fig. 4.10c). It is important to stress that van der Waals interactions are not taken into account, since the theory of this part of the interaction for spin-polarized systems is not well understood so far. However, we expect that this interaction will lead to a slight decrease of the molecule-substrate distance and an appreciable increase of the interaction energy between the molecule and the sheet.

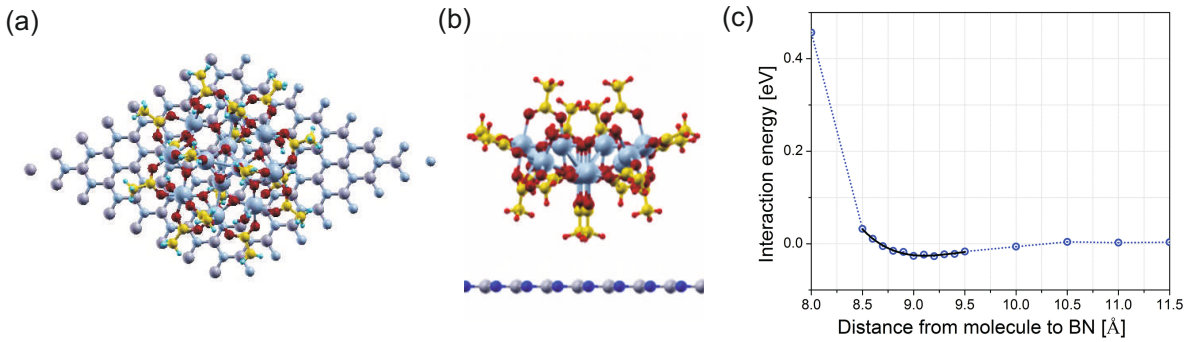

Figure 4.10.: Top view (a) and side view (b) of the structure used for the DFT calculation consisting of a single BN sheet and the Mn_{12} molecule. (c) Total energy of the Mn_{12}/BN system as function of the molecule center-of-mass layer separation. The circles connected by the dotted curve represent calculated data, the black line shows the fitting to a 3rd-order polynomial. The lowest energy configuration corresponds to a distance of 9.1 Å and a binding energy of 25 meV.

An important result of this analysis is that at distances between 8 and 11.5 Å, the spin density distribution on the Mn_{12} molecule is practically identical to the case with no substrate. This result indicates that within the limitations of this model the BN does not affect the electronic state of the Mn_{12} when the molecule physisorbs to the surface, preserving its magnetic properties.

STM images are simulated using the Tersoff-Hamann approach. We calculate the local density of states (LDOS) to extract contributions from bands whose eigenvalues lie in the range from E_F to $E_F + eV$ where E_F is the Fermi level and V the bias voltage applied to the sample in experimental STM. With this definition, when V is positive, the unoccupied local density of state on the Mn_{12} molecule is probed in the calculation. The Fermi level is defined as the center of the HOMO–LUMO gap and lies −4.8 eV below the vacuum level.

Figure 4.8g shows a simulated STM image, with a LDOS isosurface of $10^{-5}e/Å^3$ and $eV = 2.5$ eV. These simulations agree well with the measured topographies also for the negative bias $eV = -2$ eV (not shown). Isosurface values in the range of $10^{-3} - 10^{-5}e/Å^3$ do not significantly change the simulated image.

Spin Excitation Calculation

To simulate spin excitation spectra we determine the appropriate Hamiltonian to describe the coupled spin system of the Mn_{12} molecule and calculate its eigenvalues and

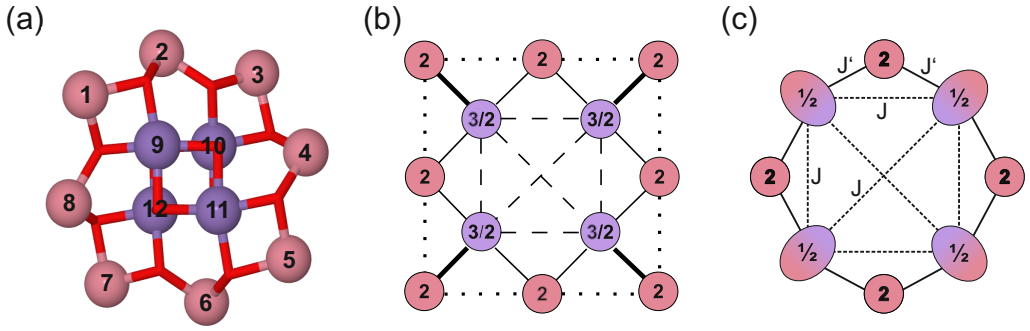

Figure 4.11.: (a) Magnetic core of the Mn_{12}-acetate molecule. The 12 Mn atoms are coupled via oxygen bridges (red bars). (b) The strength of the magnetic coupling between the different Mn atoms varies. The largest coupling exists between the corner $s = 2$ and the inner $s = 3/2$ atoms (thick line). This strong antiferromagnetic coupling allows simplification of the model by replacing the coupled pairs by an effective $s = 1/2$ site (c).

-vectors to gain the energy spectrum of the spin system. Since we are only interested in spin excitations the used Hamiltonian omits non spin-related effects like molecular vibrations or Coulomb scattering.

The magnetic core of the Mn_{12}-acetate molecule contains 12 Mn atoms which are coupled via superexchange by oxygen bridges (see fig 4.11a). The eight outer atoms have thereby a spin $s = 2$ while the four inner atoms have a spin $s = 3/2$ (fig 4.11b). For a more feasible eigenstate calculation we use a simplified 8-site Hamiltonian which reduces the matrix size from 10^8 to acceptable 10^5 and in which the exchange interaction of the four antiferromagnetically coupled dimers with the strongest coupling ($1-9$, $3-10$, $5-11$, $7-12$ in fig 4.11a) are approximated by four spins $s = 2 - 3/2 = 1/2$ (fig 4.11c) [94–96]. This can be done because the exchange interaction inside these dimers is much larger than all other exchange interactions and larger as the energy range of interest in our experiment. Thus, the four $s = 1/2$ "dimer" spins interact with each other and the remaining four $s = 2$ spins (sites 2, 4, 6, and 8).

Following reference [96] we regard 3 types of exchange interactions in this system:
(I) Easy-axis anisotropy on the individual spins

$$\hat{H}_{\text{ani}} = K_z (s_z^i)^2, \tag{4.2}$$

with K_z as the anisotropy term which is only relevant at the $s = 2$ sites, since the $s = 1/2$ sites are degenerate in m without magnetic fields due to Kramer's degeneracy theorem.

(II) Direct Heisenberg spin-spin interaction

$$\hat{H}_{\mathrm{J}} = J_{ij}(\vec{s^i}\vec{s^j}), \tag{4.3}$$

which couples different spin sites isotropically and has in the 8-spin model two distinct strengths: A relatively strong coupling J' between the $s = 2$ and $s = 1/2$ sites and a weaker coupling J between the more distanced $s = 1/2$ sites. The even weaker coupling between the $s = 2$ sites can be neglected [96].

(III) Dzyaloshinsky-Moriya interactions

$$\hat{H}_{\mathrm{DM}} = \mathbf{D}_{ij}(\vec{s^i} \times \vec{s^j}), \tag{4.4}$$

in which the Dzyaloshinsky-Moriya vector parameter D couples neighbouring $s = 2$ and $s = 1/2$ sites.

The total Hamiltonian including the Zeeman energy results then into

$$\hat{H}_{\mathrm{total}} = \sum \hat{H}_{\mathrm{ani}} + \sum \hat{H}_{\mathrm{J}} + \sum \hat{H}_{\mathrm{DM}} + \sum g\mu_B \vec{s^i}\vec{B}, \tag{4.5}$$

with $\vec{B}$ as the applied magnetic field.

We used the three sets of parameters from Katsnelson (Katsnelson A-C in table 4.1) to create and solve the matrix system [96]. In addition we have used a set of parameters, which follow from the DFT calculation. For this we calculate the change of total energy when one of the $s = 2$ spins is flipped from $+m$ to $-m$ (see fig. 4.12). We found an energy difference of $\Delta E_{02} = 0.038$ eV which corresponds to $4J'$ when neglecting the easy axis anisotropy. This value of $J' = 0.0095$ eV $= 110.2$ K is close to that of Katsnelson A approximation (see table 4.1). Thus, we use K_z and D from this approximation. The value of J cannot be determined directly from DFT calculations because we use the 8-spin model. However, we use the value of $J = 3$ K which reproduces correctly the lowest excitation energy and which follows from the estimation of the change of the en-

Approximation	J [K]	J' [K]	K_z [K]	D_x [K]	D_y [K]	D_z [K]
Katsnelson A	0	105	5.69	25	0	-1.2
Katsnelson B	23.8	79.2	5.72	22	0	10
Katsnelson C	41.4	69	5.75	20	0	10
Our results	**3**	**110.2**	5.69	25	0	-1.2

Table 4.1.: Coupling parameters from the literature [96] and our values determined by the DFT calculation.

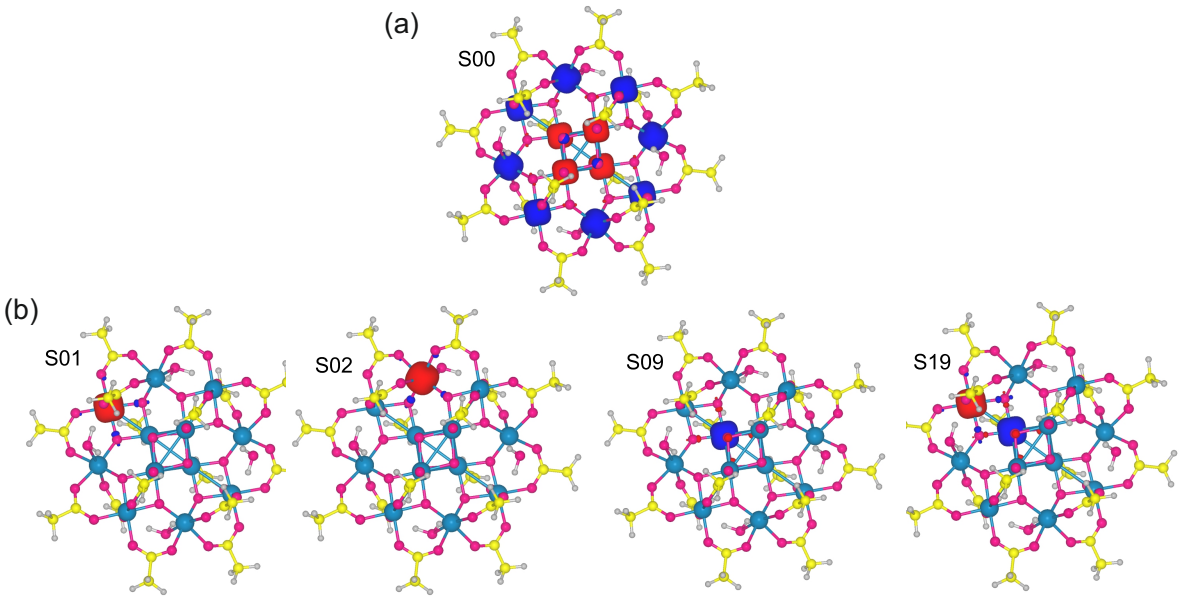

Figure 4.12.: (a) Spin-resolved density of states on the Mn_{12}-acetate molecule in the ground state (S00). Blue (red) spheres correspond to spin-up (spin-down) accumulations. (b) S01: Change of the spin-density compared to the ground-state S00 after flipping the spin of atom no. 1 (equivalent to 3, 5, and 7). The energy difference is $\Delta E_{01} = 0.078$ eV. S02: Same for flipping atom no. 2, 4, 6, or 8 with $\Delta E_{02} = 0.038$ eV. S09: Same for flipping atom no. 9 to 12 with $\Delta E_{09} = 0.064$ eV. S19: Combined flipping of one pair (atom 1 and 9) with $\Delta E_{19} = 0.119$ eV.

ergy calculated from the Heisenberg Hamiltonian by flipping one spin. Our DFT results validate the parameters chosen by Katsnelson in their model A.

We continue by calculating the inelastic spin-flip transition matrix elements $Y_{i,f}$ using Fermi's golden rule

$$Y_{i,f} = \langle \psi_f, \sigma_f | \hat{S} \cdot \hat{\sigma} | \psi_i, \sigma_i \rangle, \tag{4.6}$$

with $\hat{S} = \prod_{i=1}^{8} \hat{s}_i$ as the total spin operator of the Mn_{12} molecule, ψ_i and E_i as the eigenvectors and eigenvalues of the numerically solved 8-spin Hamiltonian of equation 4.5, and $\hat{\sigma}$ as the spin vector operator of the tunneling electron. This equation allows calculating the rate of transitions from the combined initial state $|\psi_i, \sigma_i\rangle$ of the Mn_{12} molecule and the tunneling electron to its final state $\langle \psi_f, \sigma_f |$. The total spin of the system is conserved equivalent to the selection rule $\Delta M = 0, \pm 1$ for the z-component M of the Mn_{12} molecule. The described interaction between the localized spin and the tunnel electrons is similar to previous works [56, 60, 97, 98].

The knowledge of the transition matrix Y from equation 4.6 allows us to simulate a spectrum and compare it with STS data using the general tunneling equation (cf. section 2.1.3) and include temperature broadening to gain

$$\frac{\mathrm{d}I}{\mathrm{d}V}(V) \propto \int_{-\infty}^{+\infty} \sum_{i,f} |Y_{i,f}|^2 \; f\left(\frac{E_i}{k_B T}\right) \left[1 - f\left(\frac{E_f}{k_B T}\right)\right] \; \mathrm{sech}^2\left(\frac{E_f - E_i + eV + \epsilon}{k_B T}\right) \mathrm{d}\epsilon, \tag{4.7}$$

with $f(\epsilon)$ as the Fermi-Dirac distribution and T as the temperature of the system. The use of the Fermi distribution ensures that for low temperatures only excitations from the ground state are taken into account. The result for a temperature of $T = 1.5$ K and the parameters of table 4.1 are shown in figure 4.13.

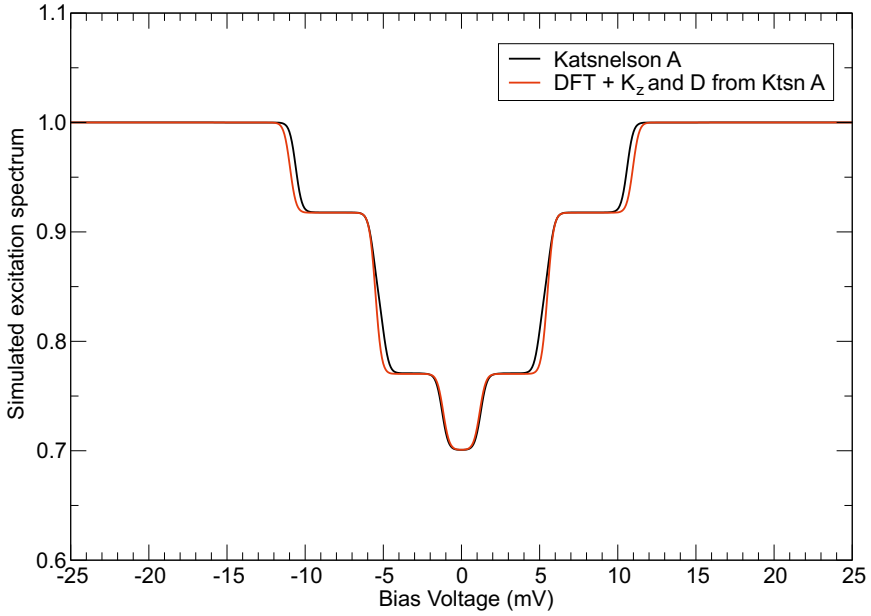

Figure 4.13.: Calculated excitation spectrum using the 8-spin model and the parameters from table 4.1 for $T = 1.5$ K and no magnetic field.

4.4.6. Discussion

The simulated spectra of the spin-flip excitations show three low-energy features at 0 T (10 T) of 1.2 (1.8), 5.5 (6.2), and 10.9 (11.6) meV as displayed in figure 4.9e. Similar energies have been found previously also in neutron scattering experiments on bulk Mn_{12} samples [95, 99] and in break-junction experiments [74]. Comparing the theoretical results with the experimental data presented in figure 4.9d reveals good agreement with

the observation of 3 peaks but differences in the positions especially at the energetically higher peaks, which is not surprising due to the simplifications of the model in which different adsorption geometries are not taken into account.

The simulation confirms, that the lowest excitation in the experimental data, which can be found at 1.4 meV (1.7 meV at 10 T), corresponds to a change of the M quantum number by one. The excitations observed at higher energy are due to an additional change of the total spin S of the molecule. For the latter several spin-configurations are possible and are the origin of the two energetically higher excitations observed at $4-9$ meV and $11-16$ meV, respectively. These excitations spread over relatively large range for different molecules presumably due to conformational changes that affect the fragile ligand field of Mn_{12} when adsorbed in different geometries on the surface. This variation in energy prevents the expected observation of the Zeeman shift for the excitations at higher energies.

At high tunneling rates, in which the average time between two tunneling events is shorter than the lifetime of the excited state, one expects the pumping into states with higher energy [24]. The lifetime of the excited states can be estimated by the linewidth of the peaks in $\mathrm{d}^2I/\mathrm{d}V^2$ to be $2-4$ ps. Thus, spin pumping would require tunneling currents of the order of 100 nA, which is too high for the fragile ligands of the molecule.

To analyze if the Coulomb blockade effect can be responsible for the step-like structure in the $\mathrm{d}I/\mathrm{d}V$ signal, we model our system as two tunnel junctions coupled in series: One junction between the substrate and the molecule (SM) and one between the molecule and the tip (MT). Coulomb blockade steps would occur at integer multiples of the energy $e^2/2C$ with C as the effective capacity of the molecule, which can be calculated by combining both junctions [100]. We estimate the capacities of the two junctions from geometrical considerations to $C_{SM} \approx 6 \times 10^{-19}$ F and $C_{MT} \approx 1 \times 10^{-19}$ F [101]. In our linear setup the effective capacity can be approximated by the lower capacity resulting in energies of $E_C \approx E_C^{MT} \approx 1$ eV, much larger than our observed spectral features.

Furthermore, the observed excitations are not due to vibrational modes of the molecule which are expected at higher energies and have been found by IR- and Raman-spectroscopy on Mn_{12} at energies > 25 meV [102, 103].

In summary, we demonstrated the controlled deposition of fragile Mn_{12} molecular magnets on metallic and thin-insulating surfaces and the feasibility of preserving the quantum magnetism of Mn_{12} on thin insulating layers such as BN.

ES-IBD and local probe techniques such as STM are ideally suited for the preparation of complex molecular nanostructures and studying their properties. The added value provided by the combination of the two techniques is that the local electronic and magnetic properties derived from STM and STS investigations can be linked directly to a chemical structure, well characterized from the fully controlled, gentle deposition process that can be applied even to fragile molecules such as Mn_{12}.

This work provides access to atomic-scale studies of individual molecular magnets and their intriguing behaviour, opening the pathway to experimentally address characteristics like tunneling of magnetization, lifetime of magnetization, or intermolecular coupling of magnetic moments.

4.5. STM Studies on Individual Cr_7Ni Molecules

4.5.1. Cr_7Ni in the Literature

Another class of molecular magnets are antiferromagnetic rings. In such systems the magnetic core consists of a ring of metal atoms (typically 8 to 12) bridged together by carboxylate or flouride groups, which give rise to an antiferromagnetic (AFM) coupling. Typical examples are iron rings of even numbers (Fe_{10}, Fe_{12}, etc) [104–106] or heterometallic molecules derived from the Cr_8 ring like Cr_7Ni [107].

For the investigated Cr_7Ni the parent molecule is Cr_8: a molecular ring of eight Cr^{3+} atoms, where antiferromagnetic coupling of the $s = 3/2$ single spins forms a $S = 0$ singlet ground state [108]. To obtain a molecule with non-zero magnetic moment one Cr ion is replaced by an ion with a different magnetic moment preventing the pairwise compensation through the AFM coupling. In the case of Cr_7Ni one Cr^{3+} ion is replaced by Ni^{2+} with a spin of $s = 1$, resulting in a total spin of $S = 1/2$ (see fig. 4.14).

Among the numerous molecules based on Cr_8 (Cr_7M with M = Co, Fe, Mn, Cd, etc) Cr_7Ni has attracted the most attention, since its two spin-1/2 states ($|1/2, +1/2\rangle$ and $|1/2, -1/2\rangle$) represent a stable two-level system with very little mixing into higher states [109] and long decoherence times [52]. Consequently, Cr_7Ni has been proposed as candidate for qubit implementation [109] and recently the entanglement of several Cr_7Ni molecules has been achieved [110, 111].

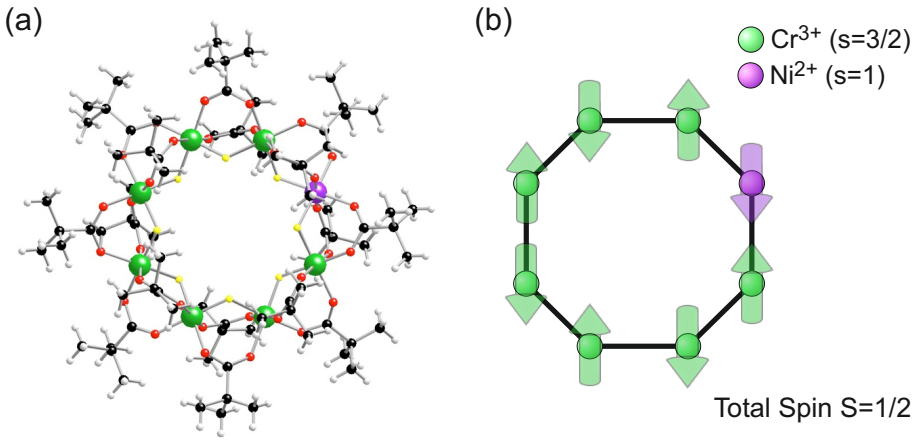

Figure 4.14.: (a) Molecular structure of Cr_7Ni. Colors: C black; H white; O red; F yellow; Cr green; Ni purple. (b) All atomic spins are bound antiferromagnetically resulting in a total spin of $S = 1/2$. Image adapted from work by Alberto Ghirri, with permission.

4.5.2. Motivation

The energy scheme of Cr_7Ni is shown in figure 4.15. Because Cr_7Ni is a spin-$1/2$ system, the only allowed excitation at zero magnetic field is $|S, m\rangle = |1/2, -1/2\rangle \rightarrow |3/2, -3/2\rangle$ changing the total spin S of the system. Excitations only in m are not possible, since the only available states are $m = +1/2$ and $m = -1/2$, which are degenerate without magnetic field. The Zeeman splitting of these two states accounts for 0.1 meV/T and thus requires magnetic fields of at least 5 T to be observable with our available resolution (at 1.5 K).

An (avoided) level crossing occurs at $B = 11$ T, where the $|1/2, -1/2\rangle$ and the $|3/2, -3/2\rangle$ state are degenerate. This allows spontaneous transitions between the states, which could potentially lead to a new type of Kondo effect, where continuous spin transitions are taking place between $m = -1/2$ and $m = -3/2$ resulting in a non-zero average spin. In the regular Kondo effect transitions between $m = +1/2$ and $m = -1/2$ result in a non-magnetic state.

The energy scheme of Cr_7Ni (fig 4.15) is known from calculations and bulk measurements [109, 112], but measurements on individual molecules are missing so far. Analog to the study on Mn_{12} presented before, the first goal of this study is to measure spin-flip excitations on an individual Cr_7Ni molecule verifying its intactness after deposition on a surface. Secondly, we are interested if any particular spectral signature appears at the level crossing indicating an unusual Kondo effect.

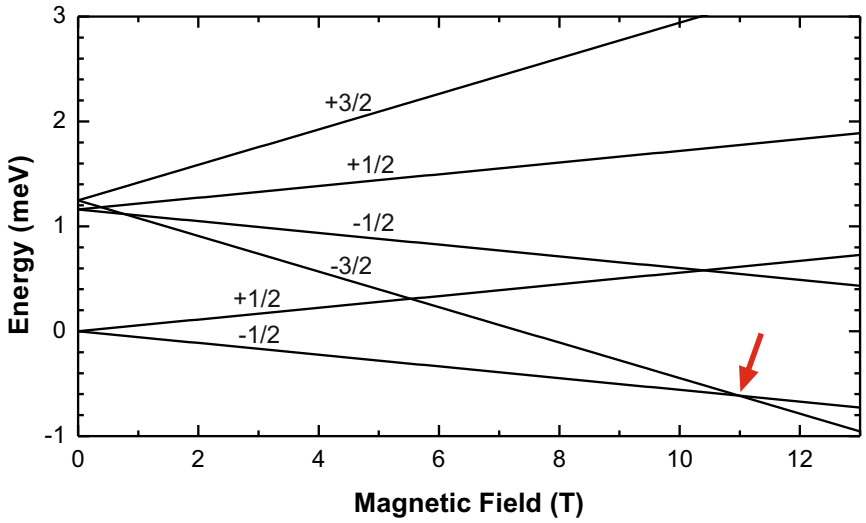

Figure 4.15.: Simplified energy levels of the Cr_7Ni molecule as function of a magnetic field applied along the z-axis. Numbers indicate the quantum number m. At zero field the ground-state doublet is energetically separated from the excited states. At a magnetic field of 11 T a level crossing with the ground state occurs (red arrow). Adapted from [109].

4.5.3. Experimental Results

We applied a similar strategy to investigate individual Cr_7Ni molecules as in the case of the Mn_{12} molecules described in section 4.4. Fortunately, Cr_7Ni rings are less fragile than Mn_{12} molecules and the deposition can be done by thermal evaporation directly in the UHV chamber of the STM setup. X-ray studies have shown that the deposition on Au surfaces does not affect the oxidation state or the local symmetry of the Cr and Ni sites, indicating intact magnetic behaviour [113–115].

We used $\{[(CH_3)_2CHCH_2]_2\text{-}NH_2\}\{Cr_7NiF_8[O_2CC(CH_3)_3]_{16}\}$ (shortly Cr_7Ni-bu) a derivative of Cr_7Ni in which a diisobutylamine is placed in the central cavity of the Cr_7Ni ring. This molecule has been deposited on Au(111) surfaces before in a combined STM/XMCD study [115] and has been supplied by Grigore Timco from the University of Manchester. Further assistance in the setup of this experiment has been provided by Alberto Ghirri from the University of Modena.

We deposited Cr_7Ni-bu on Au(111) and BN/Rh(111) samples by evaporation for $1-10$ min from a crystal powder heated to 200°C. Metal samples are prepared by repeated Ar^+ sputtering and thermal annealing. The BN/Rh samples are prepared as described in appendix A. During deposition the sample temperature was either at room

temperature or cooled down to temperatures between 90 K and 150 K. After deposition the samples were immediately transferred to the STM head at 4.2 K.

Figure 4.16 shows Cr_7Ni deposited on Au(111). The molecules are individually addressable and preferably adsorb at the elbow sites of the Au surface reconstruction. No formation of clusters was observed even for depositions at room temperature. The molecules are circular in shape and have an average diameter of 1.5 ± 0.1 nm and an apparent height of 0.21 ± 0.02 nm, which slightly differs from the 1.9 ± 0.2 nm x 0.20 ± 0.05 nm reported in another STM study [115] possibly due to tip effects (in either study).

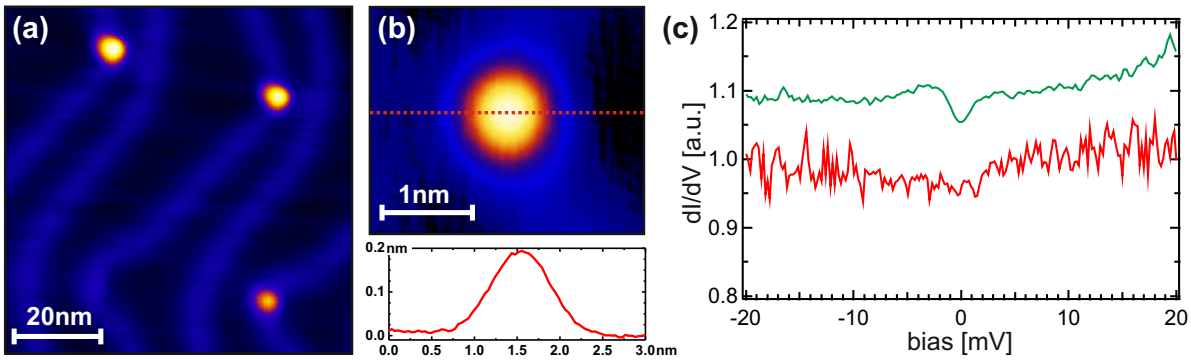

Figure 4.16.: (a) STM image showing several Cr_7Ni adsorbed on the elbow sites of the Au(111) surface reconstruction. (b) Close-up image and height profile of a single Cr_7Ni. The dotted line marks the position of the line profile. (c) dI/dV-spectrum measured at Cr_7Ni molecules are usually flat (red line). Scarcely a dip could be observed, but of unreproducible width ($2 - 15$ mV) and intensity (green line). The spectra are normalized and offset for clarity. Image parameters: **a**: $V = +500$ mV, $I = 20$ pA **b**: -50 mV, 200 pA.

We used STS to investigate the molecules deposited on Au with and without an applied magnetic field of up to 10 T and at a temperature of 1.5 K. Most molecules showed no spectral features in the observed range around the Fermi energy, and while scarcely a spectral dip in the expected energy range could be measured, it was not reproducible on other molecules (fig 4.16c). In total more than one hundred molecules have been investigated in several deposition cycles without the required reproducibility necessary to determine any non-zero observations in the dI/dV-measurements.

In STS the signal-to-noise ratio varies with the bias within a single spectrum. Typical spectra of Cr_7Ni have been taken in a range of ± 20 mV and show an average noise level of 5% of the signal intensity with smaller noise levels towards lower absolute bias values, where spin excitation features would be expected. Thus, if spectral signatures

of the magnetic interactions in Cr_7Ni exist, they should have an amplitude of less than 5% of the total conductance. Furthermore, thermal broadening of the excitation steps reduces the effective amplitude of a spin-flip "dip" if they are not sufficiently separated by their excitation energy. At 1.5 K the amplitude of an excitation at ± 0.2 meV would be reduced to 50% by this effect.

To reduce possible influences of the substrate like charge transfer, we deposited Cr_7Ni on a decoupling layer of BN on Rh(111). Imaging of Cr_7Ni deposited on BN/Rh surfaces showed no localized molecules, but instead were characterized by unstable tunneling conditions resulting in streaks in the STM images, following the movement of the tip on the surface (fig 4.17). This behaviour is typical for adsorbates which are mobile enough to be dragged across the surface by the tip or even get attached to it in an uncontrollable manner. The unstable behaviour prevails even with tunnel currents as low as 5 pA and for bias voltages in the range of $\pm(10 - 1000)$ mV. This inability to stably image Cr_7Ni on BN/Rh for dozens of tip geometries and multiple depositions cycles for over 40 measurement days, leads us to conclude that Cr_7Ni is not sufficiently immobilized on BN/Rh even at 1.5 K to allow STM imaging.

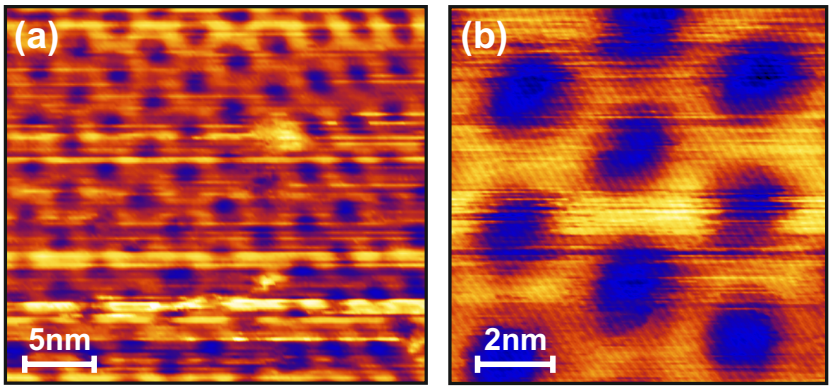

Figure 4.17.: (a,b) STM images of Cr_7Ni on BN/Rh showing horizontal streaks due to mobile adsorbates on the surfaces being dragged along by the tip. Image parameters: **a**: $V = -100$ mV, $I = 12$ pA **b**: -100 mV, 10 pA.

In summary we have imaged Cr_7Ni on Au(111) surfaces for the first time at low temperatures and with unprecedented image quality. Spectroscopy of the molecules has shown no signature of spin-flip excitations, indicating that either the magnetic arrangement of the individual spins has been changed upon adsorption or that the signal intensity is to low to be measured with our setup. Stable imaging of Cr_7Ni deposited on BN/Rh has been hindered by a too high mobility of the molecules during scanning. Besides different adsorption/hopping energies for Cr_7Ni on BN/Rh, this instability can

be caused by the insulating character of the BN, which enforces a shorter tip-sample distance at the same tunneling parameters making a crash into the molecule more likely.

In both cases a more stable system setup as provided in the new lab building could bypass this restrictions by allowing lower tunneling currents or by providing a lower noise level for spectroscopy.

5. Weak Coupling Kondo Effect in a Purely Organic Radical

5.1. The Kondo Effect

5.1.1. Introduction

Electrical resistivity in metals is dominated by electron-phonon scattering at room temperature. When lowering the temperature, the phonons freeze out, leading to a monotonous decline of the resistance towards an intrinsic resistivity based on impurities and defects in the metal. Unaware of the nature of their observation, first experimental evidence for the Kondo effect was already presented in the 1930s [12], where measurements on different metals at low temperatures showed a resistance minimum at a finite temperature (see figure 5.1). It took 30 years until this could be attributed to the scattering on magnetic impurities buried in the metals [13, 116].

The first quantitative explanation was given by Kondo [13], who modeled the interaction of magnetic impurities with the conduction electrons using perturbation theory. Since his perturbation series breaks down below a critical ratio of interaction strength to temperature, later called the Kondo temperature T_K, his model's validity is limited to temperatures higher than T_K, the region of weak coupling (more in section 5.1.2).

The missing description of the phenomena in the strong coupling regime or in the cross-over region (temperatures below or around T_K) was called the *Kondo Problem*. Based on the preliminary work by Anderson [117], Wilson [118] solved this problem for a single spin-$^1/_2$ impurity by using a renormalization group transformation (RG). He showed that for $T = 0\,\mathrm{K}$ and an antiferromagnetic interaction between the impurity and the conduction band the impurity spin is completely screened by the conduction electrons resulting in a non-magnetic singlet-state.

Even before magnetic impurities were revealed as cause for the Kondo effect, Anderson described under which conditions a single magnetic impurity embedded in a metal could retain its magnetic moment [119]. Schrieffer and Wolff showed later that his results were transferable to the general Kondo problem [120].

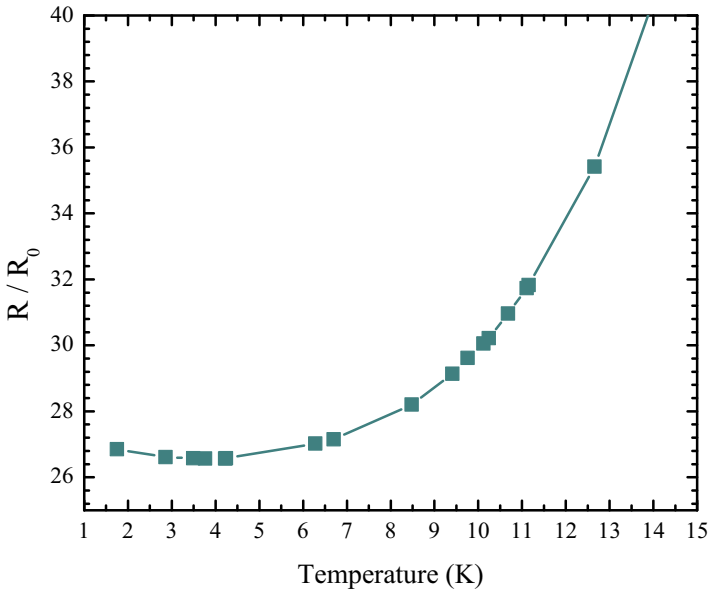

Figure 5.1.: Resistance curve of a Au wire at low temperatures, showing a minimum at 3.7 K. Resistance is given relative to a base value R_0. Data from [12].

With access to the atomic scale, made possible by the experimental development of the last decades, interest in the Kondo effect has renewed and the effect has been observed in several nano-scale systems: Quantum dots provided the first observation of the Kondo effect in a localized state rather than a statistical distribution [15], and their wide tunability has led to novel types of the Kondo effect [121, 122]. Naturally, the Kondo effect is not limited to point-like structures but has also been found in 1-dimensional structures such as nanotubes [123].

STM studies of magnetic adatoms on metallic substrates were the first to observe the Kondo resonance at the Fermi level for a single atom [14,124]. The Kondo effect has been investigated on single transition metal atoms (most commonly Co atoms) on different metallic surfaces [14, 125, 126] or on thin insulating layers [127]. Further work focused on the line shape of the resonance [128], and its dependance on temperature [129] or magnetic field [127]. The real-space imaging and manipulation capabilities of the STM led to a more detailed understanding of the role of the local environment [127] or the interaction between two Kondo impurities [130, 131].

The Kondo effect has also been observed for single metal atoms embedded in molecules, which offers a higher degree of tunability of the coupling to the substrate. With metal atoms like Mn, Fe or Co embedded in phthalocyanines [132–134] or porphyrins [135, 136] very high Kondo temperatures up to 550 K [137] have been observed, a measure of strong spin-electron coupling J. STM manipulation allows the controlled switching of

the Kondo effect on existing molecules [132, 135] and even the manual bottom-up building of molecular structures showing the Kondo effect [138, 139]. More recently, Kondo resonances have been studied on purely organic molecules, which obtain a magnetic moment upon adsorption through charge transfer processes [140–142].

5.1.2. Kondo's Perturbation Approach

The first analytical description of this scattering process was given by Kondo [13], who used a perturbation approach, in which the conduction electrons (in the metal) are perturbed by an exchange interaction J with the electrons in the impurity. The Kondo Hamiltonian can be written as

$$H = \underbrace{\sum_{k,s} \epsilon_k a^*_{ks} a_{ks}}_{\text{conduction electrons}} \underbrace{- J \sum_{k,k'} (a^*_{k'\uparrow} a_{k\uparrow} - a^*_{k'\downarrow} a_{k\downarrow}) S_z}_{\text{spin-conserving scattering}} \underbrace{- J \sum_{k,k'} a^*_{k'\uparrow} a_{k\downarrow} S^- + a^*_{k'\downarrow} a_{k\uparrow} S^+}_{\text{spin-flip scattering}} . \quad (5.1)$$

In this Hamiltonian the conduction electrons have a wave vector k, a spin s which can either point up ($\uparrow$) or down ($\downarrow$), and an energy ϵ_k. They are created or annihilated by the corresponding operators a^* and a. The impurity has the spin-operator S, with the z-component S_z and $S^\pm = S_x \pm i S_y$.

Based on this Hamiltonian and the general transport properties of metals the conductivity can be calculated to be

$$\rho = \rho_0 + a T^5 + J \log(T), \quad (5.2)$$

where for high temperatures the phonon scattering dominates with T^5 and for low temperatures the impurity scattering with $\log(T)$. This can explain the resistance minimum assuming $J < 0$, implying an anitferromagnetic spin alignment of the conduction electrons and the localized electrons. While this theory could fit the existing data at that time, the model breaks down for $T \to 0\,\mathrm{K}$ and leads to a $\log(T)$-singularity in the conductivity. Thus, the theory is only valid for temperatures above a characteristic temperature, which was later called the Kondo temperature T_K.[1] To be more precise, as an perturbative approach in J, this calculation only holds below a characteristic ratio of interaction strength to temperature, the weak-coupling regime (see figure 5.2).

[1] Note that in the literature different definitions of T_K are used, which usually are in the same range, but based on different approaches to the Kondo problem.

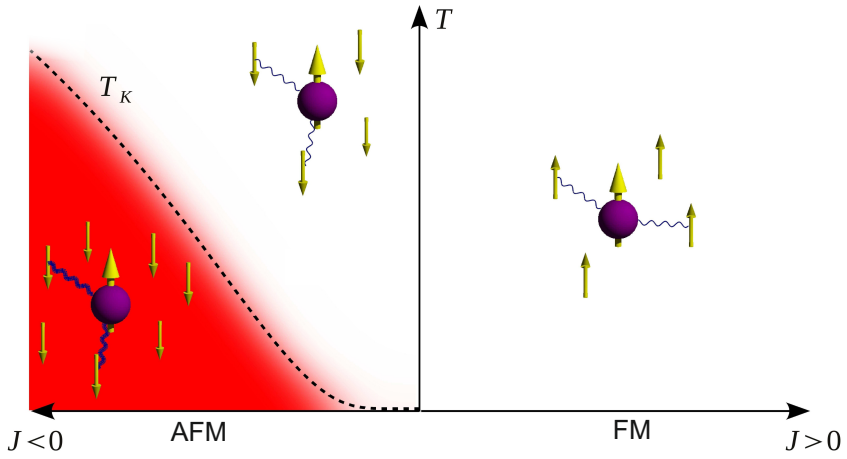

Figure 5.2.: The exchange interaction J couples conduction electrons (small arrows) with the localized spin of the impurity (ball and large arrow). For antiferromagnetic (AFM) coupling ($J < 0$) and at low enough temperatures this results in a many body state where the spins of the conduction electrons effectively screen the impurity spin (strong coupling regime, red area). In contrast, at temperatures above a characteristic temperature (Kondo temperature T_K, dashed line) or at ferromagnetic (FM) coupling ($J > 0$) the spin remains and can be described by perturbation theory (weak coupling regime).

5.1.3. The Anderson Model

Anderson [119] described under which conditions a single magnetic impurity embedded in metal can retain its magnetic moment – a prerequisite for a Kondo state. In his model the electronic structure of the impurity is simplified to a single d-orbital[2], which can contain up to two electrons, interacting with the conduction band of the metal with a constant density of states σ. Since only an unpaired spin constitutes a magnetic moment, the d-orbital must be singly occupied (d^1) and thus lies below the Fermi energy with a binding energy ϵ. Adding a second electron to the orbital increases the energy by the Coulomb repulsion U. The doubly occupied orbital d^2 must lie above the Fermi energy to ensure the unpaired spin. The localized d-orbitals hybridize with the conduction band and are therefore broadened by $\Delta = |V|^2\sigma$, with V as matrix element describing the intensity of the s-d-interaction.

As can be seen in figure 5.3, this gives certain restrictions on the relative energies of U, ϵ, and Δ for the existence of a magnetic state. Essentially it means, that the d^1-state should be well below and the d^2-state well above the Fermi energy.

[2]This can be generalized to be also valid for f-orbitals.

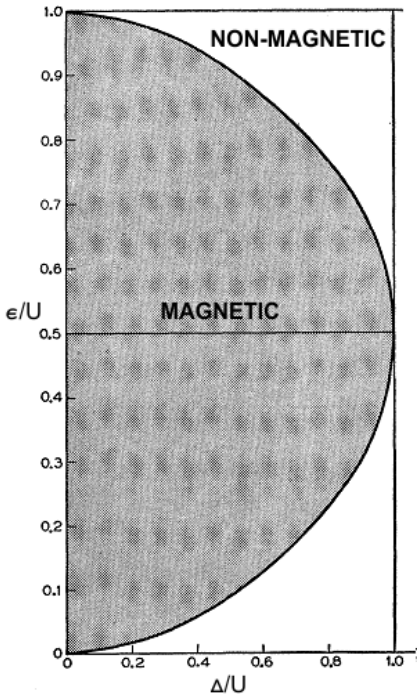

Figure 5.3.: Regions of magnetic and non-magnetic behaviour for a magnetic impurity embedded in a non-magnetic metal. The horizontal axis Δ/U describes the width of the localized states versus the repulsion energy, with smaller hybridization leading more likely to a magnetic state. The vertical axis ϵ/U describes the position of the d-states with respect to the Fermi level; at $\epsilon/U = 0.5$ they are symmetrically around the Fermi level, a perfect condition for magnetic states. Image from [119].

Later it has been shown, that Anderson's formalism can be related to the Kondo problem [120]. In the limit of small *s-d* hybridization Δ the magnetic impurity picture of Anderson is equivalent to the scattering process described by Kondo. The exchange interaction J of the Kondo model can be expressed as

$$J = \frac{\Delta}{\pi\rho} \frac{U}{\epsilon(\epsilon + U)}. \tag{5.3}$$

While Anderson described the energy scheme of a static magnetic impurity hybridized with the conduction band, the Kondo effect depicts a dynamic state, consisting of multiple conduction electrons continuously interacting with the impurity state through spin-flip processes. Nevertheless the Anderson model offers a descriptive understanding of the emergence of a resonance at the Fermi energy based on spin-flip processes:

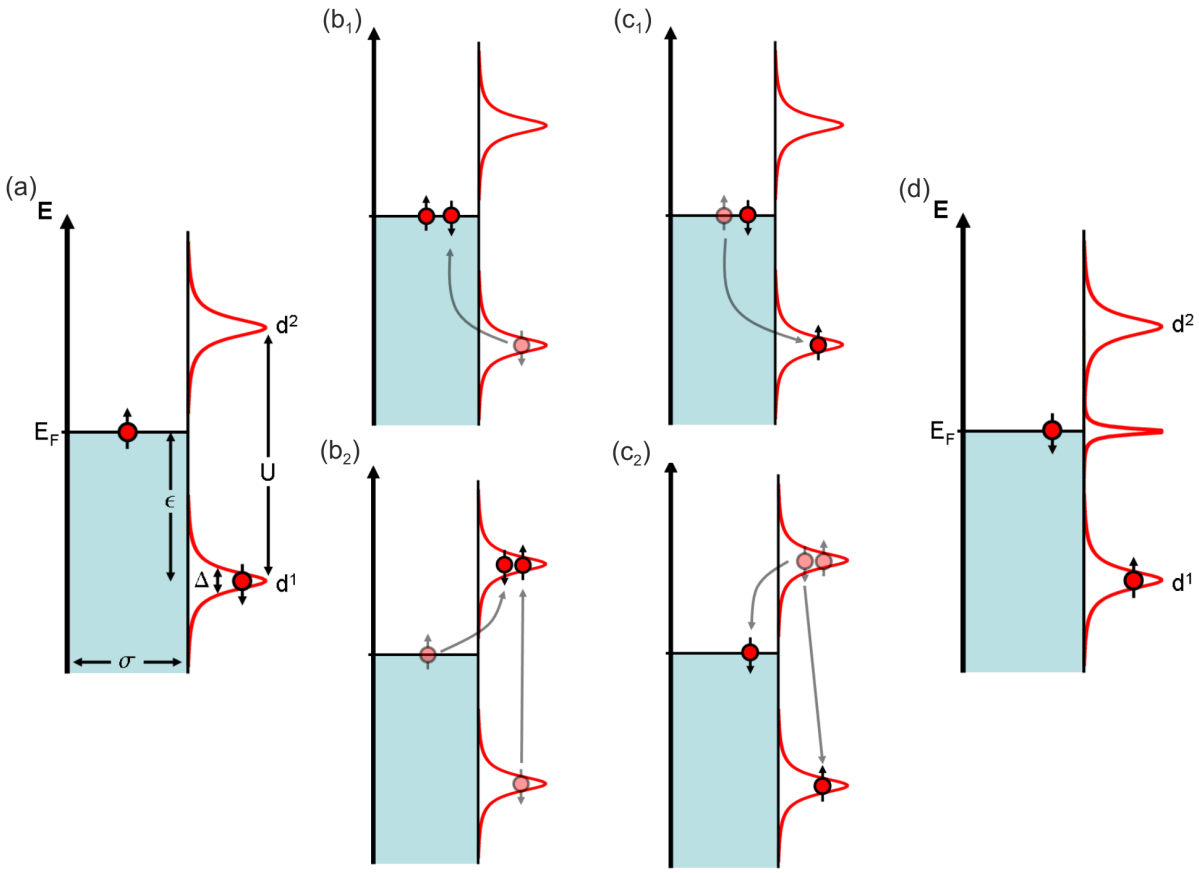

Figure 5.4.: Spin-flip process in the Anderson model. In order to flip the impurity spin from down (a) to up (d), a virtual process over either an empty orbital (b_1,c_1) or a doubly filled orbital (b_2,c_2) is necessary. The involved electrons at the Fermi energy generate the Kondo resonance (d). Note that the orbitals d^1 and d^2 do not have to be symmetrically around E_F.

To flip the spin in a singly occupied *d*-state, a bulk electron of the opposite spin is needed (figure 5.4a). To exchange the positions of both electrons, either the orbital is first emptied and then occupied with the opposite spin (fig. 5.4b_1,c_1), or it is first doubly occupied and then the initial electron is removed (fig. 5.4b_2,c_2). To bring the electron from the *d*-orbital to an empty state in the bulk (above the Fermi energy), *at least* the energy ϵ is needed (fig. 5.4b_1), while the refilling of the orbital with an electron of opposite spin (from below the Fermi energy) gains *at most* the energy ϵ (fig. 5.4c_1). The same argument holds for the case of the temporarily doubly occupied orbital, where an initial energy of at least $2U - \epsilon$ is required (fig. 5.4b_2). Since in the continuous spin-flip process of the Kondo effect no external energy is available, the bulk electrons involved in this process must be located exactly at the Fermi energy.

This process is forming a many-particle state, which can be depicted as the continuous flipping of the impurity spin. Going beyond the single-particle picture, a multitude of conduction electrons are involved, with their total spin screening the impurity spin, resulting in a non-magnetic singlet state. Since this electrons are located at the Fermi energy, the so called Kondo resonance emerges at the Fermi energy (fig. 5.4d), which is the basic object of investigation for STM studies of the Kondo effect.

5.1.4. The Appelbaum Model

Shortly after Kondo described the resistance increase at low temperatures due to spin-flip scattering, more detailed transport measurements have been published. Measurements on tunnel junctions incorporating magnetic impurities (deliberately or not) showed a zero bias anomaly in the electrical conductance, strongly varying with temperature and magnetic field [143, 144]. Joel Appelbaum (together with Anderson) presented a theory, which completely described the conductance G of such a tunnel junction as function of bias, temperature, and magnetic field $G(V, T, H)$ [145–147].

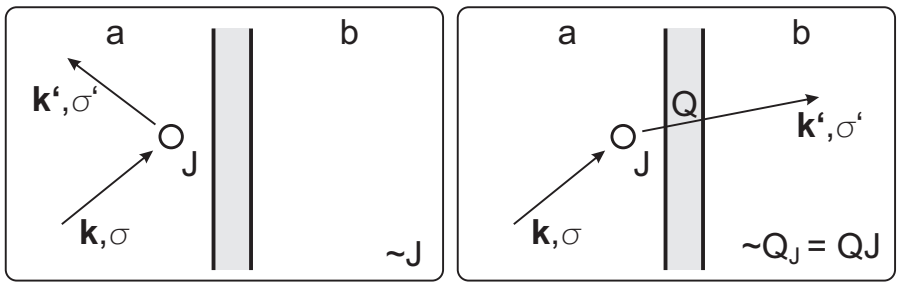

Figure 5.5.: The Appelbaum model: A tunnel gap separates the electrodes a and b, with the impurity (circle) on the a-side. An electron with wavevector $\mathbf{k}$ and spin σ moves towards the impurity and is scattered with the probability J. With the tunnel probability Q, the total probability for an electron to scatter at the impurity and tunnel across the gap is $Q_J = QJ$.

He assumed a tunnel junction, consisting of two metals (a and b) separated by an oxide layer. A localized magnetic state of Spin S exists on the side of the metal a close to the junction (see figure 5.5). It is coupled to the conduction electrons on both sides of the junction with the coupling constant J (to side a) or Q_J (to side b), respectively, with a negative J implying antiferromagnetic coupling between conduction electrons and the

localized spins. These couplings have to be added to the Hamiltonian H_0 leading to a total $H = H_0 + H'$, with the contribution of the localized state H' of the following form[3]:

$$
\begin{aligned}
H' &= H^{ab} + H^a && (5.4)\\
H^{ab} &= -Q_J \sum_{k,k'} \Big(S_z(a^*_{k\uparrow} b_{k'\uparrow} + b^*_{k\uparrow} a_{k'\uparrow} - a^*_{k\downarrow} b_{k'\downarrow} - b^*_{k\downarrow} a_{k'\downarrow}) && (5.5)\\
&+ S^+(a^*_{k\downarrow} b_{k'\uparrow} + b^*_{k\downarrow} a_{k'\uparrow}) + S^-(a^*_{k\uparrow} b_{k'\downarrow} + b^*_{k\uparrow} a_{k'\downarrow}) \Big) \\
H^a &= -J \sum_{k,k'} \left(S_z(a^*_{k\uparrow} a_{k'\uparrow} - a^*_{k\downarrow} a_{k'\downarrow}) + S^+ a^*_{k\downarrow} a_{k'\uparrow} + S^- a^*_{k\uparrow} a_{k'\downarrow} \right) && (5.6)
\end{aligned}
$$

Here H^{ab} denotes the Hamiltonian for electrons scattered at the impurity, and then cross the junction from a to b (or vice versa), while H^a describes the processes, where an electron from side a is scattered at the impurity but does not cross the gap (see fig. 5.5). Both parts contain terms, where either the impurity spin and the electron spin stay constant (terms with S_z), or where both spins change (terms with $S^\pm$). Either way the total spin of the system is preserved. H^a is essentially the Kondo Hamiltonian as described in equation 5.1. Appelbaum extended the Kondo model by adding a tunnel junction and scattering processes across it. Thus, when applying the Appelbaum model to an STM setup, the observation by the STM tip is already part of the model and needs no further implementation. A term H^b describing the interaction of tip electrons with the impurity across the junction (without crossing it) is omitted by Appelbaum as usual in STS.

For simplicity we assume that Q_J can be factorized into J, the coupling between the impurity spin and an electron on side a, and Q, the coupling between both electrons across the tunnel gap, so that $Q_J = Q \cdot J$ (see fig. 5.5). In the STM experiments later shown in this work the sample resembles electrode a containing the impurity, while Q describes the tip-sample interaction.

The current I across the junction can be calculated using the general tunneling equation (eq. 2.4), which arises the main task of calculating the transition probabilities $W_{k\sigma,k'\sigma'}$. Here (k, σ) describes a combined state of a conduction electron and the impurity spin. For simplicity such a state will be named shortly i (or j) with the corresponding Energy E_i (E_j) and the transition probability W_{ij}. Since the spin flip operators S^+ and S^- do not commute, the transition probability between two states depends on the direction of the transition ($W_{ij} \neq W_{ji}$), and thus the general tunneling equation has to be used in the form

[3]The operators follow the naming conventions of the 2nd quantization as used before in equation 5.1.

$$I = e \sum_{i,j} \Big(W_{ij}\ f(\epsilon_i, T)[1 - f(\epsilon_j, T)] - W_{ji}\ f(\epsilon_j, T)[1 - f(\epsilon_i, T)] \Big), \tag{5.7}$$

where $f(\epsilon, T)$ is the Fermi distribution function.

To calculate W_{ij} from the Hamiltonian H, Appelbaum uses a perturbation approach: He assumes that the scattering related tunneling H' is small against H_0 and accordingly uses perturbation theory to calculate W_{ij}, which at third order in H' reproduces the experimentally observed behaviour. Thus, the transition probabilities can be described as

$$W_{ij} = \frac{2\pi}{\hbar} \Bigg[\underbrace{|H'_{ij}|^2}_{\text{2nd order}} + \underbrace{\sum_{k \neq i} \Big(\frac{H'_{ik} H'_{kj} H'_{ij}}{E_i - E_j} + \text{compl. conj.} \Big)}_{\text{3rd order}} + \underbrace{\dots}_{\substack{\text{higher} \\ \text{orders}}} \Bigg] \delta(E_i - E_j). \tag{5.8}$$

For a complete description of the system the influence of an applied bias V and a magnetic field H have to be taken into account. The bias voltage is applied to the electrode a and shifts the energies of all states on this side by eV. The magnetic field leads to a Zeeman splitting of $\Delta = g\mu_B H$ for the eigenstates of the localized spin. Here g is the gyromagnetic factor of the localized spin and μ_B is the Bohr magneton. The Zeeman shift of the conduction electrons in tip and sample have no effect on the current, because we assume the DOS of tip and sample to be constant in the energy range of interest.

The current I can now be obtained by carrying out the sums in equation 5.7, which include the thermal broadening of the Fermi levels. We are in fact not interested in the current I, but in the conductance $G = \partial I / \partial V$. Before taking the derivative, we replace the sums in equation 5.7 with integrals over the energy, to introduce the density of states (DOS) of both electrodes $\rho^a(\epsilon)$ and $\rho^b(\epsilon)$. Since the Fermi functions in equation 5.7 restrict all integrals to values close to the Fermi energy ϵ_F, we will assume both DOS to be constant as $\rho^{(n)}(\epsilon) = \rho^{(n)}(\epsilon_F)$, or more shortly $\rho^{(n)}$ for $n = a, b$. After carrying out the integrals and taking the derivative towards V, we finally gain $G(V, T, H)$.

In the following we will first discuss the contributions of the 2nd and the 3rd order perturbation terms to the current and conductivity and then add them up to obtain the total conductance:

The second order terms in equation 5.8 are a constant with a delta function such as $\delta(\epsilon_i + eV - \epsilon_k \pm \Delta)$ limiting the possible transitions. This leads to a constant conduc-

tance at zero magnetic field and to inelastic steps symmetrically around zero bias at magnetic fields. Appelbaum approximates these steps as $Z(\Delta \pm eV) = \tanh\left(\frac{\Delta \pm eV}{2k_BT}\right)$ by using a somewhat inconsistent low temperature approximation for only some of the involved Fermi functions. For a more accurate description we will describe these spin flip excitations by the general formula for inelastic excitations (as derived in section 2.2.3) as

$$Z(\Delta \pm eV) = \frac{\exp\left(\frac{\Delta \pm eV}{k_BT}\right)\left(\frac{\Delta \pm eV}{k_BT} - 1\right) + 1}{\left(\exp(\frac{\Delta \pm eV}{k_BT}) - 1\right)^2}. \tag{5.9}$$

The third order terms in equation 5.8 include the transition over an intermediate state k. The summation over this states leads to transition probabilities proportional to

$$g(\omega) = \rho^a(\epsilon_F) \int_{-E_0}^{E_0} \frac{f(\epsilon)}{\epsilon - \omega} \mathrm{d}\epsilon \tag{5.10}$$

with $f(\epsilon)$ as Fermi distribution. This scattering into an intermediate state represents the actual continuous spin flip scattering of the Kondo effect and the same term can consequently be also be found in the original work of Kondo [13]. The integral describes a logarithmic shape convoluted by $f(\epsilon)$ to incorporate the occupation of states also for the intermediate state, which reflects the many particle nature of the effect. Since the scattering occurs at the site of the impurity, the DOS of side a is used. The integration is limited to an energy range of $2E_0$ around the Fermi energy, which represents the range in which conduction electrons interact with the impurity spin. While this cut-off parameter E_0 is experimentally inaccessible, it can be shown that the exact value of E_0 has only minor influence on the conductivity.

The corresponding 3rd order conduction terms contain – besides the step functions at magnetic fields as in the 2nd order terms – a peak at zero bias (and at the energies $\pm\Delta$) of the form

$$F(\omega) = -\int_{-\infty}^{+\infty} g(\epsilon) \frac{\partial}{\partial \epsilon} f(\epsilon - \omega)\ \mathrm{d}\epsilon. \tag{5.11}$$

This peak is the Kondo resonance as it can be observed by STS. In the experimental realization of this model, equation 5.10 represents the actual LDOS of the sample, while equation 5.11 describes how the LDOS is observed including the broadening effect of the tip, with $F(\omega)$ as a convolution of $g(\omega)$ with a Fermi function. At zero temperature $F(\omega)$ is reduced to a logarithmic singularity of infinite sharpness, while the broadening at higher temperatures can be approximated by $F(\omega) = \rho^a(\epsilon_F) \ln\left(\frac{|\omega| + k_BT}{E_0}\right)$.

Adding up the second order $G^{(2)}$ and third order $G^{(3)}$ terms, and using $Q_J = QJ$, the total conductance G can be described by

$$\begin{aligned} G(V) &= c_2 G^{(2)}(V) + c_3 G^{(3)}(V) \qquad (5.12) \\ G^{(2)}(V) &= J^2 Q^2 \left[1 + m_1 \left(Z\left(\Delta + eV\right) + Z\left(\Delta - eV\right)\right)\right] \\ G^{(3)}(V) &= 2J^3 Q^2 \left[1 - m_2 + m_1 \left(Z\left(\Delta + eV\right) + Z\left(\Delta - eV\right)\right)\right] F\left(eV\right) \\ &+ J^3 Q^2 \left[1 + m_2 + 2m_1 Z\left(\Delta - eV\right)\right] F\left(eV - \Delta\right) \\ &+ J^3 Q^2 \left[1 + m_2 + 2m_1 Z\left(\Delta + eV\right)\right] F\left(eV + \Delta\right). \end{aligned}$$

with $c_2 = \frac{4\pi e^2}{\hbar} S(S+1)\rho^a\rho^b$, $c_3 = \rho^a c_2$, $m_1 = \frac{<M>}{2S(S+1)}$, and $m_2 = \frac{<M^2>}{S(S+1)}$. Hereby describes S the total spin of the impurity and $\langle M \rangle$ and $\langle M^2 \rangle$ the statistical average of S_Z and S_Z^2, respectively.

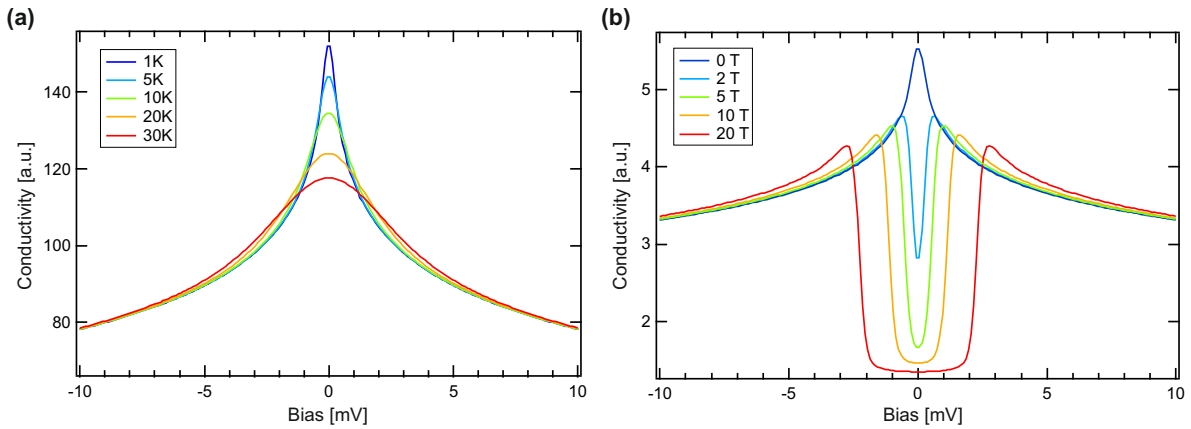

Figure 5.6.: The total conductance G as function of the bias voltage. (a) Plot for different temperatures without magnetic field. (b) Plot for different magnetic fields at 1.5 K. For all cases is $E_0 = 40$ mV and the ratio $Jc_3/c_2 = 0.03$.

Figure 5.6a shows the behaviour of the conductivity without magnetic field. For negative J (antiferromagnetic coupling) the conductivity shows a peak at zero bias, while a positive J (ferromagnetic coupling) would produce a dip. At zero magnetic field equation 5.12 can be simplified to

$$G(V) = c_2 J^2 Q^2 \left(1 + 4J\rho^a(\epsilon_F) F\left(eV\right)\right). \qquad (5.13)$$

With increasing magnetic fields the central peak vanishes and the two outer peaks arise at the position $V = \pm\Delta$, which is exactly on top of the inelastic steps (see fig. 5.6b). The relative height of these peaks compared to the step heights is determined by

the relative amplitudes of the 2nd and 3rd order terms in the conductivity and can be used to deduce the coupling intensity $J\rho^a$.

The coupling constant J describes the coupling between one single conduction electron and the impurity spin and has been used so far as measure of coupling intensity. For a real system many conduction electrons are participating, and thus the quantity $J\rho^a$ is more useful to describe the interaction strength between conduction band and impurity.

As a perturbation approach, the Appelbaum model is only valid, when the perturbation series in equation 5.8 converges. As in the original Kondo model this depends on the ratio of temperature to coupling strength J. For a given coupling J, we can define a Kondo temperature as

$$k_B T_K = E_0 \exp(-J\rho^a) \tag{5.14}$$

The series converges only for temperatures above T_K, which is called the weak-coupling regime. As can be seen from equation 5.14, high Kondo temperatures can only be achieved in the antiferromagnetic case ($J < 0$), while for the ferromagnetic case ($J > 0$) the Kondo temperature can be approximated to be zero (see fig 5.2).

5.1.5. Strong Coupling Model

Most Kondo studies done by STM/STS claim to observe the Kondo resonance at temperatures below the Kondo temperature T_K (in the strong coupling regime) and thus can be described based on renormalization group calculations [118] or Fermi liquid models [148]. In this regime the lineshape of the resonance is often modeled as a Lorentzian $\delta(\epsilon) \propto \frac{\Gamma_L^2}{\Gamma_L^2+\epsilon^2}$, with its half-width at half-maximum (hwhm) Δ directly given by $\Delta = \Gamma_L$. The Kondo temperature can be defined as hwhm at $T = 0$ K by

$$\Delta(0\text{K}) = k_B T_K. \tag{5.15}$$

For finite temperatures the half-width broadens according to the work by Nagaoka and Crommie [129] as

$$\Delta(T) = \frac{1}{2}\sqrt{(\alpha k_B T)^2 + (2k_B T_K)^2} \tag{5.16}$$

with $\alpha = 2\pi$ (see figure 5.7a).

In more recent works [149–151] the Lorentzian was exchanged by the more accurate *Frota function* [152, 153], which has been first used to describe Kondo resonances in

photo emission studies, but has later been also applied to STS studies [128]. The Frota function describes the conductivity δ as

$$\delta(\epsilon) \propto \mathrm{Re}\left[\sqrt{\frac{i\Gamma_F}{\epsilon + i\Gamma_F}}\right] \tag{5.17}$$

with the energy ϵ and the width parameter Γ_F. The Frota function describes particularly the tails of a Kondo resonance more accurately than a Lorentzian (fig 5.7b), and will be used in this work. For easier handling by data analysis software the above equation can be converted to

$$\delta(\epsilon) \propto \sqrt{\frac{\sqrt{\Gamma_F^2 + \epsilon^2} + \Gamma_F^2}{\epsilon^2 + \Gamma_F^2}}. \tag{5.18}$$

The definition of the Kondo temperature by the half-width of the peak and the broadening at higher temperatures as described before (equations 5.15 and 5.16) are still valid also with the Frota function. Since the Frota function uses the width parameter Γ_F, we need to use the relation $\Delta = 2.54\Gamma_F$ [154] to obtain the actual half width Δ, unlike the Lorentzian, where it is directly given by the identity $\Delta = \Gamma_L$.

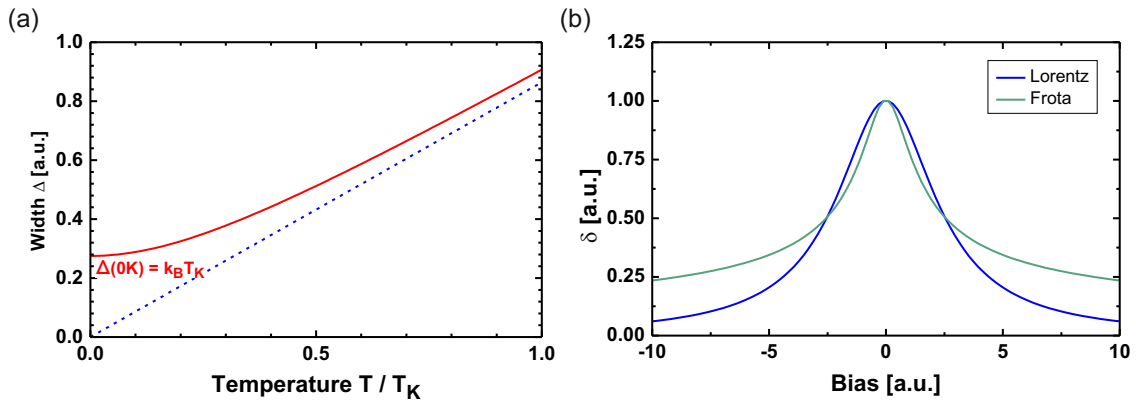

Figure 5.7.: **(a)** Temperature dependance of the peak width (red line). The minimal width at $T = 0$ K defines the Kondo temperature. At higher temperatures the dependance converges to a linear increase of $\Delta = 2\pi k_B T$ (dotted line). Strictly speaking this behaviour is only valid for $T \ll T_K$, but is anyhow often applied to data at temperatures up to the range of T_K in the literature [127,129] **(b)** Lineshape comparison for a Frota and a Lorentzian curve. The width parameters are $\Gamma_L = 2.54\Gamma_F$.

5.1.6. Observation of the Kondo Effect by Scanning Tunneling Spectroscopy (STS)

STM studies of the Kondo effect rely on measuring the Kondo resonance at the Fermi energy by means of scanning tunneling spectroscopy (STS), typically identified by its temperature or magnetic field behavior. While for example photo-emission was able to image both the Kondo resonance and the d- or f-orbital it is based upon [155](figure 5.8), this basic orbital has never been observed by STS yet. While theoretically STS should be able to measure the singly occupied orbital below the Fermi level as well as the empty doubly-occupiable state above it, the small overlap of the d- or f-orbitals with the tip and the general low signal intensity of the orbital compared to the Kondo resonance have prevented observations so far.

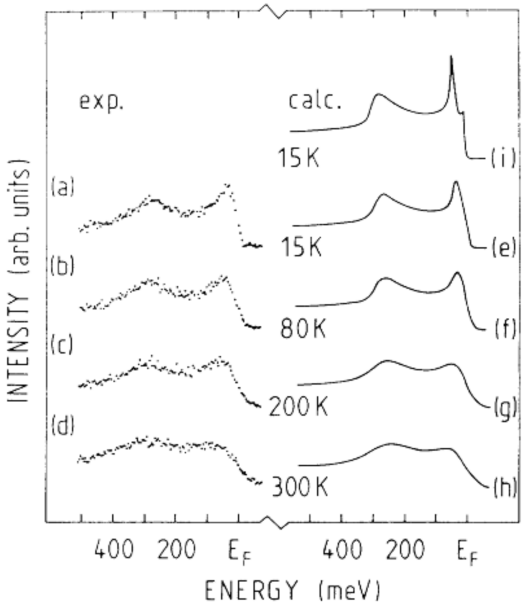

Figure 5.8.: Photo emission data (left) and calculations (right) of a $CeSi_2$-sample for different temperatures. The singly occupied f-orbital can be seen at around 300meV, while at the Fermi energy E_F the Kondo resonance is visible directly next to the signal drop representing the Fermi edge. Naturally photo emission can only address occupied states. From [155].

Another distinctive feature of STS when observing the Kondo effect is that the Kondo peak not necessarily appears as such in the spectra, but rather as a dip or more complex structure. This is due to quantum interference between two tunneling channels, where the electrons either tunnel into the Kondo resonance or directly into the bulk. The resulting energy spectra can been explained as a Fano-resonance [156, 157], which is a general wave phenomenon present in different areas of physics.

It should be noted here that the observation of a Kondo resonance differs from the spin excitations observed via inelastic electron tunneling spectroscopy (IETS) as described in section 2.2.3. While in the case of IETS the tunneling current is necessary to generate the spin flips in the sample, the Kondo effect is happening regardless of the presence of a tunnel current.

5.2. Kondo Studies on a Nitronyl Nitroxide Radical

The following results have been published in *Nature Communications* in 2013 as an article named "Temperature and Magnetic Field Dependence of a Kondo System in the Weak Coupling Regime" [158].

5.2.1. Motivation / Introduction

In this study, we have observed the Kondo resonance of a organic radical with its unpaired electron delocalized over several atoms in its nitronyl nitroxide group. The investigated radical consists of a terphenyl-based backbone connected with the spin-carrying nitronyl nitroxide group. The full structure can be seen in figure 5.9 and is described as a *2-nitronylnitroxide-5'-methyl-[1,1';4',1"]terphenyl-4,4"-dicarbonitrile*, which will be further referenced after its functional group as nitronyl nitroxide or NIT for simplicity.[4]

While radicals naturally tend to be very reactive, and thus loosing their spin quickly, the unpaired spin in the nitronyl nitroxide is spatially delocalized over the O-N-C-N-O part of the side group [159, 160], stabilizing it against chemical reaction and charge transfer. This has led to studies of radical-metal chains, where NIT groups alternate with different metal atoms (Mn, Cu, etc.) showing magnetic behavior [161, 162]. Purely organic molecules with a NIT group have shown to form ferromagnetic molecule crystals below a Curie temperature of 0.6 K [36]. Furthermore, the molecules are stable in ambient conditions and have a shelve life of at least five years.

Most studies of the Kondo effect have been conducted on transition metal atoms or molecules containing transition metals as spin carrier. The spin quantum number S of these systems is defined by the occupation of the d- or f-orbital of the magnetic atom, possibly reduced by the substrate [126]. The resulting S is usually above $1/2$, while theoretical descriptions of the Kondo effect have focused on the $S = 1/2$ system due to its simplicity (e. g. the Anderson model), making quantitative comparisons often cumbersome.

[4] The molecules have been synthesized by Christophe Stroh, department of Prof. Marcel Mayor, Institut für Nanotechnologie, Forschungszentrum Karlsruhe.

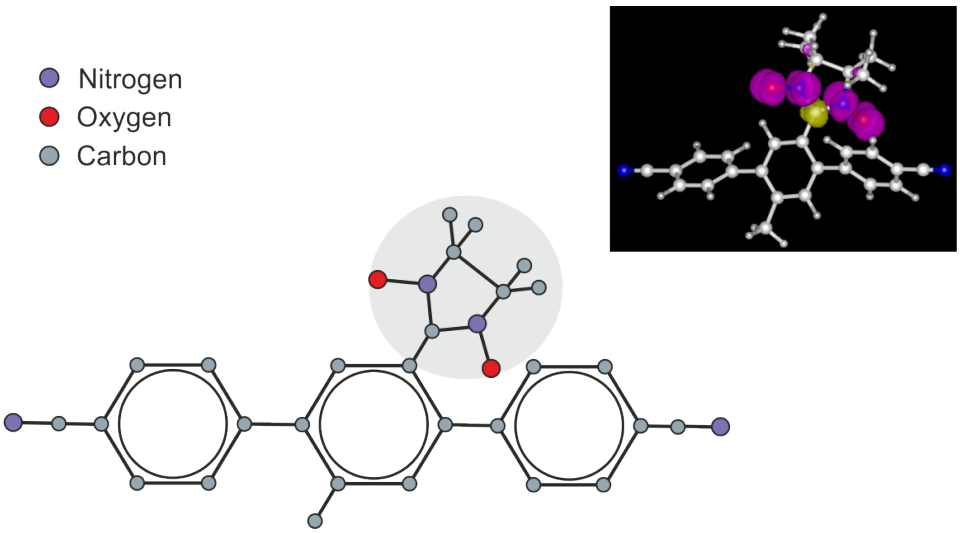

Figure 5.9.: Structure of the molecule, with the NIT group shaded in gray. The inset shows the spin density (violet and yellow represent oppsing spin orientations), which is localized on the NIT group. Inset produced by Duy Le, University of Central Florida, reprint with permission.

In this study the Kondo effect has been observed in a native spin-1/2 system, which is provided by the NIT group, while the terphenyl backbone provides sufficient separation from the substrate to avoid charge transfer, which would likely cancel the spin. Through the use of a purely organic molecule the spin is based on the more simple *s*- and *p*-orbitals, which further minimizes theoretical complexity. While this is not the first study to observe a Kondo feature in an organic molecule [140, 141], it is the first study with the spin as an intrinsic property of the molecule instead of being created upon deposition by charge transfer.

In the following I will present the first STM study of a unambiguous spin-1/2 Kondo system with detailed temperature and magnetic field dependance.

5.2.2. Sample Preparation and Imaging

We have deposited the nitronyl nitroxide derivates on a Au(111) surface to make them individually addressable by STM. The gold surface was cleaned prior to deposition by cycles of Ar^+ sputtering and annealing to approximately 800 K (standard procedure). The molecules, available in form of a crystal powder containing equal amounts of the radical and dichlormethane (CH_2Cl_2), were heated inside a quartz crucible opposing the sample surface in UHV.

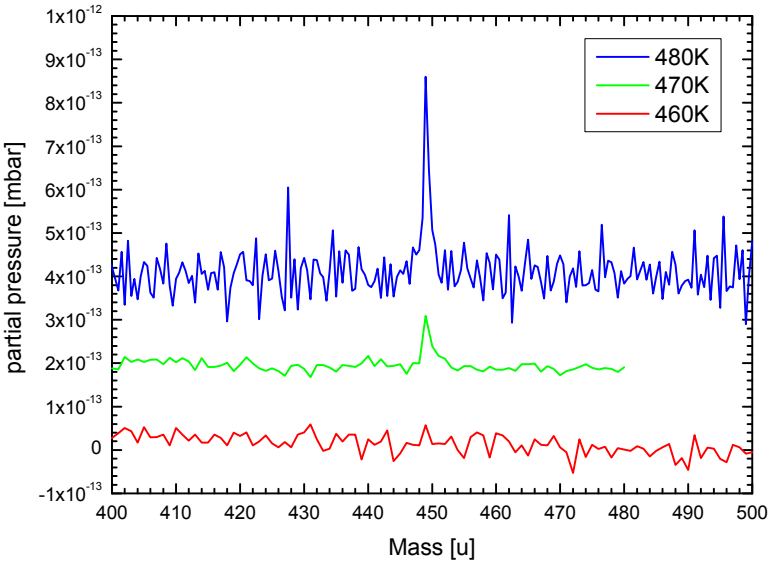

Figure 5.10.: Mass spectra for calibrating the evaporation temperature of the nitronyl nitroxide. The crucible containing the radical was mounted opposing a mass spectrometer and slowly heated to increasing temperatures. Measurements have been performed in high vacuum (10^{-8} mbar) in a separate vacuum chamber. The spectra are vertically offset for clarity.

Since the sublimation rate depends very critically on the temperature, a suitable evaporation temperature had to be established to obtain sub-monolayer coverages. For this the same crucible was mounted in front of a mass spectrometer and the temperature was successively increased until a peak at the molecular mass of 449 u appeared at 470 K (see figure 5.10).

The molecules were heated to 470 K and deposited for durations of 30 seconds to 10 minutes. Deposition at room temperature led to clustering and nucleation at step edges. To reduce the molecular mobility, the Au samples were cooled to $150 - 170$ K during the deposition. STM imaging has been performed at temperatures of 4.3 Kelvin or below, see figure 5.11 for overview images at different coverages. At higher coverages the molecules are forming molecular chains. While this study focuses on the Kondo behavior of individual molecules, the chain formation at higher coverages or in radical-metal-compounds has been simultaneously studied by Zhang [163].

As can be seen in figure 5.11 the molecules tend to adsorb on the elbow sites of the reconstructed Au(111). The characteristic shape consists of a central structure, which can be attributed to the actual NIT molecule, neighboured by smaller bumps on opposing sides of the central molecule. The outer structures are dichlormethane molecules (CH_2Cl_2) contained in the crystal powder, which appear to be bound to the nitrogen

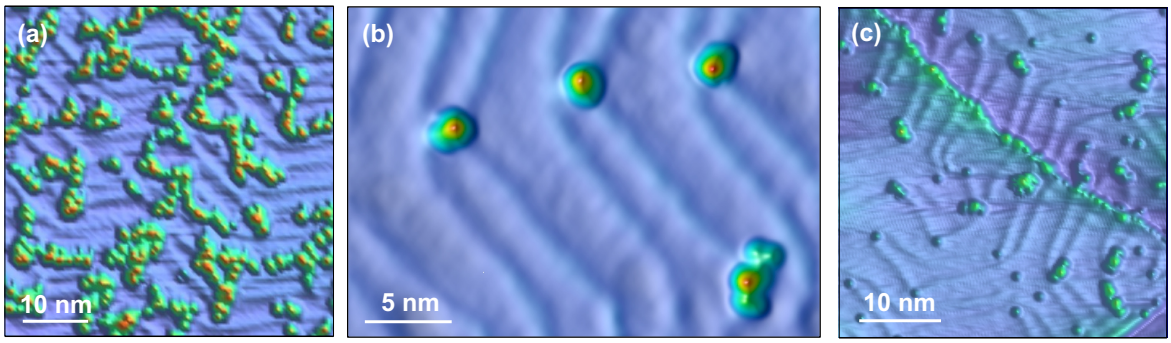

Figure 5.11.: (a) At high coverages the molecules start to form chains. Deposition: 480 K for 20 min, to study single molecules lower coverages are preferred (b,c) Deposition 480 K for 2 min. Tunneling parameters: (a) V=-150mV, I=25pA; (b) V=+50mV, I=30pA; (c) V=-1V, I=30pA.

atoms on either side of the nitronyl nitroxide. The CH_2Cl_2-groups can be removed from the NIT by positioning the tip over them and applying a bias pulse of several Volts.

Detailed topographies of the NIT molecule (figure 5.12) show the elongated molecular backbone and the radical side group, which is imaged as an approximately 0.3 nm high and 1 nm wide protrusion. The increased apparent height of the side group over the backbone indicates a large distance/weak coupling of the side group with the metallic substrate. While the majority of NIT is decorated by CH_2Cl_2, also undecorated NIT can be found. The Kondo resonance – which is described in the next sections – appears regardless of the existence of CH_2Cl_2 molecules at the ends of the molecular backbone.

5.2.3. Kondo Resonance - Temperature Dependance

When measuring the LDOS over the molecule we detect a strong resonance at the Fermi level at the site of the nitronyl nitroxide group. The resonance is found neither on the backbone of the molecule nor on the clean surface. Furthermore, the observation of this resonance on single molecules does not depend on the presence of adsorbates close to the molecule or its orientation with respect to the Au(111) substrate, while its apparent width and amplitude varies slightly between different molecules. Spectra have been taken at temperatures between 1.5 K and 16 K on a total of about 25 molecules.

Figure 5.13 shows the development of the Kondo resonance over different temperatures. A strong broadening towards higher temperatures can be observed, while in the accessible temperature range down to 1.5 K no minimal natural peak width seems to emerge.

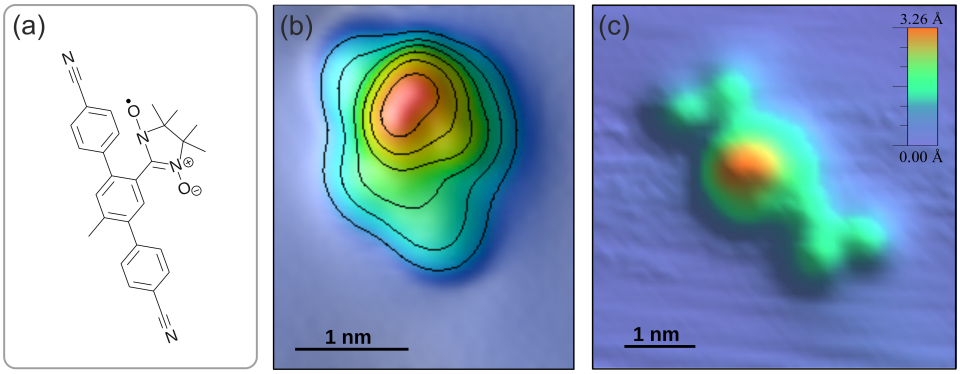

Figure 5.12.: (a) Chemical structure of the nitronyl nitroxide. (b) Detailed topography of a single molecule. Contour lines are at height intervals of 50 pm (V=100 mV, I=33 pA). (c) Detailed topographies of a molecule decorated by four dichlormethane molecules attached to the nitrogen atoms at both ends of the molecular backbone (V=−200 mV, I=25 pA).

The LDOS was measured on different locations on the sample by Scanning Tunneling Spectroscopy (STS), with typical tunneling setpoints before deactivating the feedback loop of $V_{\text{bias}} = -20$ mV and $I_T = 0.1 - 1$ nA. Spectra were typically taken in a range of −20 mV to +20 mV symmetrically around zero bias. V_{LI} was chosen to be small enough that the signal broadening due to the modulation voltage was always less than the thermal broadening; more precisely $V_{LI}(\text{rms}) < \frac{1}{2}5.4\,k_B T$, resulting in typical used values of $V_{LI}(\text{rms}) = 0.1 - 0.3$ mV at low temperatures while at higher temperatures ($T > 5$ K) $0.5 - 1$ mV was used.

Before and after spectra were measured on the radical, reference spectra have been taken on the clean Au surface to ensure a featureless conductance of the tip. The measured spectra were normalized and a linear baseline was subtracted to account for drift effects which were also visible in the reference spectra.

The attribution of a zero bias peak in the LDOS as a Kondo resonance can be done by analyzing the peak shape and its temperature behaviour. Here I will discuss the experimental observations with regard to two different models:

- For temperatures below the Kondo temperature ($T < T_K$), the strong coupling model applies as described in section 5.1.5. The strong coupling model is widely used in STM studies of Kondo impurities [14, 129, 140, 149–151, 164].
- The Appelbaum model [145, 147] as described in section 5.1.4. As a perturbative approach it is only valid in the weak coupling regime ($T > T_K$).

As the Kondo temperature is a priori unknown, both models have been used to obtain fitting curves. As can be seen in figure 5.13 both models offer an overall good fit quality

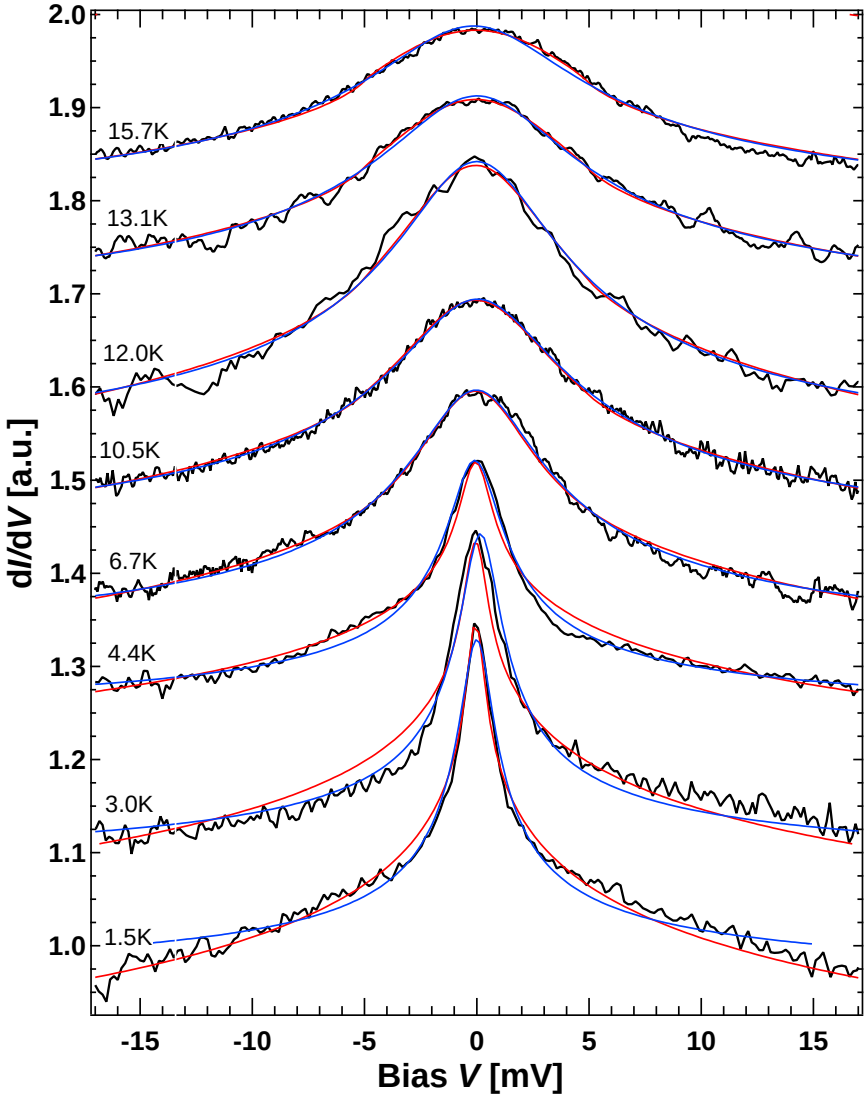

Figure 5.13.: Typical differential conductance spectra taken on the radical side group of the molecule at temperatures between T = 1.5 K and T = 15.7 K (black), simulated spectra using the weak coupling model (red) and the strong coupling model (blue). All spectra are normalized and offset for visual clarity.

over the observed temperature range, with excellent agreement at higher temperatures (above 5 K) and more deviations from the measurements at lower temperatures.

As discussed in the techniques chapter (section 2.2.4), measuring the sharpness of any STS feature is limited by the temperature broadening of the involved Fermi levels and the additional broadening due to the finite size of the modulation voltage in the lock-in-technique (LI). While the latter one can be chosen sufficiently small to not significantly broaden the results, the temperature induced broadening increases towards higher temperatures and must not be confused with the intrinsic broadening of the Kondo feature itself. For both models care was taken to correct the observed spectra for these effects.

Strong Coupling Model

The Frota function as written in equation 5.18 was used to fit the measured data (see figure 5.13) yielding the peak width and height as fit parameters. Since the hereby obtained width Δ_{fit} includes the temperature- and LI-broadening from the measurements, these factors have to be corrected to gain the real width Δ.

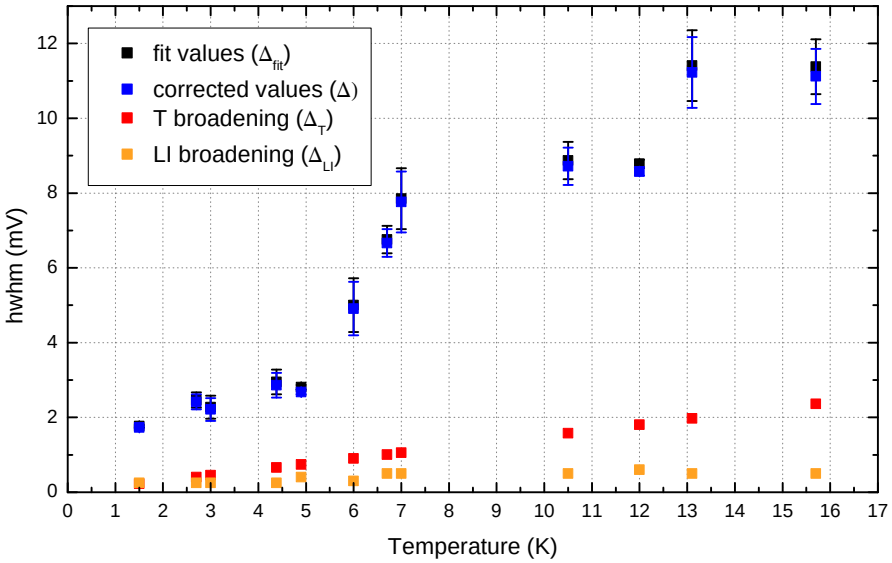

Figure 5.14.: **Correction Terms**. The hwhm-values for different temperatures as obtained from the Frota-fits (black), and with the correction terms applied (blue). Error bars result from averaging over different molecules. The correction terms due the finite sharpness of the tip's Fermi level (red) and the modulation voltage of the lock-in-amplifier (orange) are shown for comparison.

While formally a deconvolution of the measured line-shape with the shape of the temperature- and LI-broadening is necessary, we assume that all three curves can be approximated by a Gaussian distribution and that the half widths of the corrections terms (Δ_T, Δ_{LI}) are small against the real width Δ. That enables us to use the relation $\Delta_{fit}^2 = \Delta_T^2 + \Delta_{LI}^2 + \Delta^2$ (from section 2.2.4) to deduce the real width. Figure 5.14 shows the original and the corrected values. It can be seen, that the correction terms are indeed small against the measured values. Thus, the corrected terms can represent the real widths accurately.

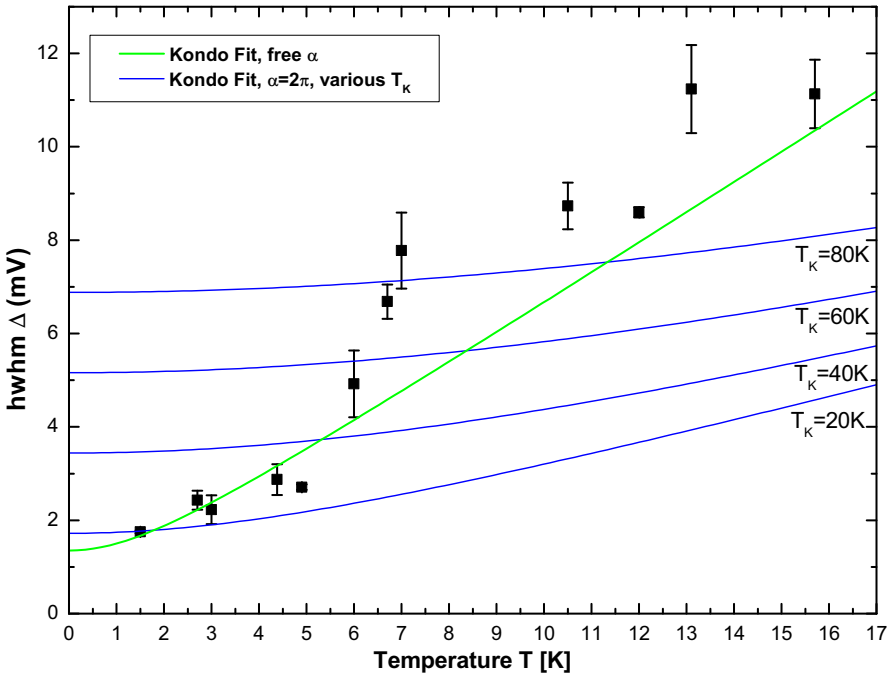

Figure 5.15.: Temperature dependence of the width of the Kondo resonance as extracted from Frota fits. Black squares denote the corrected values Δ. The family of blue curves follows the strong coupling model with $\alpha = 2\pi$ and different T_K. The green curve fits the data with α and T_K as fit parameters.

Using the corrected values we compare the experimental results with the expected behaviour from the strong coupling model (equation 5.16) and try to deduce a Kondo temperature in this framework. As can be seen in figure 5.15 the increase of the widths Δ over temperature is much stronger than expected in this model, where the slope is mainly given by the parameter $\alpha = 2\pi$. The model fails to describe our data. If we anyhow estimate the Kondo temperature by extrapolating the width to zero temperature, for which we let α be a free fit parameter, we obtain an unphysically high $\alpha = 15.2 \pm 0.9$ and a Kondo temperature of $T_K = 15.7 \pm 2.5$ K.

Weak Coupling Model

As described in section 5.1.4, the weak-coupling model by Appelbaum suggests that without magnetic field the observed Kondo resonance assumes the form

$$\frac{\mathrm{d}I}{\mathrm{d}V}(eV) = -aF(eV) + \text{offset}, \tag{5.19}$$

with $F(eV)$ as defined in equation 5.11. At zero temperature $F(eV)$ is a logarithmic singularity of infinite sharpness, at finite temperatures the logarithmic peak broadens due to the broadened Fermi levels of both tip and sample. Inserting the complete expression for $F(eV)$ from equation 5.11 results in

$$\frac{\mathrm{d}I}{\mathrm{d}V}(eV,T) = -a\int_{-\infty}^{+\infty}\left(\int_{-E_0}^{+E_0}\frac{1}{\epsilon-\omega}f(\epsilon,T)\ \mathrm{d}\epsilon\right)f'(\omega-eV,T)\ \mathrm{d}\omega + \text{offset}, \tag{5.20}$$

where the only fit parameters necessary are the amplitude a, the cutoff energy E_0, and the temperature T. The function $f(eV,T)$ denotes the Fermi distribution and $f'(eV,T)$ its derivative with respect to the energy eV. The temperature T should resemble the temperature of the measurement. Since we use normalized spectra our offset is always one. For numerical reasons both integrals where performed up to the cutoff energy E_0, which was chosen to be twice as high as the measured range of the spectra to avoid convolution artifacts from the sides of the spectra.

The convolution with the Fermi function serves not only as a correction factor to increase the peak width, but replaces the unphysical singularity at zero bias with a curved shape of finite height. At the same time the constant decline of conductivity towards higher voltages is not affected by the convolution. This allows for a more precise modeling of the conductivity as shown in figure 5.16:

When modeling the very sharp resonances observed at low temperatures ($T < 5$ K) with a Frota function, the sharpness of the peak can only be produced correctly at the expense of a too weak signal decline towards higher bias (and vice versa). The logarithmic shape allows for an almost perfect fit over the whole bias range.

When plotting the spectra with a logarithmic abscissa (fig. 5.17) the logarithmic voltage dependance of the signal over almost two orders of magnitude is visible. In this representation the temperature broadening appears as a flat peak top, whose width scales with the thermal energy k_BT.

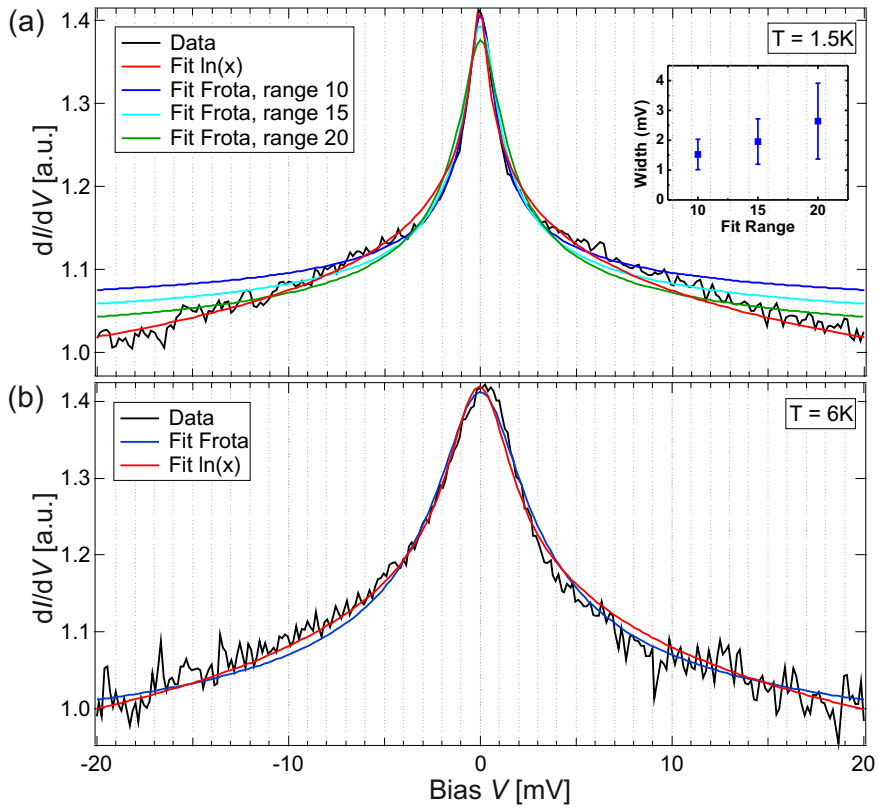

Figure 5.16.: **Comparison of different fit models.** (a) At low temperatures like 1.5 K the logarithmic model fits the data over the whole observed bias range. The fit by the Frota-function depends on the used range in which the data is fitted: Either the sharpness of peak or the decline of the signal at higher voltages can be reproduced. The obtained half-width depends on the fit range (inset). (b) At higher temperature these differences vanish and the data can be fitted by both models equally well.

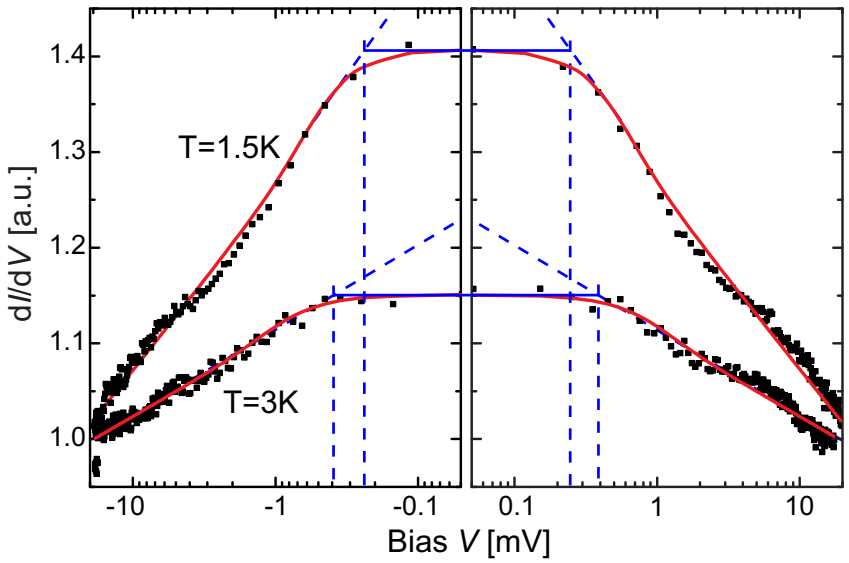

Figure 5.17.: Two exemplary spectra (black dots) and the conductance modeled by the Appelbaum model (red line) plotted with logarithmic abscissa. The blue lines mark the flat top range (intersection between an extrapolation of the logarithmic increase in the conductance and the conductance at zero bias, shown by dashed blue lines) whose width scales with temperature.

The extracted fit parameter T_{eff} should reproduce the temperature of the experiment, and thus can be used as a test of the validity of our model. In figure 5.18 we plot T_{eff} over the experimental temperature T obtaining good agreement with deviations towards lower values for T_{eff} at temperatures $T < 6$ K.

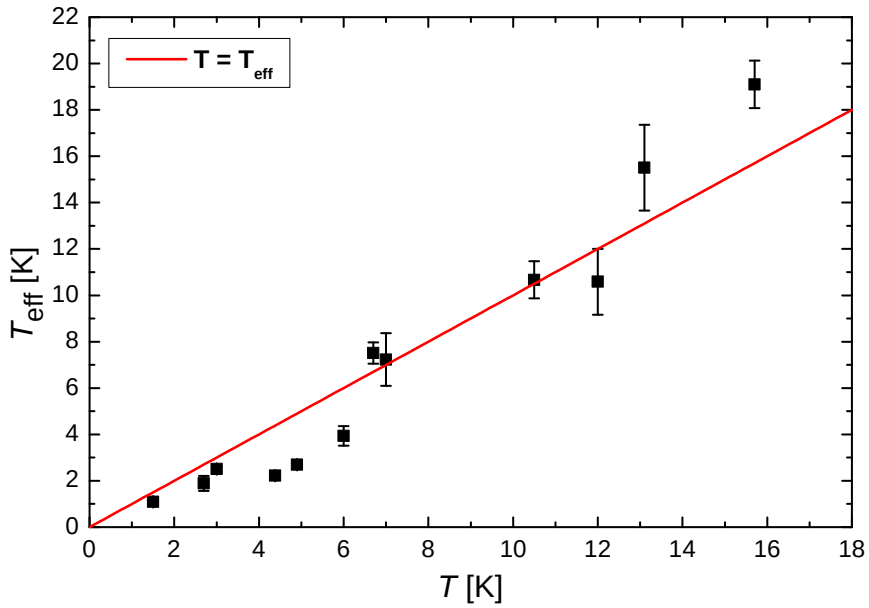

Figure 5.18.: Plot of the effective temperature T_{eff} obtained by fitting spectra with the Appelbaum model versus the experimental temperature T. The red line marks $T_{\text{eff}} = T$. Error bars include the variation from the spectra taken on different molecules.

In equation 5.13 the Appelbaum model offers a relation of peak height to background conductance, which could be used to calculate the coupling intensity $J\rho$. Unfortunately, STM measurements do not reproduce a viable ratio of peak height to background conductance in the sense of the Appelbaum model, which will be discussed in the following section.

Peak Heights

Also the peak height of a Kondo resonance has a characteristic temperature behaviour, which has been observed in quantum dots [165]. STM studies have not been able to successfully use this relation so far due to complications determining the actual resonance height from spectroscopic data and the necessity of data from a wide temperature range.

When an STM tip is positioned over a Kondo impurity like an atom or a molecule, only a part of the tunnel current actually passes through the impurity. Depending on the exact shape and position of the tip, electrons can either tunnel through the Kondo impurity into the substrate, or they can directly tunnel into the substrate bypassing the impurity (see fig 5.19a). Even the electrons passing through the impurity are not necessarily using the Kondo resonance but can also tunnel elastically through the DOS of the substrate. This results in a considerable background current (which in our case is bigger than the resonance amplitude)(fig 5.19b).

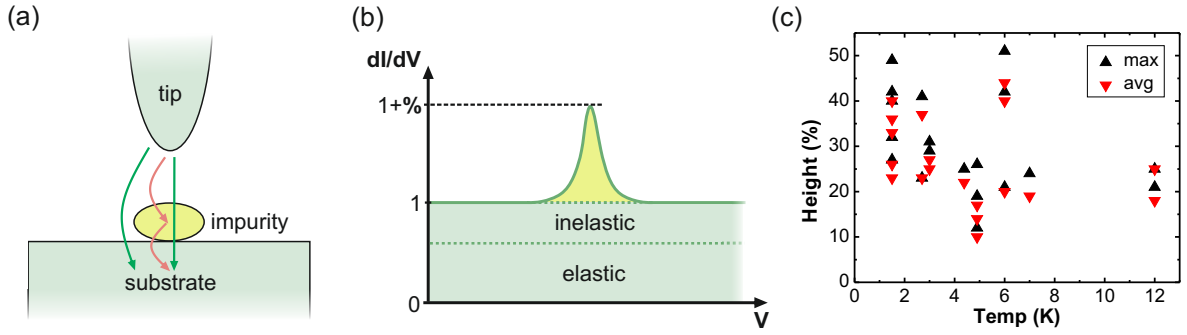

Figure 5.19.: (a) The electrons can either tunnel through the Kondo resonance at the impurity (light arrow) or through another orbital or bypass the impurity at all (dark arrows). (b) We normalize our spectra to the background conductance, which consists of an elastic component and an inelastic spin-flip component (indistinguishable at zero field). The peak height is given relative to the background. (c) Peak heights plotted over temperature. Each data points represents the maximum (black) or the average (red) value of all measurements of one molecule.

Since minute variations in the position of the tip over the impurity cannot be avoided – particularly while changing the temperature – the peak height varies from measurement to measurement. Since this variation affects also the ratio of peak height to background current, the normalization of the spectra by setting the background to unity does not solve this problem.

Figure 5.19c shows the measured peak heights as percentage of the background current. The heights have been obtained by evaluating the maximum value of each spectrum and show a declining trend towards higher temperatures. The peak height is hereby a parameter which is independent of the used model. Since the variations in peak heights can be partially attributed to an imperfectly positioned tip, we use the maximal height values observed on each molecule for further analysis instead of the average ones to reduce the deviation from an optimal setup.

According to observations on quantum dots [165] and NRG calculations [166] the height of a Kondo resonance decreases with increasing temperature following

$$G(T) = G_0 \left(\frac{T_K'^2}{T^2 + T_K'^2} \right)^s . \tag{5.21}$$

The maximum peak height G_0 is reached at zero temperature and T_K' is defined as $T_K' = T_K/\sqrt{2^{1/s} - 1}$ so that the amplitude is $G_0/2$ at the Kondo temperature T_K. The exponential factor s is $s = 0.22$ for a spin-½ system [167]. As shown in figure 5.20a the curves saturate only for temperatures far away from T_K.

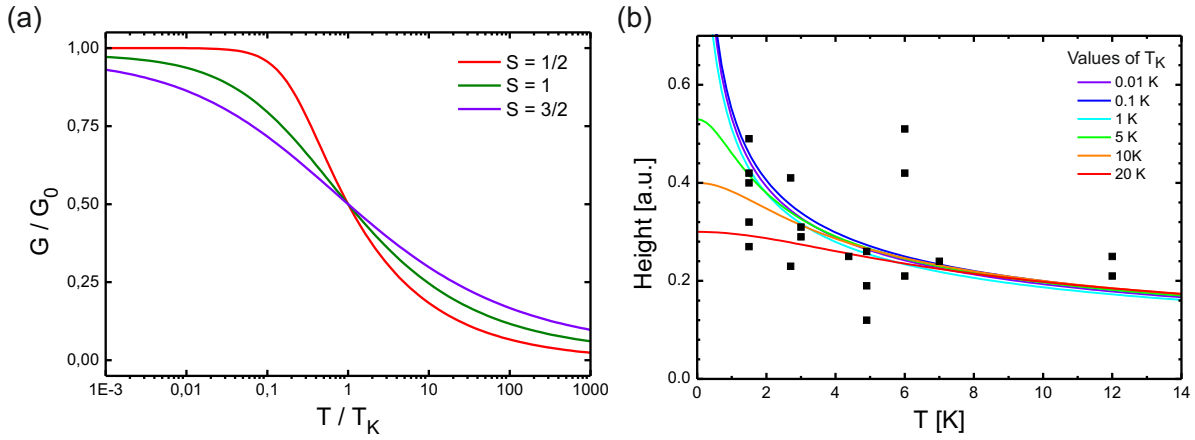

Figure 5.20.: (a) Peak heights plotted over temperature for Kondo impurities of spin S with a single screening channel (resulting in a fully screened model for $S = ½$ and underscreened for $S > ½$). Plots according to [167]. (b) As long as we are not in the saturation regime far below T_K, the amplitude G_0 is unknown, and we can generate identical curves in the observed temperature range even for very different values of T_K, which all fit the data. Only Kondo temperatures above 10 K result in different curves for the observed range. Curve parameters: T_K=20 K, G_0=0.3; 10 K, 0.4; 5 K, 0.53; 1 K, 1; 0.1 K, 3; 0.01 K, 8.

Since the maximum peak height G_0 is unknown for our system, the peak heights shown in figure 5.19c are given in arbitrary units. Therefore we cannot determine T_K from fitting equation 5.21 to our data, since by choosing an amplitude G_0, we can obtain almost any value for T_K (fig 5.20b). Anyhow, the observed increase in peak height towards lower temperatures suggests that we are not in the saturation regime. From this we estimate an upper limit of the Kondo temperature of $T_K \leq 10$ K. Even experimentally eliminating the discussed variations between individual measurements would not allow for a direct determination of T_K, since a much wider temperature range would be necessary for this.

Discussion

The main goal of this analysis is to identify the Kondo temperature T_K of the observed system. The Kondo temperature determines, whether our measurement have been performed at temperatures above T_K in the weak coupling regime, at temperatures below T_K in the strong coupling regime or in the cross-over regime $T \approx T_K$. At a first glance, both models fit the lineshape of the observed peak reasonably well (fig. 5.13).

When assuming the typically used strong coupling regime, the peak broadens with increasing temperature more than expected, showing an almost linear increase in the observed temperature range (figure 5.15). The slope of this linear increase is described by the parameter α, which assumes an unphysically high value of $\alpha = 15.2$ compared to $\alpha = 2\pi$ as expected from Fermi-liquid theory. This opposes that we are in the strong coupling regime of $T < T_K$. Nevertheless, we can estimate a limit for the Kondo temperature by using its definition as peak width at zero temperature (eq. 5.15). Since the peak width at zero temperature – regardless of the model – has to be lower than at all finite temperatures, we can limit the peak width to be smaller than the measured minimum of 1.75 meV which equals $T_K < 20$ K. The temperature behaviour of the peak height supports this result, by estimating an upper limit for T_K of 10 K.

When assuming the weak coupling regime, the temperature behaviour can be much better reproduced (fig. 5.18) and also the logarithmic lineshape seems to fit the data excellently (fig. 5.17). Since a logarithmic shape has a continuous decay of signal intensity towards higher bias values, no half-width can be defined. This explains the unphysically strong increase of apparent peak width described in the strong coupling model.

The validity or respective non-validity of these models indicates that the actual Kondo temperature lies below the observed temperate range, making this the first STM study of a Kondo system in the weak coupling regime with a unprecedentedly low Kondo temperature of $T_K < 1.5$ K.

For temperatures below 6 K the values of T_{eff} in the Appelbaum model deviate from the ideal curve (fig. 5.18), while the widths at the same temperature range produce a more reasonable slope in the strong coupling model with an inconsistently high Kondo temperature of around 30 K (fig. 5.15). This might be an indication that we approach the cross-over regime at the lower end of the observed temperature range. Furthermore, the coupling between conduction electrons and the impurity spin is clearly antiferromagnetic ($J\rho < 0$) since the resonance appears as a peak instead of a dip in the conductivity.

5.2.4. Kondo Resonance - Magnetic Field Dependance

The magnetic field dependance of the Kondo resonance has been measured at magnetic fields up to 14 T. The field has been applied perpendicular to the sample surface and measurements have been performed at the lowest possible temperature of 1.5 K for optimal spectroscopic resolution.

As can be seen in figure 5.21 the Kondo peak splits into two peaks already at fields as low as 2 T. Measurements at smaller fields have not been performed since the spectroscopic resolution at 1.5 K is 0.45 meV ($3.5k_BT$), which is not sufficient to detect the splitting for example at 1 T, which is 0.23 meV ($2g\mu_BH$) assuming a Landé factor of $g = 2$. At higher magnetic fields the spectra are dominated by symmetric steps representing spin flip excitations with the splitted Kondo peak superimposed on top of the steps.

At $T \ll T_K$ the Kondo cloud screens the magnetic impurity resulting in a non-magnetic ground state, which is unaffected by small magnetic fields. A splitting of the Kondo resonance and the appearance of spin excitations is only expected above a critical field $B_C = \frac{1}{2}k_BT_K/(g\mu_B)$, where the Zeeman energy is comparable to the Kondo screening [168]. We observe a clear splitting at fields as low as 2 T, which yields an upper limit of $T_K \leq 5.4$ K.

Thus, we assume that we are in the weak coupling regime, and use the Appelbaum model to obtain a quantitative description of the splitting as function of the magnetic field. Equation 5.12 describes the conductance at magnetic fields with the Kondo resonance split into two peaks shifted by the Zeeman energy $\Delta = g\mu_BH$ and a pair of step functions at the same energy Δ describing spin excitations of a free spin. We calculate the prefactors in equation 5.12 for a spin-$^1/_2$ system to be able to determine the fit parameters Δ and $J\rho$, with ρ as the LDOS of the sample.

Figure 5.22a shows the obtained fit values for the Zeeman energy Δ at different magnetic fields. It scales linearly with the applied magnetic field and yields a Landé factor $g = 1.94 \pm 0.04$, which differs from the expected value for a free electron, $g_0 = 2$. This difference provides an estimate for the exchange interaction J: Due to the coupling of the localized spin with the conduction electrons and their polarization by the magnetic field, the effective Landé factor will be modified compared to the value for the free spin [169]. From g we obtain $J\rho = -0.03 \pm 0.02$ at the highest magnetic fields, where the measurements are most accurate (figure 5.22b).

We derive a second independent estimate of $J\rho$ by comparing the amplitudes of the different scattering orders in equation 5.12: The height of the logarithmic peak from the

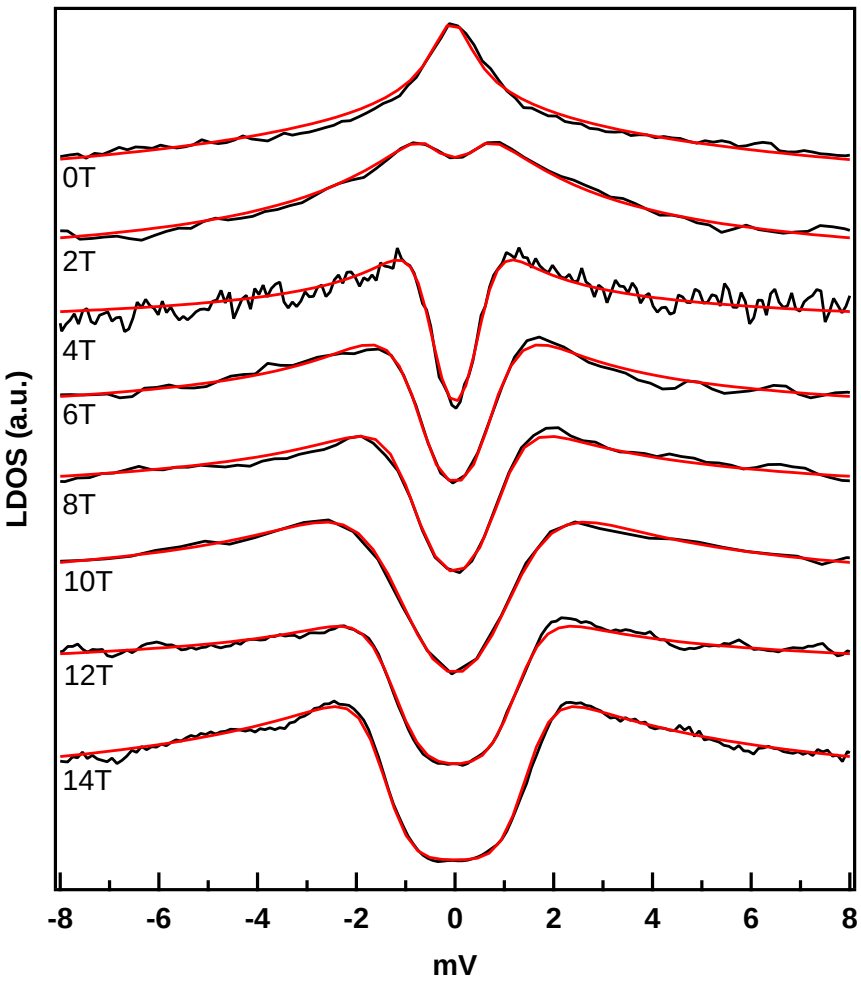

Figure 5.21.: Differential conductance measurements taken at different magnetic fields on the radical side group of the molecule at 1.5 K. All spectra are normalized and offset for clarity. Red curves are fits using the Appelbaum model.

third order terms is proportional to $(J\rho)^3$ while the amplitude of the spin-flip steps from the second order terms is proportional to $(J\rho)^2$. This yields $J\rho = -0.044 \pm 0.015$, in good agreement with the value obtained from the Zeeman splitting (figure 5.22b).

For comparison we also used the strong coupling model to fit the magnetic field data. We used two Frota functions F, shifted by the Zeeman energy Δ, combined with a pair of symmetric step functions Z identical to the ones in the Appelbaum model leading to a total fit function of

$$G(eV) = a_F \left[F(eV + \Delta) + F(eV - \Delta)\right] + a_Z \left[Z(\Delta + eV) + Z(\Delta - eV)\right], \qquad (5.22)$$

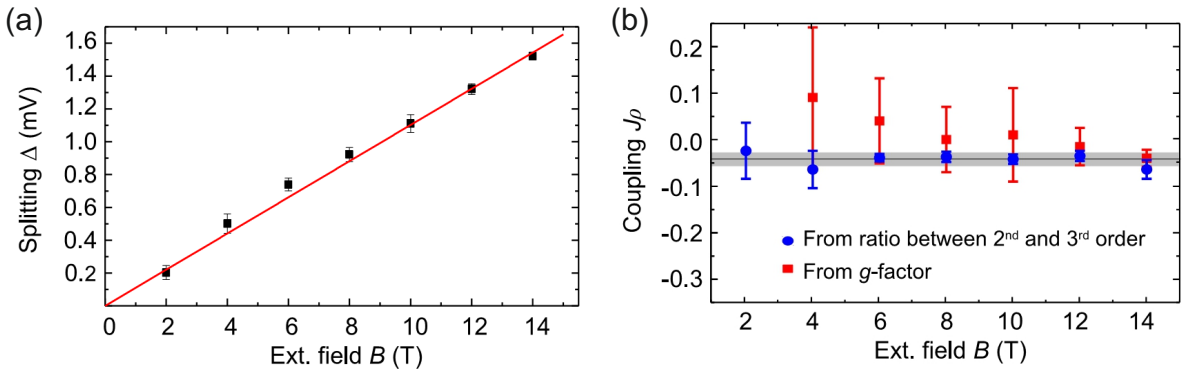

Figure 5.22.: (a) Extracted Zeeman splitting as function of the magnetic field. A linear fit (red line) yields $g = 1.94 \pm 0.04$. (b) Magnetic coupling $J\rho$ obtained from the Zeeman splitting (red dots) and from the ratio between 2nd and 3rd order contributions to the fit (blue dots). The average value of $J\rho = -0.044 \pm 0.015$ (grey line) has been obtained from the latter one. Error bars in (a) and (b) are due to the variation of spectra taken on different molecules.

with the according amplitudes a_F and a_Z. This fit function differs from the Appelbaum model mainly in the shape of the peaks. Fitting the experimental data yields values for the Zeeman splitting Δ, a comparison of the obtained values for both models are shown in figure 5.23. The most pronounced differences in Δ between the models can be found at lower magnetic fields, where the influence of the peak shape on the total fit function is most important. The symmetric shape of the Frota function fails to produce the steep dip at zero bias as observed in the data (cf.. figure 5.21). Therefore the strong coupling model yields a slightly higher value for the Landé factor of 2.04 ± 0.07.

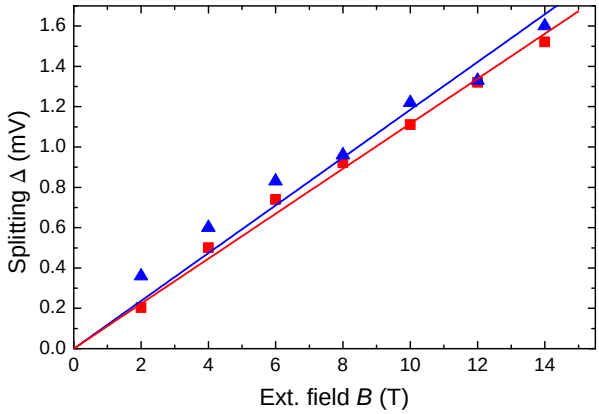

Figure 5.23.: Comparison of the extracted Zeeman splitting Δ from different models. Values have been obtained from the Appelbaum model (red) and from the strong coupling model (blue). Linear fits require crossing the origin.

5.2.5. Discussion

In the past, Kondo resonances on single atoms and molecules have usually been interpreted in the strong coupling limit. The temperature behaviour of the peak and the peak splitting at fields as low as 2 T are both inconsistent with an interpretation of an anitferromagnetic spin-1/2 Kondo model in the strong coupling regime.

Thus, a Kondo temperature below the observed temperature range of $1.5 - 16$ K has been assumed, representing a weak coupling between impurity spin and conduction band. Using the weak coupling theory developed by Appelbaum we have obtained excellent agreement with the measured data, particularly for the lineshape of the peak at very low temperatures close to 1.5 K. The model yields a Landé factor for the impurity of $g = 1.94 \pm 0.04$, close to the value of a free electron, which further confirms our spin-1/2 assumption.

A ferromagnetic coupling ($J\rho > 0$) can be ruled out, since we obtain a negative $J\rho$ from the Appelbaum model and the resonance would appear as a dip instead of a peak for ferromagnetic coupling.

We conclude that the resonance we observe is due to a single unpaired spin with weak antiferromagnetic coupling to the conduction band. 50 years after Kondo identified the correct Hamiltonian for a single magnetic impurity in a metallic host and showed the break-down of perturbation theory on a characteristic energy scale, our results demonstrate its validity for a single spin-1/2 impurity in the weak coupling regime which is characterized by an almost parameter-free universal temperature and magnetic field dependence.

Even though zero bias anomalies have been observed previously on purely organic molecules adsorbed on metal surfaces, the quantitative level of agreement between the data and theory is unprecedented for measurements on single impurities by low temperature STM. The identification of a true spin-1/2 system allows to perform quantitative tests of theoretical predictions, which can be performed at even lower temperatures. Besides enabling studies of spin-1/2 Kondo physics on a single impurity, experiments on systems of coupled impurities are conceivable. This can be of particular utility, since most theoretical studies of Kondo lattices are build on top of spin-1/2 Kondo impurities. Tailoring of the back bone in the synthesis of the molecules facilitates self-assembled growth of ordered one- or two-dimensional lattices of these molecules. This potentially allows for experimental studies of model Hamiltonians for correlated electron materials.

6. Summary and Outlook

With novel disciplines like molecular electronics the implementation of single molecules as functional units in information technology is approaching. This requires a more detailed understanding of the behaviour of individual molecules and the influence of the local environment on their properties. In this thesis the magnetic properties of individual molecules have been studied experimentally by means of scanning tunneling microscopy (STM) and scanning tunneling spectroscopy (STS). The results of this thesis will be presented in two parts. Examples for future experiments will be given at the end of each part respectively. Also the possibilities of the now working combined STM/AFM will be considered.

In the first part we have investigated different molecular magnets by means of spin-flip spectroscopy to identify whether they retain their molecular magnetic moment when deposited on different surfaces.

We have studied the archetypical molecular magnet Mn_{12} deposited on Au(111) surfaces and on a monolayer of BN on Rh(111). The intact deposition of the fragile molecule has been achieved by using electrospray ion beam deposition and has allowed detailed STM imaging of Mn_{12} molecules of unprecedented quality. Furthermore, the STM imaging ensured that the spectroscopic results have been obtained on individual Mn_{12} molecules in a well defined environment.

Spin-flip spectroscopy has been performed on individual molecules at temperatures of 1.5 K and at magnetic fields up to 10 T. A symmetric step-like structure around the Fermi energy has been observed for the molecules deposited on BN/Rh substrates. Comparison with calculations based on a spin Hamiltonian supported by DFT simulations has shown, that these steps can be interpreted as spin excitations, demonstrating the intactness of the molecular spin. The observed excitations change not only the orientation of the total molecular spin, but also the arrangement of the atomic spins within the molecule, showing the limitations of the giant spin approximation. The Mn_{12} molecules on Au showed no spectroscopic features, indicating a quenched spin probably due to the reduction of the Mn atoms upon deposition.

These results present the first observation of the magnetic moment of an individual Mn_{12} molecule in a well defined environment and successfully demonstrates the use of a BN monolayer as a decoupling layer to avoid the spin canceling reduction of the Mn atoms on metal surfaces.

A similar experimental strategy was employed to study the magnetic properties of Cr_7Ni on Au(111) and BN/Rh(111) surfaces. Imaging of Cr_7Ni on Au showed individually addressable molecules, but spectroscopy of the molecules has shown no signature of spin-flip excitations, indicating that either the magnetic moment has been quenched upon adsorption or that the signal intensity is too low to be measured with our setup. Stable imaging of Cr_7Ni deposited on BN/Rh has not been possible, presumably since the molecules were too weakly bond to the BN and have been dragged over the surface by the moving tip. For imaging of these samples a shorter tip-sample distance was required due to the insulating character of BN.

In future experiments it would be desirable to be able to discriminate between different spin directions by using a spin-polarized STM tip. This would allow lifetime measurements on a single Mn_{12} molecule prepared in an oriented ground state like $M = +10$. Changes in the magnetization could be observed by changes in the spin-polarized tunnel current giving access to the magnetic relaxation times of individual molecules. Applying small magnetic fields shifts the energy levels of the molecule and thereby controls the occurrence of quantum tunneling of magnetization, the main factor for magnetic relaxation at low temperatures.

With the combined STM/AFM we also have the option to measure the magnetization of the molecule and yet avoid excitations from the ground state by the tunnel electrons: The force between a magnetic tip and the molecule depends on the relative orientation between both spins, which should make changes in the magnetization of the molecule visible by AFM without the need of applying a bias voltage.

While the experiments on Mn_{12} have shown the feasibility of observing the characteristics of individual molecular magnets with our setup, other types of molecular magnets could be investigated in the same manner. Of particular interest could be a new derivate of Mn_{12} which shows no reduction of the Mn atoms when deposited on gold surfaces [82] and thus is a candidate to retain its magnetic moment also on metal surfaces.

The spectroscopic investigation of Cr_7Ni-*bu* on Au(111) surfaces showed no magnetic behaviour, thus making the use of a decoupling layer a sensible approach. Since studying Cr_7Ni-*bu* on BN/Rh was hindered by the unstable imaging conditions, other Cr_7Ni derivates or different decoupling layers (like KCl) could be investigated to achieve a stronger bonding to the substrate. The improved stability of the system in the new lab

environment could help by allowing lower tunnel currents or by providing a lower noise level in general.

In the second part of this thesis an organic radical based on a nitronyl nitroxide group (NIT) has been studied, whose unpaired electron is delocalized over several atoms stabilizing it against chemical reactions and charge transfer. The unpaired electron has no further orbital degeneracy and thus represents an ideal spin-$^1/_2$ system. The molecule retains its spin after deposition on a Au(111) surface and a Kondo resonance is formed by coupling of the free spin to the conduction electrons of the substrate.

A detailed STS study of the Kondo resonance has been performed in a temperature range of $1.5 - 16$ K and at magnetic fields up to 14 T. While in the past zero-bias anomalies have usually been interpreted as Kondo resonance in the strong anitferromagnetic (AFM) coupling regime, our analysis of the temperature and magnetic field dependence has shown, that the resonance we observe is due to a single unpaired spin with weak AFM coupling to the conduction band. Our results match the predictions from the almost 60 years old Kondo perturbation approach and are the first experimental demonstration of its validity for a single spin-$^1/_2$ impurity in the weak coupling regime. Thus, our results can be used as a benchmark for spin-$^1/_2$ systems, which has been a subject of intense theoretical research.

An STM study at even lower temperatures reaching the Kondo temperature of the NIT system would allow insights into the crossover regime between strong and weak coupling for a single spin system. The theoretical treatment of this regime, known as the Kondo problem, so far lacks detailed experimental data for comparison.

Further conceivable experiments include the coupling of multiple of these spin-$^1/_2$ systems, or the use of the molecule as building block for Kondo lattices. The STM is ideally suited to couple multiple molecules in a controllable way either by arranging them in close vicinity on the surface or by attaching one to the tip and approach it to another one on the surface [131]. Also chemical tailoring of the molecular backbone can be used to enable self-assembly of the molecules in one- or two-dimensional structures. An organic molecule is an ideal candidate to study the coupling of multiple spins since its spin resides in a more delocalized orbital than in a transition metal or rare earth molecule. This should make the spin more accessible to its environment and the coupling by other spins.

The combined STM/AFM allows access to more fundamental, yet so far unaddressed magnetic properties. The magnetic force between two individual spins could be extracted from differential force measurements of parallel and antiparallel aligned spins to eliminate non-magnetic force components. To measure this force the two magnetic

atoms (or molecules) must be attached to tip and surface. Depending on the chosen materials this setup can incorporate a Kondo state on either side of the tunnel gap, allowing force measurements between two coupled Kondo systems, or – even more exiting – a Kondo state across the tunnel gap, which would allow fine tuning of the Kondo coupling distance and the measurement of a "Kondo force" [170].

A. The Boron Nitride "Nanomesh"

Boron nitride is a wide bandgap material consisting of equal amounts of boron and nitrogen atoms. In its most common crystal structure, hexagonal boron nitride (h-BN), it consists of hexagonally ordered monolayers, which are only weakly bond to each other, resembling the structure of graphite. Monolayers of h-BN have been grown on various metallic substrates like Ni, Pt [171], Ru [172] and Rh [173]. The atomic structure on all substrates is comparable to graphene with boron and nitrogen atoms alternating in a hexagonal lattice (fig A.1a). BN monolayers are very stable and stay intact in air [174], water [175], or at temperatures above 1000 K. In particular BN on Rh(111) has attracted much attention due to the formation of a regular "nanomesh" [173].

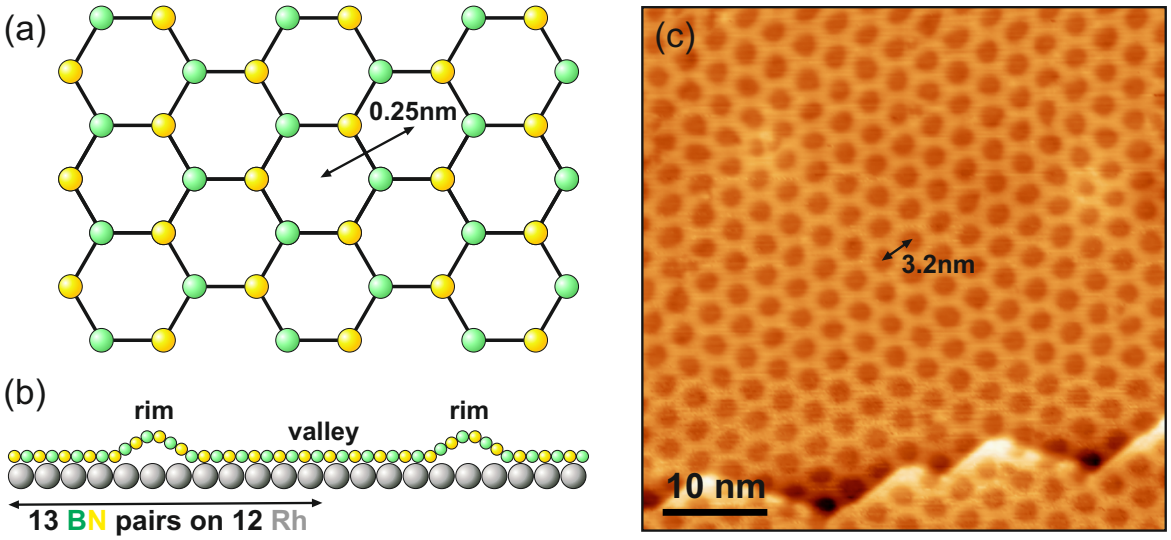

Figure A.1.: **(a)** Structure of a BN monolayer: boron (green) and nitrogen (yellow) atoms alternate in a hexagonal pattern forming a honeycomb lattice. **(b)** Cross section of a BN monolayer on Rh(111) (gray), which self-arranges in valleys separated by rims due to the lattice mismatch. **(c)** STM image of a BN/Rh surface showing the hexagonal superstructure of valleys and rims. Image Parameters: $V = -1$ V, $I = 80$ pA.

We prepare BN/Rh samples by chemical vapor deposition using borazine $(HBNH)_3$ as a precursor gas[1]. Clean Rh(111) surfaces are prepared by repeated Ar^+ sputtering

[1]The borazine was synthesized by Fanny Schurz, Dept. Jansen, Max Planck Institute for Solid State Research, Stuttgart

and thermal annealing. The atomically clean Rh surface is exposed to borazine gas via a leak valve at pressures of 10^{-6} mbar while being kept at 1070 K. The hot Rh acts as catalyst, splitting the borazine into BN and gaseous H_2, which limits the growth of BN on the surface to a monolayer. This self-limitation provides a very reliable procedure for monolayer growth, an advantage over other insulation layers, where exact dosing is required.

While BN grows flat on Ni(111) surfaces [176], it shows a corrugation on most other substrates due to a lattice mismatch with the underlying metal [173,177,178]. In the case of BN on Rh(111) 13 boron/nitrogen hexagons are sitting on top of 12 rhodium atoms (fig A.1b), resulting in a periodical structure with hexagonal valleys separated by a net of higher wires (fig A.1c) with a periodicity of 3.2 nm. This hexagonal superstructure must not be confused with the hexagonal arrangement of the atoms, which has a periodicity of 2.5 Å. This *nanomesh* acts as growth template allowing the organization of molecules in a bottom-up approach, an important requisite for many applications [179]. Different molecules or metallic clusters of similar size as the nanomesh pores are known to adsorp inside the pores [173, 175, 180].

Equally important the BN monolayer shows a band gap of $5 - 7$ eV on Rh(111), which decouples adsorbates from the underlying metal by preventing charge transfer [180–182]. The combination of these two properties make the BN nanomesh a promising decoupling layer for the deposition of functional molecules in ordered patterns.

Publications

- Steffen Kahle, Zhitao Deng, Nikola Malinowski, Charlène Tonnoir, Alicia Forment-Aliaga, Nicha Thontasen, Gordon Rinke, Duy Le, Volodymyr Turkowski, Talat S Rahman, Stephan Rauschenbach, Markus Ternes, and Klaus Kern. The Quantum Magnetism of Individual Manganese-12-Acetate Molecular Magnets Anchored at Surfaces. *Nano Letters* 12, 518–21 (2012).

- Yong-hui Zhang, Steffen Kahle, Tobias Herden, Christophe Stroh, Marcel Mayor, Uta Schlickum, Markus Ternes, Peter Wahl, and Klaus Kern. Temperature and Magnetic Field Dependence of a Kondo System in the Weak Coupling Regime. *Nature Communications* 4, (2013)

Danksagung

Zum Schluss möchte ich all jenen danken, die zum Gelingen dieser Arbeit beigetragen haben:

- Prof. Dr. Klaus Kern für die Vergabe des Themas und die Möglichkeit, in seiner Abteilung zu arbeiten.
- Prof. Dr. Elke Scheer und Prof. Dr. Peter Nielaba von der Universität Konstanz für die prompte Bereitschaft, als Gutachter und Prüfer meiner Arbeit zu fungieren.
- Dr. Markus Ternes für die Betreuung der Promotion, die stets schnelle Beantwortung all meiner Fragen und das Korrekturlesen dieser Arbeit.
- Tobias Herden, ohne den diese Arbeit in vieler Hinsicht so nicht möglich gewesen wäre, für die gute Zusammenarbeit und für das hervorragende Korrekturlesen meiner Arbeit.
- Dr. Peter Wahl für die gute Zusammenarbeit im Rahmen des *Weak-Coupling Kondo*-Projektes und für die Hilfe darüber hinaus.
- Carola Straßer, die als Büronachbarin alle Höhen und Tiefen miterlebt hat.
- Dr. Liza Herrera-Diez, Sören Krotzky, Dr. Ulrich Stützel und Dr. Theresa Lutz für ihre freundschaftliche Unterstützung.
- Dr. Markus Etzkorn für das geduldige Beantworten aller meiner Fragen, nur weil er im "falschen" Büro saß.
- Charlène Tonnoir für ihre Neugier und gute Laune während unserer Zusammenarbeit.
- Dr. Christian Michaelis für die hervorragende Übergabe des experimentellen Aufbaus.
- Wolfgang Stiepany, Peter Andler und Andreas Koch für ihre technische Expertise und ihre Hilfsbereitschaft.
- Allen Steuerzahlern, die Forschung mit so hohem personellen und technischen Aufwand erst ermöglichen.

Der größte Dank gilt meiner Lebensgefährtin Katharina Pott für ihr Verständnis und ihren Rückhalt während dieser Zeit.

Bibliography

[1] Richard P. Feynman. There's plenty of room at the bottom. *Engineering and Science*, 23:22–36, 1960.

[2] JM Daughton. GMR applications. *Journal of magnetism and magnetic materials*, 192:334–342, 1999.

[3] N. N. Ledentsov, V. M. Ustinov, V. A. Shchukin, P. S. Kop'ev, Zh. I. Alferov, and D. Bimberg. Quantum dot heterostructures: Fabrication, properties, lasers. *Semiconductors*, 32(4):343–365, April 1998.

[4] Jack Clark. Intel's 22nm Ivy Bridge chips set for launch. *ZDnet*, Apr 23, 2012.

[5] Intel Corporation. Intel to Invest More than $5 Billion to Build New Factory in Arizona. *Press Release*, Feb 18, 2011.

[6] Chris Nuttall. Intel's chip plans bloom in Arizona desert. *Fincancial Times*, Jan 22, 2012.

[7] International Technology Roadmap for Semiconductors. ITRS Update 2012. *http://www.itrs.net/*, 2012.

[8] S A Wolf, D D Awschalom, R A Buhrman, J M Daughton, S von Molnár, M L Roukes, A Y Chtchelkanova, and D M Treger. Spintronics: A Spin-Based Electronics Vision for the Future. *Science*, 294(5546):1488–95, November 2001.

[9] DP DiVincenzo. Quantum Computation. *Science*, 270(5234):255–261, 1995.

[10] G. Binnig and H. Rohrer. Scanning tunneling microscopy. *Helvetica Physica Acta*, 55:726–735, 1982.

[11] DM Eigler and EK Schweizer. Positioning single atoms with a scanning tunnelling microscope. *Nature*, 344, 1990.

[12] WJ de Haas, J de Boer, and GJ Van den Berg. The electrical resistance of gold, copper and lead at low temperatures. *Physica*, 1(233):1115–1124, 1934.

[13] J Kondo. Resistance minimum in dilute magnetic alloys. *Progress of Theoretical Physics*, 32:37–49, 1964.

[14] V. Madhavan, W. Chen, T. Jamneala, M.F. Crommie, and M.S. Wingreen. Tunneling into a Single Magnetic Atom: Spectroscopic Evidence of the Kondo Resonance. *Science*, 280(5363):567–569, April 1998.

[15] D Goldhaber-Gordon, H Shtrikman, D Mahalu, D Abusch-Magder, U Meirav, and MA Kastner. Kondo effect in a single-electron transistor. *Nature*, 391(January):1996–1999, 1998.

[16] G. Binnig, H. Rohrer, Ch. Gerber, and E. Weibel. Tunneling through a controllable vacuum gap. *Applied Physics Letters*, 40(2):178, 1982.

[17] G Binnig, H Rohrer, C Gerber, and E Weibel. Surface studies by scanning tunneling microscopy. *Physical Review Letters*, 49(1):57–61, 1982.

[18] FM Leibsle, CFJ Flipse, and AW Robinson. Structure of the Cu{100}-c(2x2)N surface: a scanning-tunneling-microscopy study. *Physical Review B*, 47(23), 1993.

[19] John Bardeen. Tunnelling from a many-particle point of view. *Physical Review Letters*, 6(2), 1961.

[20] Jerry Tersoff and Donald R Hamann. Theory and Application for the Scanning Tunneling Microscope. *Physical Review Letters*, 50(25), 1983.

[21] Jerry Tersoff and Donald R Hamann. Theory of the scanning tunneling microscope. *Physical Review B*, 31(2), 1985.

[22] G Binnig, KH Frank, H Fuchs, and N Garcia. Tunneling spectroscopy and inverse photoemission: image and field states. *Physical Review Letters*, 55(9):991–994, 1985.

[23] Andreas J. Heinrich, J A Gupta, C P Lutz, and D M Eigler. Single-atom spin-flip spectroscopy. *Science*, 306(5695):466–9, October 2004.

[24] Sebastian Loth, Kirsten von Bergmann, Markus Ternes, Alexander F. Otte, Christopher P. Lutz, and Andreas J. Heinrich. Controlling the state of quantum spins with electric currents. *Nature Physics*, 6(5):340–344, March 2010.

[25] R. Jaklevic and J. Lambe. Molecular Vibration Spectra by Electron Tunneling. *Physical Review Letters*, 17(22):1139–1140, November 1966.

[26] J. Lambe and R.C. Jaklevic. Molecular vibration spectra by inelastic electron tunneling. *Physical Review*, 165, 1968.

[27] B.C. Stipe. Single-Molecule Vibrational Spectroscopy and Microscopy. *Science*, 280(5370):1732–1735, June 1998.

[28] J. Gupta, C. Lutz, A. Heinrich, and D. Eigler. Strongly coverage-dependent excitations of adsorbed molecular hydrogen. *Physical Review B*, 71(11):115416, March 2005.

[29] J Klein, A Leger, M Belin, D Défourneau, and MJL Sangster. Inelastic-electron-tunneling spectroscopy of metal-insulator-metal junctions. *Physical Review B*, 7(6), 1973.

[30] Paolo Messina. *Towards Magnetic Engineering at Metal Surfaces*. PhD thesis, École Polytechnique Fédérale de Lausanne, 2003.

[31] Gero Wittich. *Scanning Tunneling Microscopy and Spectroscopy at Low Temperatures: Development of a 1K-Instrument and Local Characterization of Heterogenous Metal Systems*. PhD thesis, Universität Konstanz, 2005.

[32] Christian Michaelis. *Local electronic properties of individual nanostructures on the boron nitride nanomesh*. PhD thesis, Universität Konstanz, 2010.

[33] Franz J. Giessibl. High-speed force sensor for force microscopy and profilometry utilizing a quartz tuning fork. *Applied Physics Letters*, 73(26):3956, 1998.

[34] S. H. Pan, E. W. Hudson, and J. C. Davis. [3]He refrigerator based very low temperature scanning tunneling microscope. *Review of Scientific Instruments*, 70(2):1459, 1999.

[35] Tobias Herden. *Aufbau eines Q-Sensor AFM/STMs für den Einsatz bei tiefen Temperaturen*. Diploma thesis, Universität Konstanz, 2010.

[36] Masafumi Tamura, Yasuhiro Nakazawa, Daisuke Shiomi, and Kiyokazu Nozawa. Bulk ferromagnetism in the beta-phase crystal of the p-nitrophenyl nitronyl nitroxide radical. *Chemical Physics Letters*, 186(4):401–404, 1991.

[37] A Caneschi, D Gatteschi, R Sessoli, A Barra, L Brunel, and M Guillot. Alternating Current Susceptibility, High Field Magnetization, and Millimeter Band EPR Evidence for a Ground S = 10 State in [Mn12O12(CH3COO)16(H2O)4] 2CH3COOH4H2O. *Journal of the American Chemical Society*, 113(15):5873–5874, 1991.

[38] R Sessoli, D Gatteschi, A Caneschi, and MA Novak. Magnetic bistability in a metal-ion cluster. *Nature*, 365:141, 1993.

[39] W. Wernsdorfer, M. Murugesu, and G. Christou. Resonant Tunneling in Truly Axial Symmetry Mn12 Single-Molecule Magnets: Sharp Crossover between Thermally Assisted and Pure Quantum Tunneling. *Physical Review Letters*, 96(5):3–6, February 2006.

[40] Sheila M J Aubin, Neil R Dilley, Luca Pardi, J Krzystek, Michael W Wemple, Louis-claude Brunel, M Brian Maple, George Christou, and David N Hendrickson. Resonant Magnetization Tunneling in the Trigonal Pyramidal MnIVMnIII_3 Complex [Mn_4O_3Cl(O_2CCH_3)_3(dbm)_3]. *Journal of the American Chemical Society*, 120(20):4991–5004, 1998.

[41] Constantinos J Milios, Alina Vinslava, Wolfgang Wernsdorfer, Stephen Moggach, Simon Parsons, Spyros P Perlepes, George Christou, and Euan K Brechin. A record anisotropy barrier for a single-molecule magnet. *Journal of the American Chemical Society*, 129(10):2754–5, March 2007.

[42] Anastasios J. Tasiopoulos, Alina Vinslava, Wolfgang Wernsdorfer, Khalil A. Abboud, and George Christou. Giant Single-Molecule Magnets: A {Mn84} Torus and Its Supramolecular Nanotubes. *Angewandte Chemie*, 116(16):2169–2173, April 2004.

[43] A.-L. Barra, P. Debrunner, D. Gatteschi, Ch. Schulz, and R. Sessoli. Superparamagnetic-like behavior in an octanuclear iron cluster. *EPL (Europhysics Letters)*, 35(2):133, 1996.

[44] Naoto Ishikawa, Miki Sugita, Tadahiko Ishikawa, Shin-Ya Koshihara, and Youkoh Kaizu. Lanthanide double-decker complexes functioning as magnets at the single-molecular level. *Journal of the American Chemical Society*, 125(29):8694–5, July 2003.

[45] Ching Tsang, Mao-Min Chen, and Tadashi Yogi. Gigabit-density magnetic recording. *Proceedings of the IEEE*, 81(9):1344, 1993.

[46] Robert E. Fontana, Steven R. Hetzler, and Gary Decad. Technology Roadmap Comparisons for TAPE, HDD, and NAND Flash: Implications for Data Storage Applications. *IEEE Transactions on Magnetics*, 48(5):1692–1696, May 2012.

[47] Prachi Patel. How Seagate's Terabit-Per-Square-Inch Hard Drive Works. *MIT Technology Review*, Mar 23, 2012.

[48] Akira Kikitsu and Yoshiyuki Kamata. Recent progress of patterned media. *IEEE Transactions on Magnetics*, 43(9):3685–3688, 2007.

[49] Stuart S P Parkin, Masamitsu Hayashi, and Luc Thomas. Magnetic domain-wall racetrack memory. *Science*, 320(5873):190–4, April 2008.

[50] J R Friedman, M P Sarachik, J Tejada, and R Ziolo. Macroscopic measurement of resonant magnetization tunneling in high-spin molecules. *Physical Review Letters*, 76(20):3830–3833, May 1996.

[51] Alain Chiolero and Daniel Loss. Macroscopic Quantum Coherence in Molecular Magnets. *Physical Review Letters*, 80(1):169–172, January 1998.

[52] Arzhang Ardavan, Olivier Rival, John Morton, Stephen Blundell, Alexei Tyryshkin, Grigore Timco, and Richard Winpenny. Will Spin-Relaxation Times in Molecular Magnets Permit Quantum Information Processing? *Physical Review Letters*, 98(5):057201, January 2007.

[53] W. Wernsdorfer and R. Sessoli. Quantum Phase Interference and Parity Effects in Magnetic Molecular Clusters. *Science*, 284:133–135, April 1999.

[54] S. Heinze. Real-Space Imaging of Two-Dimensional Antiferromagnetism on the Atomic Scale. *Science*, 288(5472):1805–1808, June 2000.

[55] Dante Gatteschi, Roberta Sessoli, and Jacques Villain. *Molecular Nanomagnets*. Oxford University Press, 2006.

[56] Cyrus F Hirjibehedin, Chiung-Yuan Lin, Alexander F Otte, Markus Ternes, Christopher P Lutz, Barbara A Jones, and Andreas J Heinrich. Large magnetic anisotropy of a single atomic spin embedded in a surface molecular network. *Science*, 317(5842):1199–203, August 2007.

[57] T. Balashov, T. Schuh, A. Takács, A. Ernst, S. Ostanin, J. Henk, I. Mertig, P. Bruno, T. Miyamachi, S. Suga, and W. Wulfhekel. Magnetic Anisotropy and Magnetization Dynamics of Individual Atoms and Clusters of Fe and Co on Pt(111). *Physical Review Letters*, 102(25), June 2009.

[58] A. A. Khajetoorians, S. Lounis, B. Chilian, A. T. Costa, L. Zhou, D. L. Mills, J. Wiebe, and R. Wiesendanger. Itinerant Nature of Atom-Magnetization Excitation by Tunneling Electrons. *Physical Review Letters*, 106(3):037205, January 2011.

[59] Cyrus F Hirjibehedin, Christopher P Lutz, and Andreas J Heinrich. Spin coupling in engineered atomic structures. *Science*, 312(5776):1021–4, May 2006.

[60] Sebastian Loth, Christopher P Lutz, and Andreas J Heinrich. Spin-polarized spin excitation spectroscopy. *New Journal of Physics*, 12(12):125021, December 2010.

[61] Xi Chen, Ying-Shuang Fu, Shuai-Hua Ji, Tong Zhang, Peng Cheng, Xu-Cun Ma, Xiao-Long Zou, Wen-Hui Duan, Jin-Feng Jia, and Qi-Kun Xue. Probing Superexchange Interaction in Molecular Magnets by Spin-Flip Spectroscopy and Microscopy. *Physical Review Letters*, 101(19), November 2008.

[62] Ying-Shuang Fu, Tong Zhang, Shuai-Hua Ji, Xi Chen, Xu-Cun Ma, Jin-Feng Jia, and Qi-Kun Xue. Identifying Charge States of Molecules with Spin-Flip Spectroscopy. *Physical Review Letters*, 103(25):257202, December 2009.

[63] Noriyuki Tsukahara, Ken-ichi Noto, Michiaki Ohara, Susumu Shiraki, Noriaki Takagi, Shik Shin, and Maki Kawai. Adsorption-Induced Switching of Magnetic Anisotropy in a Single Iron(II) Phthalocyanine Molecule on an Oxidized Cu(110) Surface. *Physical Review Letters*, 102(16):167203, April 2009.

[64] M. A. Novak and R Sessoli. Magnetic properties of a Mn cluster organic compound. *Journal of Magnetism and Magnetic Materials*, 146:211–213, 1995.

[65] Luc Thomas, Andrea Caneschi, and Bernard Barbara. Nonexponential Dynamic Scaling of the Magnetization Relaxation in Mn_{12} Acetate. *Physical Review Letters*, 83(12), 1999.

[66] Myles R Cheesman, Vasili S Oganesyan, Roberta Sessoli, Dante Gatteschi, and Andrew J Thomson. Magnetically induced optical bi-stability of the molecular

nanomagnet Mn12O12 (OOCMe)16 (H2O)4 in an organic glass. *Chemical Communications*, 12:1677–1678, 1997.

[67] EJL McInnes, Elna Pidcock, Vasili S Oganesyan, MR Cheesman, AK Powell, and Andrew J Thomson. Optical Detection of Spin Polarization in Single-Molecule Magnets. *Journal of the American Chemical Society*, 124:9219–9228, 2002.

[68] L Thomas, F Lionti, R Ballou, and D Gatteschi. Macroscopic quantum tunnelling of magnetization in a single crystal of nanomagnets. *Nature*, 383, 1996.

[69] T Lis. Preparation, structure, and magnetic properties of a dodecanuclear mixed-valence manganese carboxylate. *Acta Crystallographica B*, 36(9):2042–2046, 1980.

[70] RA Robinson and PJ Brown. Internal magnetic structure of Mn12 acetate by polarized neutron diffraction. *Journal of Physics: Condensed Matter*, 12:2805–2810, 2000.

[71] Laura Zobbi, Matteo Mannini, Mirko Pacchioni, Guillaume Chastanet, Daniele Bonacchi, Chiara Zanardi, Roberto Biagi, Umberto Del Pennino, Dante Gatteschi, Andrea Cornia, and Roberta Sessoli. Isolated single-molecule magnets on native gold. *Chemical Communications*, 6(12):1640, March 2005.

[72] S. Voss, M. Fonin, U. Rüdiger, M. Burgert, U. Groth, and Y. Dedkov. Electronic structure of Mn12 derivatives on the clean and functionalized Au surface. *Physical Review B*, 75(4):045102, January 2007.

[73] Matteo Mannini, Philippe Sainctavit, Roberta Sessoli, Christophe Cartier dit Moulin, Francesco Pineider, Marie-Anne Arrio, Andrea Cornia, and Dante Gatteschi. XAS and XMCD investigation of Mn12 monolayers on gold. *Chemistry-A European Journal*, 14(25):7530–5, January 2008.

[74] H. Heersche, Z. de Groot, J. Folk, H. van der Zant, C. Romeike, M. Wegewijs, L. Zobbi, D. Barreca, E. Tondello, and A. Cornia. Electron Transport through Single Mn12 Molecular Magnets. *Physical Review Letters*, 96(20), May 2006.

[75] Moon-Ho Jo, Jacob E Grose, Kanhayalal Baheti, Mandar M Deshmukh, Jennifer J Sokol, Evan M Rumberger, David N Hendrickson, Jeffrey R Long, Hongkun Park, and D C Ralph. Signatures of molecular magnetism in single-molecule transport spectroscopy. *Nano Letters*, 6(9):2014–20, September 2006.

[76] Guillaume Rogez, Bertrand Donnio, Emmanuel Terazzi, Jean-Louis Gallani, Jean-Paul Kappler, Jean-Pierre Bucher, and Marc Drillon. The Quest for Nanoscale Magnets: The example of [Mn12] Single Molecule Magnets. *Advanced Materials*, 21(43):4323–4333, November 2009.

[77] Joulia Larionova, Rodolphe Clérac, Bruno Boury, Jean Le Bideau, Lollita Lecren, and Stephanie Willemin. Structural and magnetic studies of the

[Mn12O12(CH3COO)16(H2O)4] 2CH3COOH 4H2O thermal derivatives. *Journal of Materials Chemistry*, 13(4):795–799, March 2003.

[78] A. Naitabdi, J.-P. Bucher, Ph. Gerbier, P. Rabu, and M. Drillon. Self-Assembly and Magnetism of Mn12 Nanomagnets on Native and Functionalized Gold Surfaces. *Advanced Materials*, 17(13):1612–1616, July 2005.

[79] Michael Burgert, Sönke Voss, Simon Herr, Mikhail Fonin, Ulrich Groth, and Ulrich Rüdiger. Single-molecule magnets: a new approach to investigate the electronic structure of Mn12 molecules by scanning tunneling spectroscopy. *Journal of the American Chemical Society*, 129(46):14362–6, November 2007.

[80] S. Voss, O. Zander, M. Fonin, U. Rüdiger, M. Burgert, and U. Groth. Electronic transport properties and orientation of individual Mn12 single-molecule magnets. *Physical Review B*, 78(15):155403, October 2008.

[81] Alex Saywell, Graziano Magnano, Christopher J Satterley, Luís M A Perdigão, Andrew J Britton, Nassiba Taleb, María del Carmen Giménez-López, Neil R Champness, James N O'Shea, and Peter H Beton. Self-assembled aggregates formed by single-molecule magnets on a gold surface. *Nature Communications*, 1:75, January 2010.

[82] Karsten Handrup, Victoria Richards, Matthew Weston, James O'Shea, and Neil Champness. Single Molecule Magnets with Protective Ligand Shells on Gold and Titanium Dioxide Surfaces: In-situ Electrospray Deposition and X-ray Absorption Spectroscopy (working title). *unpublished results, private communications with J.O'Shea*, 2013.

[83] Steffen Kahle, Zhitao Deng, Nikola Malinowski, Charlène Tonnoir, Alicia Forment-Aliaga, Nicha Thontasen, Gordon Rinke, Duy Le, Volodymyr Turkowski, Talat S Rahman, Stephan Rauschenbach, Markus Ternes, and Klaus Kern. The Quantum Magnetism of Individual Manganese-12-Acetate Molecular Magnets Anchored at Surfaces. *Nano Letters*, 12(1):518–21, January 2012.

[84] Zheng Ouyang, Zoltán Takáts, Thomas A Blake, Bogdan Gologan, Andy J Guymon, Justin M Wiseman, Justin C Oliver, V Jo Davisson, and R Graham Cooks. Preparing protein microarrays by soft-landing of mass-selected ions. *Science*, 301(5638):1351–4, September 2003.

[85] Stephan Rauschenbach, Frank L Stadler, Eugenio Lunedei, Nicola Malinowski, Sergej Koltsov, Giovanni Costantini, and Klaus Kern. Electrospray ion beam deposition of clusters and biomolecules. *Small*, 2(4):540–7, April 2006.

[86] Stephan Rauschenbach, Ralf Vogelgesang, Nicola Malinowski, Jürgen W Gerlach, Mohamed Benyoucef, Giovanni Costantini, Zhitao Deng, Nicha Thontasen, and Klaus Kern. Electrospray ion beam deposition: soft-landing and fragmentation of functional molecules at solid surfaces. *ACS Nano*, 3(10):2901–10, October 2009.

[87] Grant E Johnson, Qichi Hu, and Julia Laskin. Soft landing of complex molecules on surfaces. *Annual Review of Analytical Chemistry*, 4:83–104, January 2011.

[88] Anne Barra, Dante Gatteschi, and Roberta Sessoli. High-frequency EPR spectra of a molecular nanomagnet: Understanding quantum tunneling of the magnetization. *Physical Review B*, 56(13):8192–8198, October 1997.

[89] G Kresse and J Furthmüller. Efficient iterative schemes for ab initio total-energy calculations using a plane-wave basis set. *Physical Review B*, 54(16):11169–11186, October 1996.

[90] J Perdew, K Burke, and M Ernzerhof. Generalized Gradient Approximation Made Simple. *Physical Review Letters*, 77(18):3865–3868, October 1996.

[91] PE Blöchl. Projector augmented-wave method. *Physical Review B*, 50(24), 1994.

[92] G Kresse and D Joubert. From ultrasoft pseudopotentials to the projector augmented-wave method. *Physical Review B*, 59(3):11–19, 1999.

[93] SL Dudarev, GA Botton, SY Savrasov, CJ Humphreys, and AP Sutton. Electron-energy-loss spectra and the structural stability of nickel oxide: An LSDA+U study. *Physical Review Letters*, 57(3):1505–1509, 1998.

[94] R Sessoli, H-L Tsai, AR Schake, S Wang, J Vincent, K Folting, D Gatteschi, G Christou, and DN Hendrickson. High Spin Molecules [Mn12O12(O2CR)16(H2O)4]. *Journal of the American Chemical Society*, 115:1804–1816, 1993.

[95] M Hennion, L Pardi, I Mirebeau, and E Suard. Neutron study of mesoscopic magnetic clusters: Mn_{12} O_{12}. *Physical Review B*, 56(14):8819–8827, 1997.

[96] M. Katsnelson, V. Dobrovitski, and B. Harmon. Many-spin interactions and spin excitations in Mn12. *Physical Review B*, 59(10):6919–6926, March 1999.

[97] J. Fernández-Rossier. Theory of Single-Spin Inelastic Tunneling Spectroscopy. *Physical Review Letters*, 102:256802, 2009.

[98] Nicolás Lorente and Jean-Pierre Gauyacq. Efficient Spin Transitions in Inelastic Electron Tunneling Spectroscopy. *Physical Review Letters*, 103(17):176601, October 2009.

[99] I Mirebeau, M Hennion, H Casalta, H Andres, H Güdel, A Irodova, and A Caneschi. Low-Energy Magnetic Excitations of the Mn_ {12}-Acetate Spin Cluster Observed by Neutron Scattering. *Physical Review Letters*, 83(3), 1999.

[100] Gert-Ludwig Ingold. Charge Tunneling Rates in Ultrasmall Junctions. *NATO ASI Series B*, 294:21–107, 1992.

[101] Charlène Tonnoir. *Low Temperature Scanning Tunneling Microscopy and Spectroscopy on Single Molecular Magnets*. Master thesis, Université Joseph-Fourier Grenoble, 2010.

[102] A. Sushkov, J. Musfeldt, Y. Wang, R. Achey, and N. Dalal. Spin-vibrational coupling in the far-infrared spectrum of Mn12-acetate. *Physical Review B*, 66(14):144430, October 2002.

[103] J. M. North, L. J. van de Burgt, and N. S. Dalal. A Raman study of the single molecule magnet Mn 12-acetate and analogs. *Solid State Communications*, 123(1):75–79, 2002.

[104] Kingsley L. Taft, Georgia C. Delfs, Christopher D. Papaefthymiou, Simon Foner, Dante Gatteschi, and Stephen J. Lippard. [Fe(OMe)_2(O_2CCH_2Cl)]_10, a Molecular Ferric Wheel. *Journal of the American Chemical Society*, 116(3), 1994.

[105] Stephen P Watton, Peter Fuhrmann, Laura E Pence, Andrea Caneschi, Andrea Cornia, Gian Luca Abbati, and Stephen J Lippard. A Cyclic Octadecairon (III) Complex, the Molecular 18 Wheeler. *Angewandte Chemie International Edition*, 36(24):2774–2776, 1997.

[106] Andrea Caneschi, Andrea Cornia, Antonio C. Fabretti, and Dante Gatteschi. Structure and Magnetic Properties of a Dodecanuclear Twisted-Ring Iron(III) Cluster. *Angewandte Chemie International Edition*, 38(9):1295–1297, 1999.

[107] Finn K. Larsen, Eric J. L. McInnes, Hassane El Mkami, Jacob Overgaard, Stergios Piligkos, Gopalan Rajaraman, Eva Rentschler, Andrew A. Smith, Graham M. Smith, Val Boote, Martin Jennings, Grigore A. Timco, and Richard E. P. Winpenny. Synthesis and characterization of heterometallic {Cr7M} wheels. *Angewandte Chemie International Edition*, 42(1):101–105, 2003.

[108] Joris van Slageren, Roberta Sessoli, Dante Gatteschi, Andrew A Smith, Madeleine Helliwell, Richard E P Winpenny, Andrea Cornia, Anne-Laure Barra, Aloysius G M Jansen, Eva Rentschler, and Grigore A Timco. Magnetic anisotropy of the antiferromagnetic ring [Cr8F8Piv16]. *Chemistry-A European Journal*, 8(1):277–85, January 2002.

[109] F. Troiani, A. Ghirri, M. Affronte, S. Carretta, P. Santini, G. Amoretti, S. Piligkos, G. Timco, and R. Winpenny. Molecular Engineering of Antiferromagnetic Rings for Quantum Computation. *Physical Review Letters*, 94(20):207208, May 2005.

[110] Grigore A. Timco, Stefano Carretta, Filippo Troiani, Floriana Tuna, Robin J. Pritchard, Christopher A. Muryn, Eric J. L. McInnes, Alberto Ghirri, Andrea Candini, Paolo Santini, Giuseppe Amoretti, Marco Affronte, and Richard E. P. Winpenny. Engineering the coupling between molecular spin qubits by coordination chemistry. *Nature Nanotechnology*, 4:173–178, 2009.

[111] A. Candini, G. Lorusso, F. Troiani, A. Ghirri, S. Carretta, P. Santini, G. Amoretti, C. Muryn, F. Tuna, G. Timco, E. J. L. McInnes, R. E. P. Winpenny, W. Wernsdorfer, and M. Affronte. Entanglement in Supramolecular Spin Systems of Two Weakly Coupled Antiferromagnetic Rings (Purple-Cr_{7}Ni). *Physical Review Letters*, 104(3):037203, January 2010.

[112] S. Carretta, P. Santini, G. Amoretti, T. Guidi, J. Copley, Y. Qiu, R. Caciuffo, G. Timco, and R. Winpenny. Quantum Oscillations of the Total Spin in a Heterometallic Antiferromagnetic Ring: Evidence from Neutron Spectroscopy. *Physical Review Letters*, 98(16):167401, April 2007.

[113] V. Corradini, F. Moro, R. Biagi, V. de Renzi, U. del Pennino, V. Bellini, S. Carretta, P. Santini, V. Milway, G. Timco, R. Winpenny, and M. Affronte. Successful grafting of isolated molecular Cr7Ni rings on Au(111) surface. *Physical Review B*, 79(14), April 2009.

[114] V. Corradini, A. Ghirri, U. del Pennino, R. Biagi, V. Milway, G. Timco, F. Tuna, R.E.P. Winpenny, and M. Affronte. Grafting molecular Cr7Ni rings on a gold surface. *Dalton Transactions*, 39:4928, May 2010.

[115] Alberto Ghirri, Valdis Corradini, Valerio Bellini, Roberto Biagi, Umberto del Pennino, Valentina de Renzi, Julio C. Cezar, Christopher A. Muryn, Grigore A. Timco, Richard E.P. Winpenny, and Marco Affronte. Self-Assembled Monolayer of Cr(7)Ni Molecular Nanomagnets by Sublimation. *ACS Nano*, 9:7090–7099, August 2011.

[116] MP Sarachik, E Corenzwit, and LD Longinotti. Resistivity of Mo-Nb and Mo-Re Alloys Containing 1% Fe. *Physical Review*, 135(4), 1964.

[117] PW Anderson. A poor man's derivation of scaling laws for the Kondo problem. *Journal of Physics C: Solid State Physics*, 3, 1970.

[118] Kenneth G Wilson. The renormalization group: Critical Phenomena and the Kondo Problem. *Reviews of Modern Physics*, 47(4), 1975.

[119] PW Anderson. Localized magnetic states in metals. *Physical Review*, 124(1):41, 1961.

[120] JR Schrieffer and PA Wolff. Relation between the Anderson and Kondo Hamiltonians. *Physical Review*, 14(2), 1966.

[121] S Sasaki, S de Franceschi, JM Elzerman, WG van der Wiel, M Eto, S Tarucha, and LP Kouwenhoven. Kondo effect in an integer-spin quantum dot. *Nature*, 405(6788):764–7, June 2000.

[122] M Pustilnik, Y Avishai, and K Kikoin. Quantum Dots with Even Number of Electrons: Kondo Effect in a Finite Magnetic Field. *Physical Review Letters*, 84(8):1756–9, February 2000.

[123] J Nygard, D H Cobden, and P E Lindelof. Kondo physics in carbon nanotubes. *Nature*, 408(6810):342–6, November 2000.

[124] Jiutao Li, Wolf-Dieter Schneider, Richard Berndt, and Bernard Delley. Kondo Scattering Observed at a Single Magnetic Impurity. *Physical Review Letters*, 80(13):2893–2896, March 1998.

[125] HC Manoharan, CP Lutz, and DM Eigler. Quantum mirages formed by coherent projection of electronic structure. *Nature*, 403(6769):512–5, February 2000.

[126] P. Wahl, L. Diekhöner, M. Schneider, L. Vitali, G. Wittich, and K. Kern. Kondo Temperature of Magnetic Impurities at Surfaces. *Physical Review Letters*, 93(17):176603, October 2004.

[127] Alexander F. Otte, Markus Ternes, Kirsten von Bergmann, Sebastian Loth, Harald Brune, Christopher P. Lutz, Cyrus F. Hirjibehedin, and Andreas J. Heinrich. The role of magnetic anisotropy in the Kondo effect. *Nature Physics*, 4(11):847–850, September 2008.

[128] Rok Žitko. Kondo resonance lineshape of magnetic adatoms on decoupling layers. *Physical Review B*, 84(19):195116, November 2011.

[129] K Nagaoka, T Jamneala, M Grobis, and M F Crommie. Temperature Dependence of a Single Kondo Impurity. *Physical Review Letters*, 88(7), 2002.

[130] A. Otte, M. Ternes, S. Loth, C. Lutz, C. Hirjibehedin, and A. Heinrich. Spin Excitations of a Kondo-Screened Atom Coupled to a Second Magnetic Atom. *Physical Review Letters*, 103(10), September 2009.

[131] Jakob Bork, Yong-hui Zhang, Lars Diekhöner, László Borda, Pascal Simon, Johann Kroha, Peter Wahl, and Klaus Kern. A tunable two-impurity Kondo system in an atomic point contact. *Nature Physics*, 7(11):901–906, August 2011.

[132] Aidi Zhao, Qunxiang Li, Lan Chen, Hongjun Xiang, Weihua Wang, Shuan Pan, Bing Wang, Xudong Xiao, Jinlong Yang, J.G. Hou, and Qingshi Zhu. Controlling the Kondo effect of an adsorbed magnetic ion through its chemical bonding. *Science*, 309(5740):1542–4, September 2005.

[133] K J Franke, G Schulze, and J I Pascual. Competition of superconducting phenomena and Kondo screening at the nanoscale. *Science*, 332(6032):940–4, May 2011.

[134] Noriyuki Tsukahara, Susumu Shiraki, Saika Itou, Naoka Ohta, Noriaki Takagi, and Maki Kawai. Evolution of Kondo Resonance from a Single Impurity Molecule to the Two-Dimensional Lattice. *Physical Review Letters*, 106(18):187201, May 2011.

[135] Violeta Iancu, Aparna Deshpande, and Saw-Wai Hla. Manipulating Kondo temperature via single molecule switching. *Nano Letters*, 6(4):820–3, April 2006.

[136] U. G. E. Perera, H. J. Kulik, V. Iancu, L. G. G. V. Dias da Silva, S. E. Ulloa, N. Marzari, and S.-W. Hla. Spatially Extended Kondo State in Magnetic Molecules Induced by Interfacial Charge Transfer. *Physical Review Letters*, 105(10):106601, September 2010.

[137] Aidi Zhao, Zhenpeng Hu, Bing Wang, Xudong Xiao, Jinlong Yang, and J.G. Hou. Kondo effect in single cobalt phthalocyanine molecules adsorbed on Au(111) monoatomic steps. *The Journal of Chemical Physics*, 128(23):234705, June 2008.

[138] P. Wahl, L. Diekhöner, G. Wittich, L. Vitali, M.A. Schneider, and K. Kern. Kondo Effect of Molecular Complexes at Surfaces: Ligand Control of the Local Spin Coupling. *Physical Review Letters*, 95(16):166601, October 2005.

[139] Daniel Wegner, Ryan Yamachika, Xiaowei Zhang, Yayu Wang, Tunna Baruah, Mark Pederson, Bart Bartlett, Jeffrey Long, and Michael Crommie. Tuning Molecule-Mediated Spin Coupling in Bottom-Up-Fabricated Vanadium-Tetracyanoethylene Nanostructures. *Physical Review Letters*, 103(8):087205, August 2009.

[140] I. Fernández-Torrente, K. Franke, and J. Pascual. Vibrational Kondo Effect in Pure Organic Charge-Transfer Assemblies. *Physical Review Letters*, 101(21):217203, November 2008.

[141] R Temirov, A Lassise, F B Anders, and F S Tautz. Kondo effect by controlled cleavage of a single-molecule contact. *Nanotechnology*, 19(6):065401, February 2008.

[142] Taeyoung Choi, Stéphane Bedwani, Alain Rochefort, Chia-Yi Chen, Arthur J Epstein, and Jay A Gupta. A single molecule Kondo switch: multistability of tetracyanoethylene on Cu(111). *Nano Letters*, 10(10):4175–80, October 2010.

[143] AFG Wyatt. Anomalous Densities of States in Normal Metal Tantalum and Niobium. *Physical Review Letters*, 13(13):401–404, 1964.

[144] RA Logan and JM Rowell. Conductance anomalies in semiconductor tunnel diodes. *Physical Review Letters*, 13(13), 1964.

[145] Joel Appelbaum. "sd" exchange model of Zero-Bias tunneling anomalies. *Physical Review Letters*, 17(2), 1966.

[146] PW Anderson. Localized magnetic states and Fermi-surface anomalies in tunneling. *Physical Review Letters*, 17(2), 1966.

[147] Joel Appelbaum. Exchange Model of Zero-Bias Tunneling Anomalies. *Physical Review*, 154(3):633–643, 1967.

[148] P Nozieres. A "Fermi-liquid" description of the Kondo problem at low temperatures. *Journal of Low Temperature Physics*, 17:31–42, 1974.

[149] Henning Prüser, Martin Wenderoth, Piet E. Dargel, Alexander Weismann, Robert Peters, Thomas Pruschke, and Rainer G. Ulbrich. Long-range Kondo signature of a single magnetic impurity. *Nature Physics*, 7(3):203–206, January 2011.

[150] H. Prüser, M. Wenderoth, A. Weismann, and R. G. Ulbrich. Mapping Itinerant Electrons around Kondo Impurities. *Physical Review Letters*, 108(16):166604, April 2012.

[151] D.-J. Choi, M. V. Rastei, P. Simon, and L. Limot. Conductance-Driven Change of the Kondo Effect in a Single Cobalt Atom. *Physical Review Letters*, 108(26):266803, June 2012.

[152] HO Frota and LN Oliveira. Photoemission spectroscopy for the spin-degenerate Anderson model. *Physical Review B*, 33(11):7871–7874, 1986.

[153] HO Frota. Shape of the Kondo resonance. *Physical Review B*, 45(3), 1992.

[154] Henning Prüser, Martin Wenderoth, Piet E Dargel, Alexander Weismann, Robert Peters, Thomas Pruschke, and Rainer G Ulbrich. Supplementary Information : Long range Kondo signature of a single magnetic impurity. *Nature Physics*, 7(3), 2011.

[155] F Patthey, WD Schneider, Y Baer, and B Delley. High-temperature collapse of the Kondo resonance in CeSi2 observed by photoemission. *Physical Review Letters*, 58(26):2810, 1987.

[156] U Fano. Effects of configuration interaction on intensities and phase shifts. *Physical Review*, 124(6):1866–1878, 1961.

[157] O Újsághy, J Kroha, L Szunyogh, and A Zawadowski. Theory of the Fano Resonance in STM Tunneling Density of States due to a Single Kondo Impurity. *Physical Review Letters*, 85(12):2557–2560, 2000.

[158] Yong-hui Zhang, Steffen Kahle, Tobias Herden, Christophe Stroh, Marcel Mayor, Uta Schlickum, Markus Ternes, Peter Wahl, and Klaus Kern. Temperature and Magnetic Field Dependence of a Kondo System in the Weak Coupling Regime. *Nature Communications*, 4:2110, 2013.

[159] E Ressouche and JX Boucherle. Spin density maps in nitroxide-copper (II) complexes. A polarized neutron diffraction determination. *Journal of the American Chemical Society*, 115:3610–3617, 1993.

[160] Andrei Zheludev, Vincenzo Barone, and Michel Bonnet. Spin density in a nitronyl nitroxide free radical. Polarized neutron diffraction investigation and ab initio calculations. *Journal of the American Chemical Society*, 116:2019–2027, 1994.

[161] Andrea Caneschi, Dante Gatteschi, Roberta Sessoli, and Paul Rey. Toward molecular magnets: the metal-radical approach. *Accounts of Chemical Research*, 22:392–398, 1989.

[162] Andrea Caneschi and Dante Gatteschi. Cobalt (II)-Nitronyl Nitroxide Chains as Molecular Magnetic Nanowires. *Angewandte Chemie International Edition*, 40(9):1760, 2001.

[163] Yong-hui Zhang. *Experimental Study of Quantum Transport through Single Atomic Junctions and the Magnetic Properties of Organic Radicals on Gold Surface*. PhD thesis, Tsinghua University, Beijing, 2011.

[164] Markus Ternes, Andreas J Heinrich, and Wolf-Dieter Schneider. Spectroscopic manifestations of the Kondo effect on single adatoms. *Journal of Physics: Condensed Matter*, 21(5):053001, February 2009.

[165] D. Goldhaber-Gordon, J. Göres, M. Kastner, H. Shtrikman, D. Mahalu, and U. Meirav. From the Kondo Regime to the Mixed-Valence Regime in a Single-Electron Transistor. *Physical Review Letters*, 81(23):5225–5228, December 1998.

[166] Alex C Hewson. *The Kondo Problem to Heavy Fermions*. Cambridge University Press, 1993.

[167] J J Parks, A R Champagne, T A Costi, W W Shum, A N Pasupathy, E Neuscamman, S Flores-Torres, P S Cornaglia, A A Aligia, C A Balseiro, G K-L Chan, H D Abruña, and D C Ralph. Mechanical control of spin states in spin-1 molecules and the underscreened Kondo effect. *Science*, 328(5984):1370–3, June 2010.

[168] T. A. Costi. Kondo Effect in a Magnetic Field and the Magnetoresistivity of Kondo Alloys. *Physical Review Letters*, 85(7):1504–7, August 2000.

[169] EL Wolf and DL Losee. g-shifts in the "sd" exchange theory of zero-bias tunneling anomalies. *Physics Letters A*, 29(6):5–6, 1969.

[170] M. N. Kiselev, K. A. Kikoin, L. Y. Gorelik, and R. I. Shekhter. Kondo Force in Shuttling Devices: Dynamical Probe for a Kondo Cloud. *Physical Review Letters*, 110(6):066804, February 2013.

[171] A Nagashima, N Tejima, Y Gamou, T Kawai, and C Oshima. Electronic structure of monolayer hexagonal boron nitride physisorbed on metal surfaces. *Physical Review Letters*, 75(21):3918–3921, 1995.

[172] MT Paffett, RJ Simonson, P Papin, and RT Paine. Borazine adsorption and decomposition at Pt (111) and Ru (001) surfaces. *Surface Science*, 232:286–296, 1990.

[173] Martina Corso, Willi Auwärter, Matthias Muntwiler, Anna Tamai, Thomas Greber, and Jürg Osterwalder. Boron nitride nanomesh. *Science*, 303(5655):217–20, January 2004.

[174] O. Bunk, M. Corso, D. Martoccia, R. Herger, P.R. Willmott, B.D. Patterson, J. Osterwalder, J.F. van der Veen, and T. Greber. Surface X-ray diffraction study of boron-nitride nanomesh in air. *Surface Science*, 601:L7–L10, January 2007.

[175] Simon Berner, Martina Corso, Roland Widmer, Oliver Groening, Robert Laskowski, Peter Blaha, Karlheinz Schwarz, Andrii Goriachko, Herbert Over, Stefan Gsell, Matthias Schreck, Hermann Sachdev, Thomas Greber, and Jürg Osterwalder. Boron nitride nanomesh: functionality from a corrugated monolayer. *Angewandte Chemie International Edition*, 46(27):5115–9, January 2007.

[176] W. Auwärter, T.J. Kreutz, T. Greber, and J. Osterwalder. XPD and STM investigation of hexagonal boron nitride on Ni(111). *Surface Science*, 429:229–236, June 1999.

[177] Andrii Goriachko, Yunbin He, Marcus Knapp, Herbert Over, Martina Corso, Thomas Brugger, Simon Berner, Juerg Osterwalder, and Thomas Greber. Self-assembly of a hexagonal boron nitride nanomesh on Ru(0001). *Langmuir : the ACS journal of surfaces and colloids*, 23(6):2928–31, March 2007.

[178] A.B. Preobrajenski, M.A. Nesterov, May Ling Ng, A.S. Vinogradov, and N. Martensson. Monolayer h-BN on lattice-mismatched metal surfaces: On the formation of the nanomesh. *Chemical Physics Letters*, 446(1-3):119–123, September 2007.

[179] Johannes V Barth, Giovanni Costantini, and Klaus Kern. Engineering atomic and molecular nanostructures at surfaces. *Nature*, 437(7059):671–9, September 2005.

[180] Ivan Brihuega, Christian Michaelis, Jian Zhang, Sangita Bose, Violetta Sessi, Jan Honolka, M Alexander Schneider, Axel Enders, and Klaus Kern. Electronic decoupling and templating of Co nanocluster arrays on the boron nitride nanomesh. *Surface Science*, 602(14):L95, 2008.

[181] Sangita Bose, Antonio M García-García, Miguel M Ugeda, Juan D Urbina, Christian H Michaelis, Ivan Brihuega, and Klaus Kern. Observation of shell effects in superconducting nanoparticles of Sn. *Nature Materials*, 9(7):550–4, July 2010.

[182] Ivan Brihuega, Antonio M. García-García, Pedro Ribeiro, Miguel M. Ugeda, Christian H. Michaelis, Sangita Bose, and Klaus Kern. Experimental observation of thermal fluctuations in single superconducting Pb nanoparticles through tunneling measurements. *Physical Review B*, 84(10):104525, September 2011.